AIAA Aviation
13-17 June 2016, Washington, D.C.
34th AIAA Applied Aerodynamics Conference

Numerical investigations of the vortical flow on swept wings with round leading edges

Andreas Schütte*
DLR - German Aerospace Center, Braunschweig, D-38108, Germany

The present work is investigating the vortex dominated flow physics as well as the aerodynamic behavior of swept wing configurations with round leading edges. The research is based on numerical simulations using the CFD method DLR TAU. The target configurations are swept wings of constant aspect ratio, variable leading edge contours and leading edge sweep angles. The work is dealing with the onset of the vortical flow at the leading edge for constant and variable leading edge nose radii, the influence of the angle of attack, the leading edge sweep and the onflow Mach number. Furthermore, the aerodynamic behavior is analyzed and assessed as well as the specific flow physics in the vicinity of the vortical flow separation at round leading edges. The objective of the present work is to provide a contribution for the design and assessment of the physical characteristics of swept wing configurations. Furthermore, sensitivities will be given for the design process. In addition, the current investigations provide a deeper understanding of the separation onset process and the flow physics of swept wing configurations with round leading edges.

Nomenclature

A	[m^2]	wing area
b	[m]	wing span
c_{ref}	[m]	wing reference length, depth of the wing
r	[m]	radius at nose of the profile
r_N	[-]	non-dimensional leading edge contour radius, $= r/c_{ref}$
s	[m]	wing semi span
x, y, z	[m]	cartesian coordinates
y_W	[m]	initial wall distance, distance of the first grid point from the wing surface
AR	[-]	wing aspect ratio, $= b^2/A$
α	[°]	angle of Attack or AoA
β	[°]	angle of side slip
φ	[°]	wing sweep
MRP		Moment Reference Point; $= 0.5 \cdot (s \cdot tan\varphi + c_{ref})$
c_L	[-]	lift coefficient, $= L/(\rho/2 \cdot U_\infty^2 \cdot A)$
c_D	[-]	drag coefficient, $= D/(\rho/2 \cdot U_\infty^2 \cdot A)$
c_M	[-]	pitching moment coefficient around MRP, pitch up positive, $= M/(\rho/2 \cdot U_\infty^2 \cdot A \cdot c_{ref})$
c_P	[-]	pressure coefficient , $= (p - p_\infty)/(\rho/2 \cdot U_\infty^2)$
a	[m/s]	speed of sound
M_∞	[-]	onflow Mach number, $= a/U_\infty$
Re_∞	[-]	Reynolds number, $= (U_\infty \cdot c_{ref})/\nu$
U_∞	[m/s]	onflow velocity
p	[N/m^2]	pressure
q_∞	[N/m^2]	onflow dynamic pressure
T	[K]	temperature
γ	[-]	circulation
μ	[Ns/m^2]	dynamic viscosity
ν	[m^2/s]	kinematic viscosity
ρ	[kg/m^3]	density
τ_W	[N/m^2]	wall friction

*Research Scientist, Institute of Aerodynamics and Flow Technology, Lilienthalplatz 7, 38108 Braunschweig, Germany, and AIAA Senior Member.

CFL	[-]	Courant–Friedrich–Lewy number, $= (u \cdot \Delta t)/\Delta x)$
Δt	[s]	discrete time step
Δx	[m]	discrete step in space
t	[s]	time
u	[m/s]	local velocity within the flow field
y^+	[-]	non-dimensional value to assess the resolution of the boundary layer wall unit, $= (\sqrt{\tau_W/\rho} \cdot y_W/\nu)$
$\|\frac{\partial \rho}{\partial t}\|$	[kg/m^{3}s]	density residual
p		pressure subscript
ref		reference parameter subscript
∞		onflow condition subscript
r		root subscript
le		leading edge subscript
AVT		Applied Vehicle Technology
$C^2A^2S^2E$		Center for Computer Applications in AeroSpace Science and Engineering
CST		Class Shape Function
$NATO$		Nothern Atlantic Treaty Organization
RTO		Research and Technology Organization
SA		Spalart-Allmaras turbulence model
STO		Science and Technology Organization (until 2012 RTO)
$SACCON$		Stability And Control CONfiguration
VFE		Vortex Flow Experiment

I. Introduction

Current and future uninhabited or partly autonomous fighter aircraft configurations will have wings with a low aspect ratio and a medium to high leading edge sweep angle. The leading edge sweep is a result of the aerodynamic requirements like high agility and/or performance at transonic or supersonic speed and results also from the demand of a low radar signature cross section.

At low speed the flight performance of a swept wing is significantly driven by the leading edge sweep angle. The flow physics of highly swept wings is dominated by a vortical flow field which occurs already at low angles of attack due to the separation of the flow at the leading edge. **Figure 1** shows an example of the complex vortical flow field of a generic blended wing body configuration with a sweep angle of 53°.

The contour radius is often variable along the leading edge and influences the separation sensitivity significantly. The sensitivity for separation increases for low angles of attack by decreasing the contour radius at the leading edge. Furthermore, the flow separation is also strongly influenced by the leading edge sweep, the onflow Mach number and the Reynolds number. This leads to the fact that in comparison to a swept wing with sharp leading edge, where the separation line is fixed at the leading edge, the position of the separation onset varies with the aforementioned flow parameters.

Position, strength and interferences of the vortex system at medium sweep angles from 45° to 60° only have a minor influence on the overall lift. At these sweep angles the nonlinear lift contribution is low in comparison to highly swept delta wings. On the other hand the influence on the moment balance can have a major impact. The movement of the vortex separation onset point with angle of attack can cause significant changes in the load distribution around the MRP.

The prediction of the vortical flow field around swept wings with round leading edges can only be achieved by the use of advanced computational methods like RANS solvers. For the modeling of the separation at curved contours the skin friction has to be taken also into account.

Figure 2 shows the CFD solution of a flow calculation around a delta wing with 65° leading edge sweep. Depicted are the streamlines starting at the leading edge close to the wall. The solution should give an example to show the differences in the flow topology between a sharp and a round leading edge. In the case of the sharp leading edge there is a primary separation with a fixed separation line directly at the leading edge. In the case of the round leading edge the flow is attached around the apex and separates further downstream. Additionally, for this specific case a second inner vortex is formed, rotates in the same direction as the outer one.

A. Background

In literature, several publications are dealing with the aerodynamics and flow physics of delta wings with round leading edges. The results can be taken as pre-studies for the current investigations. They deliver the justification for the validation of the numerical method DLR TAU and provide a ”Best Practice” for the grid generation.

Within the NATO RTO/AVT-113 Task Group on "Understanding and Modeling Vortical Flows to Improve the Technology Readiness Level for Military Aircraft" the "Second International Vortex Flow Experiment" (VFE-2) has been established. The objectives and the content are documented in detail in Hummel and Redeker[1] as well as in Hummel.[2,3] The VFE-2 65° delta wing wind tunnel model has interchangeable leading edges, which can be equipped with a sharp as well as with various round leading edges. The focus of the Task Group was the experimental and numerical identification of the flow phenomena for configuration with a medium round leading edge. The wind tunnel model provided by NASA was tested in various wind tunnel facilities at NASA, DLR, Onera, University of Glasgow and the Technical University of Munich. The test results from NASA are documented in Chu and Luckring.[4] In 2008 all experimental and numerical results have been published in several AIAA conference papers. The experimental investigations can be found in LeRoy et al.,[5] Furman and Breitsamter[6] and in Coton et al.[7] Furthermore, PIV measurements to analyze the flow physics of the vortical flow field are given by Konrath et al.[8] A summary of all experimental work is given by Luckring.[9]

The numerical investigations are documented by Fritz,[10] Schiavetta et al.,[11] Cummings and Schütte,[12] Crippa and Rizzi[13] and Gürdamar et al.[14] A summary of all numerical results is given by Fritz and Cummings.[15] A summary of the numerical results using the CFD method TAU are given from the author in the publication of Schütte and Lüdeke.[16] The results of the VFE-2 provide a first understanding of the complex vortical flow around a delta wing with round leading edges. This was achieved by an integrated process of experimental and numerical simulation. Within VFE-2 the detailed mechanism of the separation onset could not be solved entirely. Thus, a follow-on Task Group AVT-183 was established which will be introduced later on.

Within an internal DLR project and in cooperation with the NATO RTO/AVT-161 Task Group, two additional delta wing configurations with round leading edges have been explored. The first one, a model of the X-31 has been tested in the wind tunnel and, in parallel, various computational simulations have been conducted by the other project partners. The experimental results are documented by Rein et al.[17] The numerical results using TAU are described in detail by the author in Schütte et al.[18–22] Additional results are given by Boelens[23] and Jirasek.[24] It was shown that the complex vortical flow topology and aerodynamics could be predicted well by the CFD solver TAU and the computational methods use by the other project partners.

The second configuration was the so called SACCON. The SACCON configuration ("Stability And Control CONfiguration") is a blended wing body with a leading edge sweep of 53°. The related wind tunnel model was tested in various wind tunnel facilities and several numerical investigations at subsonic and transonic conditions have been conducted. The experimental results are described in detail by Loeser et al.[25] as well as by Vicroy and Löser.[26] Additional results of flow field measurements can be found in Konrath et al.[27] and Gilliot.[28]

The numerical results and analysis of the flow physics of the SACCON are documented in several publications by Frink,[29] Vallespin et al.,[30] Tormalm and Schmidt,[31] Le Roy and Morgand[32] as well as Cummings et al.[33] The investigations applying the CFD solver TAU are published by the author in Schütte et al.[34] Results for compressible and transonic onflow conditions are given in publications from Huber et al.,[35] Zimper and Rein[36] as well as Zimper and Hummel[37]. The achievements of the AVT-161 Task Group are the detailed analysis and understanding of the complex flow physics around the SACCON and the effects on the overall aerodynamics as well as the stability and control behavior. The results have shown that the leading edge contour is the main driver for the flow physics and the aerodynamic characteristics of the configuration.

Finally, within the AVT-201 the SACCON with control surfaces has been explored. The results of the very comprehensive wind tunnel investigations over a wide range of onflow conditions are documented by Huber et al.,[38] Vicroy et al.[39] and Rein et al.[40] the numerical work is ea. published by Frink,[41] Hitzel and Zimper,[42] Kennett et al.,[43] Lofthouse et al.[44] and Jirasek et al.[45] The TAU results are summarized by the author in Schütte et al.[46]

Within the German technology program SAGITTA *(Latin for Arrow)* experimental an numerical investigations have been conducted on a 53° diamond wing configuration with a variable leading edge contour. By Hövelmann and Breitsamter[47] leading-edge geometry effects have been evaluated on the diamond wing by examining the effect of various combinations of round and sharp contour areas along the leading edge. It has been shown that the vortical flow will be influenced significantly and though the longitudinal and lateral stability and control characteristic of the configuration.

For all discussed configurations the vortical flow topology has been predicted qualitatively quite well. Various aerodynamic quantities however are captured only in vicinity of the design point. In addition the mechanism of the vortical flow at the round leading edge has not been understood completely. Nevertheless, due to the various validated applications there exists a major confidence in the numerical methods to conduct the present numerical investigations.

As noted before, the separation onset and progression of the vortex at round leading edges was not entirely solved within VFE-2 and AVT-161. This was the motivation to establish a fundamental flow physics research group. The AVT-183 Task Group on "Reliable Prediction of Separated Flow Onset and Progression for Air and Sea Vehicles" was founded to gain a deeper understanding of the separation onset and progression of the flow at round leading edges. Finally, the flow physics regarding the separation mechanism could be described. The experimental and numerical results of AVT-183 are published by Boelens et al.,[48,49] Hövelmann et al.,[50,51] Hitzel et al.[52] and Frink.[53] Particularly, the description of the separation mechanism process described by Frink[53] should be taken into account as a reference

for the present investigations.

B. Motivation and Objectives

Multiple investigations have been conducted over the last several years regarding the vortical flow around swept wings with round leading edges. However, some questions remain which are not entirely answered. In the present work, the reason for the vortical flow progression will be investigated regarding certain onflow conditions. The aim is to show how the flow physics develops by changing the leading edge contour and onflow conditions. It should be documented at which onflow conditions for a particular leading edge geometry the vortex occurs and how it progresses depending on the angle of attack α, leading edge sweep φ and onflow Mach number. Regarding the separation onset the nomenclature and criteria defined by Frink[53] will be applied.

With these results sensitivities can be derived describing the onset and progression mechanism of the vortex depending on the given parameters. The influence of the leading edge contour on the development of the vortex can be examined separately. This means, the flow physics of variable leading contour of the SACCON can be dissolved.

Furthermore, it should be demonstrated in which way the aerodynamic behavior is influenced by the vortical flow field. Finally, the sensitivity studies as well as the results regarding the effect of the flow topology on the aerodynamic behavior can be used for the design process and assessment for configurations with swept wings and round leading edges.

C. Approach

The present paper is divided into three parts. The first part describes the pre-studies justifying the applicability of the CFD-Solver TAU for the current numerical investigation, including the computational grid approach. The second part discusses the flow around generic swept wing configurations with round leading edges of constant aspect ratio. The changes of the geometry are the leading edge contour radius along the span as well as the wing sweep. Sensitivity studies will be conducted regarding the geometric parameters by changing the angle of attack and Mach number. This results in design sensitivities regarding the behavior of the vortical flow topology as well as for the aerodynamic behavior. For the sensitivity study presented in this paper approximately 100 calculations have been conducted as listed in **Table 1**.

II. Numerical Method

For the present work the Reynolds-averaged NavierStokes(RANS) flow solver DLR TAU is used. TAU is a CFD software developed by the DLR Institute of Aerodynamics and Flow Technology.[54–57] The flow solver TAU solves the compressible, three-dimensional, time-accurate Reynolds-Averaged Navier-Stokes equations using a finite volume formulation. The code is based on a hybrid unstructured-grid approach to be able to handle structured and hybrid computational grids, which makes use of the advantages offered by prismatic grid structures applied to resolve the viscous shear layer close to the wall, and the flexibility in grid generation offered by unstructured grids. The compressible equations in full conservation form are discretized in space by a second-order accurate finite-volume method. The basic version of TAU is using a cell-vertex metric with a dual-grid approach in order to make the flow solver independent from the cell types used in the initial grid. Within TAU typical Jameson-type, Matrix dissipation and several upwind schemes can be used, all described by Jameson et al.[58]

The current simulations have been performed using the steady state and unsteady dual time-stepping approach. The dual time stepping approach was used in case no steady state solution was found. Therefore, the solution is provided by averaging over a certain time period for an unsteady calculation. For the numerical simulations the one equation Spalart-Allmaras turbulence model (SA)[59] in its negative formulation has been applied. The SA-neg version allows in comparisoin to the orgininal formulation of the turbulence model particularly negative values of the transport turbulence quantities.[60] This modification should lead to a more efficient solution of the equation without changing the dedicated aerodynamic solution.

The current approach is identified as a best practice for the flow solver DLR TAU. However, in AVT-183 qualitatively good results have been achieved to predict the separation onset conditions using other flow solvers and applying different turbulence models.[48,49,53,61]

III. Wing Geometries

To investigate the flow physics and aerodynamic behavior of swept wings with round leading edges in a systematic manner generic wing configurations have been defined. The following approach provides a discrete view on several aspects observed in the previously discussed applications regarding the effects of the wing geometry, leading edge contour and onflow conditions on the flow physics and aerodynamic behavior.

With this regard for the present work different generic wing geometries with constant aspect ratio have been defined. They represent the geometric characteristics of the previously investigated configurations like the SACCON. Beside the constant aspect ratio of the wings, the airfoil profiles have a constant relative thickness. Thus the results are independent from these two geometric parameters. In the following section the applied profiles and wing plan forms will be described.

The geometry chosen for the numerical studies is based on a NACA-64A-005 profile. It is a symmetric profile with a maximum thickness location at 40% and a maximum thickness of 5% as percent of the chord. This chosen airfoil is taken as a good compromise to represent the characteristics of common applied airfoils for military applications.

A CST (Class Shape Function) method has been used to apply different leading edge contour radii. With the parametric CST method the profile contour at the leading edge was changed in a way that downstream a continuous curvature is provided. A detailed description of the method is given by Kulfan[62] and Kunze et al.[63]

The applied profiles are plotted in **Figure 3**. The NACA profile in its original shape has a radius at the leading edge of r = 7.5mm related to a chord length of c_{ref} = 5m. This leads to a non-dimensional leading edge contour radius of $r_N = r/c_{ref}$ = 0.0015. **Figure 4** show the different leading edge geometries for the applied profiles in detail in comparison to the original NACA-64A-005 contour. For the wings discussed in this paper five different profiles with contour radius values of r_N = 0.001, 0.002, 0.003, 0.004 and 0.005 have been applied.

The wing plan forms used have a leading edge sweep of $\varphi = 45°$, $\varphi = 53°$, $\varphi = 60°$ and $\varphi = 65°$. The wing semi span s is 12m and the wing reference length l=c_{ref} is identical with the root chord of c_r = 5m for all different sweep angles. The wing configurations have a round trailing edge and a constant aspect ratio of $AR = b^2/A$ of 4.8. In the **Figures 5** to **8** the plan forms of all tested wings are depicted. The considered sweep angles are in the typical range of current military configurations, as for example the Boeing X-47 (φ = 30 and 55°),[64] Dassault Neuron ($\varphi = 57°$),[65] Eurofighter Typhoon ($\varphi = 53°$)[66] or Boeing F-22 ($\varphi = 42°$).[67]

IV. Computational Grids

For the computational grid generation the Software–System Centaur^{TM} developed by CentaurSoft[68] has been applied. For all tested configurations symmetric boundary conditions will be considered only, by using symmetry plane boundary conditions at the wing root.

For the different test configurations listed in **Table 1**, 16 hybrid meshes have been generated. For all meshes the parameters of the grid generator have been kept constant to achieve a comparable discretization for all configurations. The parameters are for example the number of prismatic layers, the initial wall distance, the cell size of the surface triangulation as well as the cell size of the tetrahedral within the source around the wing to resolve the vortical flow field sufficiently.

Table 2 provides the grid generation parameters. The overall number of grid points varies due to different sweep angles φ, thus the volume source is increasing with increasing sweep angle. The grid size for the configurations with 53° to 65° sweep angle is about $30 \cdot 10^6$ and for 45° approximately $18 \cdot 10^6$.

Figure 9 shows an example of the discretization of the surface at the leading edge along the wing span for the configuration with constant contour radius of r_N = 0.003. The resolution is getting higher towards the leading edge get a sufficient refinement of the leading edge curvature.

In **Figure 10** the overall grid topology is depicted. It can be seen that on the upper side of the wing a field source is applied. This source provides the refinement to resolve the vortical flow on the upper side of the wing. The field source extends over the whole wing span. On the upper right corner in Figure 10, the discretization of the prismatic layer is shown in detail. For all computational grids the prismatic layer consists of 35 layers to resolve the boundary layer flow.

V. Numerical Results

In this chapter the numerical results of the sensitivity studies of the swept wings with round leading edges will be analyzed and discussed. Focus of the studies are the flow topology of the vortical flow depending on the contour radius r_N at the leading edge along the span, the leading edge sweep angle φ and the angle of attack α. In addition the influence of the onflow Mach number on the flow topology will be discussed.

As a reference for the following investigations typical subsonic operational onflow conditions of military aircraft have been chosen. These operational points have been derived from typical missions used in DLR projects to assess the performance of military aircraft.[69] The onflow Mach number is M_∞ = 0.4 and the operational assumed altitude is 4000m. With these parameters the flight Reynolds number is $Re_\infty = 52.6 \cdot 10^6$ taking the chord length c_{ref} = 5m as the reference length. These assumptions represent relevant compressible flow conditions and should avoid transonic effects, which would provide additional effects and beyond the scope of this work. The investigations by Zimper et al.[36,37] regarding transonic effects on the SACCON configuration should be consulted for discussions of the impact

of compressible flow effects. For all calculations the Spalart-Allmaras (SA) turbulence model has been applied and fully turbulent flow conditions are considered to avoid laminar flow effects. The separation onset under laminar flow conditions or transition effects are not part of the current investigations.

Figures 11 and **12** show the y^+ distribution on the upper side of the wing for two different configurations and flow topologies. For the case in Fig. 11 a vortex has developed at the leading edge and the y^+ values are one and smaller in all areas apart from the area below the vortex axis. Fig. 12 shows a case with fully attached flow on the upper side of wing and all y^+ values are much smaller then one apart from the wing tip area where the tip vortex occurs. Due to the acceleration of the flow under the vortex, y^+ values higher than one occur. Adapting the grid in these areas is challenging with the applied grid generator. For the present investigations however it is actually important to have a sufficient resolution at the leading edge to predict the separation onset physics sufficiently.

The CFL number for all calculations is 1.5 and a multi-grid cycle to accelerate the convergence has been applied. All calculations have been started considering steady state conditions and a local time stepping approach was used. For several cases no converged steady state solution have been achieved an unsteady dual time stepping approach has been used. The physical time step Δt of the unsteady calculation has been determined as 0.005s and was chosen to be large enough for damping higher frequency effects, but small enough to resolve major flow phenomena like vortex breakdown. In none of the cases has vortex breakdown been observed at the considered onflow conditions. In order to get the final results the unsteady solutions have been averaged over a real time period of 2s, which is in the same range of time averring in wind tunnel tests.

The calculations have been conducted on the DLR $C^2A^2S^2E$-Cluster at DLR in Braunschweig. The DLR $C^2A^2S^2E$-Cluster is a 560 compute node cluster. Each node is based on two Intel IvyBridge processors (Intel E5-x2695v2, 2,4 GHz) and includes 24 cores. Approximately 100 calculations have been done on 10 nodes of 24 processors each. For the steady state calculations approximately 15.000 iterations were necessary to achieve a converged solution. For the present calculations this means a four order of magnitude convergence of the density residual and the lift and pitching moment coefficient did not change anymore over the final 5000-10000 iterations. One typical calculation needed 21h or 5000 processor hours. For the unsteady calculations the same resources have been used. The overall time for one averaged solutions was 25h or 6000 processor hours.

A. Flow Physics at round leading edges

In this section the detailed flow physics in the vicinity of the flow separation at the leading edge will be discussed. The characteristic flow physics at the round leading edge can be observed in all test cases in the present work. Within the NATO/STO Task Group AVT-183 on *Reliable Prediction of Separated Flow Onset and Progression for Air and Sea Vehicles* the seperation onset flow physics and topology was also analaysed. In comparison to the present results in AVT-183 only one particular test case at a certain angle of attack was analysed. To be able to determine the location of the separation onset and to decribe the flow topology the nomenclature applied by Frink[41] from AVT-183 was taken as a reference for the discussion of the following observations.

In **Figure 13** the result of a CFD calculation of the AVT-183 $\varphi = 53°$ delta wing published by Frink is depicted. **Figure 14** shows a corresponding solution for the 53° swept wing with a leading edge radius of r_N=0.004 at α = 11°. Both figures show the same characteristic flow topology.

For the delta wing as well as for the swept wing an area of attached flow exists at the round leading edge between the separation line (*converging streamtraces*) and the attachment line (*diverging streamtraces*). This area is called the area of *incipient separation*. In detail this area of *incipient separation* is limited by the extended surface streamline of the separation and attachment line towards the leading edge. The flow in this area or gap is attached. However, the flow in the boundary layer can be characterized as rotating flow which feeds the progressing vortex from the leading edge further downstream. The streamlines in gray and blue in Fig. 14 are related to the separation of the vortex directly at the leading edge. The streamtraces in red are the ones from the gap which are turning downstream by 180° and are feeding the leading edge vortex underneath the vortex core. Those in black can be assigned to the attached flow beyond the attachment line.

Figure 15 shows the numerical results for another swept wing case. Depicted are the surface streamlines in the upper part of the picture and the streamlines in the flow field in the lower part, starting at the leading edge close to the wall. In the upper part the limiting extended surface lines from the separation and attachment line are shown as well as the attached gap flow. In the lower part it can be fully observed how the attached streamline from the area of *incipient separation* feeds the leading edge vortex underneath the vortex core.

In **Figure 16** the angle of attack is increased by keeping the leading edge radius r_N and the onflow conditions constant. The increase of the AoA leads to a reduction of the attached flow area of *incipient separation*. A similar effect can be observed reducing the leading edge radius from r_N = 0.003 to 0.002 at constant AoA which is shown in the results in **Figure 17** and **18**.

In the previous discussions it was examined that the location of the separation line onset point could not be described as a particular point. Therefore a criterion for the following studies is needed to determine the location of the leading edge vortex onset point. As from the previous observations, the onset point of the separation line cannot be

centralized into one particular point but emerges from an array of converging streamlines. In this paper we will adopt again the criteria defined by Frink[41] as a suitable approach. Frink is determining the c_P distribution at the leading edge ($c_{P_{le}}$) and defines the location where the vortex occurs as the minimum $c_{P_{le,min}}$ of this distribution. This approach is shown in **Figure 19**. In addition it can be observed that the $c_{P_{le}}$ distribution has a point of inflection beyond $c_{P_{le,min}}$ along the leading edge. This increase of $c_{P_{le}}$ indicates a loss in suction force at the leading edge which will be compensated by an increased suction induced by the vortex on the upper side of the wing. This applied approach is in line with the analogy described by Polhamus.[70] **Figure 20** shows a result where the $c_{P_{le}}$ characteristic has no point of inflection. In these cases the $c_{P_{le}}$ distribution has a continuous characteristic. Hence the flow can be assumed to be fully attached or as a flow with no separation occurring at the leading edge.

B. Effect of angle of attack

1. Configuration with constant leading edge

First the numerical results of a wing with constant leading edge radius along the span will be discussed. The chosen test case has a leading edge radius of $r_N = 0.002$. In the following figures the surface pressure distribution on the upper surface and the surface streamlines are depicted. The plotted surface streamlines evolve from the skin friction distribution close to the wall.

For an angle of attack of $\alpha = 8°$ in **Figure 21a** it can be observed that the flow is fully attached. Only at the wing tip a tip vortex can be identified by the pattern of the surface streamlines. Furthermore, there is an area of converging streamlines at the trailing edge which indicates a pending separation. This kind of separation will be stated as a thickness separation in the following discussion. This thickness separation occurs close to the wall and is covered by the outer flow, which will be shown later. However, in the following discussion this kind of flow topology will be called a fully attached flow or a topology with a thickness separation, in contrast to a flow topology with a vortex appearing at the leading edge.

The flow topology changes suddenly with an increasing AoA of just about a quarter of degree. **Figure 21b** shows the surface pressure distribution and streamlines at $\alpha = 8.25°$. The flow separates at the leading edge and a vortex is present. The location of the leading edge vortex depends on the AoA. For $\alpha = 10°$ in **Figure 21c** the vortex onset point has been shifted upstream towards the leading edge. Upstream of the attachment line up to the wing root the flow remains attached. In addition, outboard of the wing, the flow separates at the trailing edge and a trailing edge vortex occurs, shifting the attachment line to the upper side of the wing. These results show that the onset point of the vortex at the leading edge moves towards the apex with increasing AoA.

The location of the vortex onset point can be evaluated by the leading edge pressure distribution. In **Figure 22** the $c_{P_{le}}$ distribution for an AoA of $\alpha = 8°$; 8.25° and 10° is depicted. For $\alpha = 8°$ a continuous $c_{P_{le}}$ characteristic is present which corresponds to the fully attached flow already discussed in the previous section. For $\alpha = 8.25°$ and 10° the $c_{P_{le}}$ characteristic has a point of inflection and a minimum at $y/s = 0.454$ and $y/s = 0.145$ respectively.

In **Figure 23** a different representation of the results is chosen. The view is no longer perpendicular but has been turned 30° around the y-axis to get a better image of the leading edge flow. Beside the pressure distribution the streamlines in the flow field are shown. The origin of the streamtraces is located at the leading edge close to the wall. The plotted streamlines give a three dimensional image of the flow topology on the upper side of the wing.

In Fig. 23a the case at an AoA of $\alpha = 8°$ is shown again. The flow is fully attached and only the tip vortex is present. Increasing the AoA to $\alpha = 8.25°$ in Fig. 23b there is a vortex present at the leading edge and the onset point moves towards the apex with increasing α, see Fig 23c for an AoA of $\alpha = 10°$.

In addition, it can be observed that for $\alpha = 8.25°$ the vortex axis develops from the leading edge to the side edge at the wing tip. At that point it is turned downstream by the main flow. For $\alpha = 10°$ the vortex reaches first the trailing edge, gets diverted, and then moves parallel to the trailing edge towards the wing tip. This is caused by the trailing edge vortex. In this case the attachment line is not located at the trailing edge anymore but moves upstream with increasing AoA. The development of the attachment line and the location of the vortex due to the trailing edge vortex can be identified in Fig. 21c.

2. Configurations with different leading edge radii

In the following section the test cases will be extended to different constant leading edge radii along the span. First of all, the cases with an AoA of $\alpha = 10°$ will be discussed to discuss the progression of the vortex with changing leading edge contour curvature. In **Figure 24** the results for four different leading edge radii of $r_N = 0.001$, 0.002, 0.003 and 0.004 are presented. The onflow conditions did not change in comparison to the previous section ($M_\infty = 0.4$, $Re_\infty = 52.6 \cdot 10^6$).

For the case $r_N = 0.001$ in Fig. 24a the vortex onset point at the leading edge is located at $y/s = 0.05$. This can be evaluated from the pressure distribution plotted in **Figure 25**. Increasing the leading edge radius from $r_N = 0.001$ to $r_N = 0.003$ like in Fig. 24a-c results in the vortex onset point moving towards the apex along the leading edge.

A further increase to $r_N = 0.004$ results in a completely attached flow topology over the wing (see Fig. 24d). The AoA is actually not high enough to cause a leading edge separation. The pressure distribution in Fig. 25 reflects this condition. It provides a continuous characteristic with no point of inflection. A similar result of a fully attached flow condition has already been discussed in the previous section for $r_N = 0.002$ at $\alpha = 8°$ in Fig. 21a. For both cases there already exists a structure of converging surface streamlines indicating a rotation in the boundary layer flow.

In **Figure 26** the field streamlines are plotted for an increased AoA from $\alpha = 11°$ to 12° for the case with $r_N = 0.004$ and for 12° for the configurations with $r_N = 0.005$. Now a vortex occurs at the leading edge for the case with $r_N = 0.004$ (Fig. 26a). Increasing the AoA from $\alpha = 11°$ and 12° (Fig. 26b) at constant r_N shifts the vortex onset location at the leading edge upstream towards the apex. If the leading edge contour radius will be increased at a constant AoA of $\alpha = 12°$ from $r_N = 0.004$ to $r_N = 0.005$ the opposite behavior can be noticed. The vortex onset point for $r_N = 0.005$ is located further downstream (compare Fig. 26b with 26c).

To provide an overview of the results in **Figure 27**, the $c_{P_{le}}$ distribution is plotted for all contour radius cases for the limit AoA a vortex initially occurs at the leading edge. Evaluating this plot regarding the location of the leading edge vortex onset location and all other AoA results the diagram in **Figure 28** can be derived. The plot shows the progression of the vortex onset location with increasing AoA for all leading edge contour radii.

Summarizing the previously discussed results it can be stated that the generation of the vortex is pushed to higher AoA with increasing leading edge contour radius. In case a vortex is already present an increasing r_N leads to a further downstream location of the onset point. Finally, the vortex onset point is moving upstream along the leading edge towards the apex with increasing AoA.

3. Configurations with variable leading edge radius

After verifying configurations with constant radius in the previous section, configurations with variable leading edge radius along the span shall now be discussed. The sweep angle chosen for the following test cases is again $\varphi = 53°$ as well as the onflow conditions. The leading edge contour radius in the present test cases is increased and decreased linearly along the span. For the first configuration with increasing r_N from 0.001 at the root up to 0.003 at the wing tip. The second configuration has a decreasing r_N distribution from 0.003 at the wing tip to 0.001 at the wing root. The numerical results for an increasing r_N are presented in the **Figure 29** for angles of attack of $\alpha = 7.5°$, 7.75°, 8° and 10°.

For an AoA up to 7.5° the flow over the wing is fully attached. However, in Fig. 29a the surface streamlines converge at the trailing edge at a spanwise location of $y/s = 0.5$ which indicates the beginning of separation. If the AoA will be increased slightly to $\alpha = 7.75°$ (Fig. 29b), the topology changes and the flow separates at the leading edge. The generated vortex is located at $y/s = 0.179$. The vortex onset location evaluates from the leading edge pressure distribution given in **Figure 30**. For a further increase of the AoA the vortical flow topology remains and the vortex onset point moves towards the apex.

The flow topology in the vicinity of the wing root for angles of attack of $\alpha \geq 7.75°$ is comparable to the one with a constant r_N of 0.001 (see Fig. 24a). The flow physics at the outer wing, however, looks different; the separation line is shifted to the upper side of the wing surface at approximately $y/s = 0.6$ (see Figs. 29b and c). The reason for that is the increased leading edge contour curvature towards the wing tip. As shown in previous cases with constant r_N the onset of separation at the leading edge is pushed to higher AoA with increasing contour radius.

This effect can be identified in the characteristics of the $c_{P_{le}}$ distribution in Fig. 30 as well. The pressure coefficient is decreasing slightly again for a spanwise location of $y/s > 0.7$, which is caused by the attached flow around the leading edge causing higher local flow velocities.

The vortex topology at the outer wing is showing in the Figs. 29b and 29c and can be characterized as a double branch vortex as indicated by the double s-slope structure in the surface streamlines. **Figure 31** shows the flow topology at the two slices ① and ② in Fig. 24b. In Fig. 31① there is only the main vortex present. In Fig. 31② the main vortex is connected to a week outer vortex. This double branch flow structure almost disappears completely for higher angle of attack as seen in Fig. 29d for an AoA at $\alpha \geq 10°$ and the separation is located at the leading edge over the entire span.

In **Figure 32** the results of the opposite case of a decreasing leading edge radius along the span are plotted. For angles of attack from $\alpha = 6°$ to 10° the surface pressure distribution as well as the surface streamlines on the upper wing are depicted.

In comparison to the case of an increasing leading edge radius, the separation at the leading edge occurs first at the outer wing at an AoA of 6° (see Fig. 32a). This corresponds to the case for $r_N = 0.001$ plotted in Fig. 28, because for both cases the same leading edge radius applies at the outer wing. The vortex onset point moves upstream with increasing AoA towards the apex according to the cases discussed previously. Opposite to the case of an increasing r_N, the separation line remains at the leading edge for all examined AoA and the flow topology is similar to the cases with constant r_N along the span.

Figure 33 demonstrates that, for similar AoA but for different radius leading edge distributions cases, a comparable flow topology occurs. The $c_{P_{le}}$ distributions are plotted for a case with decreasing r_N at $\alpha = 8°$ from Fig. 32c in

comparison to the configuration with a constant r_N of 0.002 in Fig. 21b at $\alpha = 8.25°$. For both cases the vortex onset locations at the leading edge are located approximately at the same position y/s. For the case with decreasing r_N this location corresponds to the position y/s where the local r_N is 0.002.

C. Aerodynamic behavior

In the following section the influence of the flow topology over the wing on the aerodynamic behavior will be discussed. The investigations are also related to the non-linear effects occurring for the SACCON configuration[34] discussed in the background section, see Fig. 1. For the determination of the pitching moment coefficient the Moment Reference Point (MRP) is chosen as the x-coordinate of the center of area. The y-coordinate is zero assuming the wing is taken as a half wing representation of a full span wing. The location of the MRP is plotted in **Figure 34**.

Figure 35 shows for all configurations with constant and variable leading edge radius distribution the lift coefficient c_L versus AoA α. Highlighted are the angles of attack a vortex initially occurs at the leading edge. The values are corresponding to plots in Fig. 28. It can be seen that the characteristics of the lift coefficient for the cases with $r_N = 0.001$ and with decreasing r_N are almost linear. For all others the characteristics are nonlinear; especially the onset of separation and related location of the leading edge vortex causes a discontinuous kink in the characteristic.

The nonlinear characteristic of the lift coefficient is caused by the developing vortical flow over the wing. **Figure 36** shows the c_P distribution and the surface streamlines on the upper side of the wing for the case with $r_N = 0.004$. The vortex at the leading edge develops first at an AoA of $\alpha = 10.9°$ (Fig. 36c). However a separation already occurs outboard at an AoA of $\alpha = 10.5°$ (Fig. 36b) and leads to a slightly reduced lift coefficient. The lift coefficient increases further after the vortex at the leading edge is fully developed and has compensated for the reduction in linear lift completely.

In **Figure 37** the pitching moment coefficient c_M versus the AoA α is plotted. The angles of attack are highlighted again where the vortex initially occurs at the leading edge. For all configurations the discontinuous kink in the characteristics can be observed, which have been applied for the SACCON configuration as well.[34] The reason for this nonlinear behavior (kink) is the changing load distribution caused by the separation onset and related location of the vortex.

In **Figure 38** the shift of the load distribution should be addressed by the c_P distribution in front and beyond the MRP. The c_P distribution and the surface streamlines on the upper side of the wing are plotted for the case with r_N = 0,005 for $\alpha = 11.5°$, 11.75°, 12° and 13°. In addition the reference location of the MRP from Fig. 34 is given as well as two more locations 15% behind and upfront of this position. In **Fig. 39** the related pitching moment curve is plotted for three different MRP locations.

First the reference case should be discussed. For $\alpha = 11.5°$ in Fig. 38a there is no vortex developed at the leading edge and the related pitching moment value is located upfront of the kink (location where pitching moment increases suddenly). In Fig. 38b for $\alpha = 11.75°$ a vortex occurs at the leading edge and the onset position is almost located completely behind the MRP. This changes the load distribution in a way that the pitching moment is reduced as seen in Fig. 39. For $\alpha = 12°$ in Fig. 38c this effect has increased, which can be identified by the much lower pressure values behind the MRP in comparison to the case at $\alpha = 11.75°$. The vortex onset point is in fact already located upfront the MRP, but the low pressure footprint of the vortex influences mainly the area aft the MRP. In Fig. 39 this situation is represented by the lowest point of the kink in the pitching moment curve. For $\alpha = 13°$ in Fig. 38d, the vortex onset point at the leading edge is located far upfront of the MRP. The low pressure footprint of the vortex influences primarily the area in front of the MRP. This leads to an increasing pitch up behavior as seen in Fig. 39 for $\alpha = 13°$.

If the location of the moment reference point is shifted 15% towards the wing apex as shown in Fig. 39 the overall pitching moment is reduced versus the AoA. In this case the values are negative for all plotted AoA and a completely pitch down behavior is present. The nonlinear effect due to the vortical flow increases in comparison to the reference case because the load distribution is in all cases higher aft the MRP then upfront. The opposite behavior can be observed by shifting the MRP 15% behind the current reference position. The overall pitching moment values are shifted to higher values. This causes an increased pitch up behavior. The nonlinear characteristic is reduced because there is only a minor influence of the vortex on the load distribution aft of the MRP.

Furthermore, it can be noticed that the c_M minimum suddenly occurs in some cases. **Figure 40** shows a comparison of the pitching moment coefficients of the cases with $r_N = 0.003$, 0.004 and 0.005. The range of the kink in the pitching moment characteristic increases with increasing r_N. For higher leading edge radii the characteristic is more transient. The reason for that it that the vortex for $r_N = 0.005$ influences the load distribution downstream of the MRP for a wider AoA range then for smaller r_N.

For the configuration with increasing leading edge radius the vortex occurs initially far upstream of the MRP. Hence the impact on the load distribution downstream of the MRP is marginal and the pitching moment characteristic is fairly linear. For The configuration with decreasing r_N the vortex first occurs far downstream of the MRP in comparison to the case with $r_N = 0.005$. However, this vortex is much weaker in its impact and causes only a small discontinuity because of merely small load change.

The case with decreasing leading edge radius is comparable with the tip vortex flow physics on the SACCON.

Concerning the aerodynamic stability behavior it is demonstrated that the nonlinear pitching moment characteristic of the SACCON occurs also for configurations with constant leading edge contour and not only for variable contour distributions. This is caused by a comparable load change over the wing, due to an AoA dependent vortex onset location and movement.

D. Effect of the leading edge sweep

The influence of the sweep angle will be demonstrated using results from three configurations with constant leading edge radii of $r_N = 0.002$, 0.003 and 0.004. Four different sweep angles of $\varphi = 45°$, 53°, 60° and 65° have been examined. The aspect ratio is constant, being $AR = 4.8$ for all wing configurations.

Before discussing the results the effect of a changing sweep angle should be explain theoretically. **Figure 41** shows the influence of the sweep angle on the circulation along the span. Plotted is the circulation for a non-swept wing ($\varphi = 0°$) and a swept wing, with a sweep angle of $\varphi = 45°$. For the swept wing the lift distribution has its maximum at the outer wing. Due to the wing sweep, the location of the local lift maximum is shifted outboard in comparison to the non-swept case. For the swept wings investigated in this paper this means, that with increasing sweep angle the location of maximum aerodynamic load is shifted outboard.

Figure 42 shows the results of panel method calculations for all swept wings discussed in this paper in comparison to the non-swept case. Plotted is the local lift coefficient along the span as well as the locations of the local lift maxima. It can be observed that with increasing sweep angle the maximum lift is shifted outboard. While this examination is just a 2D non frictional approach, it explains in principle the separation sensitivity.

In the **Figure 43** the results for the configuration with $r_N = 0.003$ at an AoA of $\alpha = 10°$ for different sweep angles are presented. Plotted are again the surface pressure and streamlines, as in the previous sections. As a reference case the configuration with a sweep angle of $\varphi = 53°$ is chosen, depicted in Fig. 43a.

The assessment of the $c_{P_{le}}$ distributions for an AoA of $\alpha = 10°$ in **Figure 44** shows that the vortex onset for $\varphi = 53°$ is located at approximately $y/s = 0.38$ and for $\varphi = 45°$ at approximately $y/s = 0.18$. A reduction of the sweep angle at constant α is shifting the vortex onset location upstream towards the apex.

Increasing the sweep angle from $\varphi = 53°$ to $\varphi = 60°$ as depicted in Fig. 43c, the flow physics changes on the upper side to a fully attached flow topology. The converging surface streamlines which can be observed indicating a starting separation close to the surface within the boundary layer covered by the outer flow. This kind of separation corresponds to the weak thickness vortex which has been observed in the investigations of the SACCON configuration by Schütte et al.[34]

For a higher leading edge sweep of $\varphi = 65°$ (Fig. 43d), the flow topology is similar to the one for $\varphi = 60°$. A separation line is formed on the upper side of the wing, but in comparison to the case with $\varphi = 60°$ it does not end at the side edge. The separation line is moving towards the apex. The position of the vortex onset point is located where the separation line of the thickness vortex interferes with the leading edge at $y/s = 0.82$.

In **Figure 45** the flow topology in the field is shown. For the configuration with a sweep angle of $\varphi = 60°$ in Fig. 45c it can be noticed that only the tip vortex occurs and the separation identified is just a thickness separation close to the wall covered by the outer attached flow.

Looking at the $c_{P_{le}}$ distribution in Fig. 44 for the case with $\varphi = 60°$ the continuous characteristic is plotted indicating no separation at the leading edge. For $\varphi = 65°$ there is no clear interpretation. The minimum in $c_{P_{le}}$ is not as specific to identify the location of the separation onset point but the characteristic has a point of inflection which indicates a vortex onset at the leading edge. In this case the location of the vortex onset location can be identified by extrapolating the footprint of the vortex towards the leading edge. This approach leads to an onset point location at $y/s = 0.82$.

For sweep angles of $\varphi = 60°$ and 65° another effect can be observed. Opposite to the cases with $\varphi = 53°$, the area of incipient separation propagates from the separation line upstream to the wing root. The attachment line in both cases is located beyond the trailing edge and not on the upper side of the wing, as for the case with $\varphi = 45°$ and 53°.

In **Figure 46** as well as in **Figure 47** the results for an AoA of $\alpha = 11°$ are depicted. For $\varphi = 45°$ (Fig. 46a and 47a) the location of the vortex onset point is shifted upstream towards the apex. For a sweep angles of $\varphi = 60°$ at $\alpha = 11°$ (Fig. 46c and 47c) a vortex develops at the leading edge in contrast to the case at $\alpha = 10°$. The onset location is located further downstream in comparison to the case with $\varphi = 53°$, see Figs. 46b and 47b. The attachment line is located beyond the trailing edge in the front part of the wing which indicates that the area of incipient separation expands from the separation line up to the wing root. For $\varphi = 65°$ (Fig. 46d and 47d) the flow topology remains with increasing AoA. The vortex onset point is shifted downstream in comparison to the case with $\alpha = 10°$; the attachment line remains beyond the trailing edge. In addition, a secondary separation occurs at the outer wing.

Finally the effect of the sweep angle by increasing the leading edge radius contour will be demonstrated. In **Figure 48a** and **b** the flow field streamlines for an increased leading edge contour radius of $r_N = 0.004$ are plotted for sweep angles of $\varphi = 60°$ and 65° at an AoA of $\alpha = 11°$. The results are comparable with those in Fig. 45c and 45d. The comparison shows that starting from the results presented in the Fig. 47c and d, a decreasing AoA (α) or an increasing leading edge radius contour (r_N) leads to a similar flow topology.

Figure 49 shows the evaluation of the $c_{P_{le}}$ distribution for the previuos discussed solutions. The characteristics of the $c_{P_{le}}$ distribution are similar for the related sweep angles of $\varphi = 60°$ and $\varphi = 65°$. There is only a small shift to smaller $c_{P_{le}}$ values if the leading edge contour radius decreases due to slightly higher velocities around the leading edge.

E. Effect of the Mach number

The following section discusses the effect of a changing Mach number on the flow topology over the wing. For these investigations the configuration with a leading edge radius contour of $r_N = 0.003$ with four different sweep angles of $\varphi = 45°$, 53°, 60° and 65° have been studied. The reference AoA is $\alpha = 11°$ and the reference Mach number is $M_\infty = 0.4$. For determination of the Mach number effect three additional Mach numbers of $M_\infty = 0.3$, 0.5 and 0.6 have been selected. The Reynolds number is kept constant at $Re_\infty = 52.6 \cdot 10^6$.

Figures 50 and **51** present the result for a sweep angle of $\varphi = 45°$ with changing Mach number. The results show that reducing the Mach number to $M_\infty = 0.3$ (Fig. 50a and 51a), the vortex disappears and the flow topology over the wing can be characterized as fully attached, although a small separation occurs but is covered by the outer flow field as indicted by the surface streamlines in Fig. 51a.

In **Figure 52** the related $c_{P_{le}}$ distribution is plotted. For $M_\infty = 0.3$ the characteristic continuous $c_{P_{le}}$ distribution is shown. For $M_\infty = 0.4$ a characteristic with a minimum at y/s = 0.135 is present. Thus the location of the vortex onset at the leading edge can be evaluated. For a Mach number of $M_\infty = 0.5$ and 0.6 the location of the vortex onset cannot be identified explicitly by means of the $c_{P_{le}}$ distribution. The local minima are not exactly correlating to the onset point locations. Looking at the vortex formation and surface pressure distribution in the Figs. 50c/d and 51c/d it seems to be that the limit case is already reached where the vortex onset point is located at the apex.

In the **Figures 53** and **54** the results for a sweep angle of $\varphi = 53°$ are presented. The Mach number effects are comparable to the ones observed for the case with $\varphi = 45°$. A decrease of the Mach number from $M_\infty = 0.4$ to 0.3 leads to a large change in the flow topology from a vortical flow at the leading edge to an attached flow over the wing (see Fig. 54b and 54a). For an increasing Mach number from $M_\infty = 0.5$ to 0.6 the flow topology does not change in comparison to the case with $M_\infty = 0.4$. But it can be observed that the vortex onset point at the leading edge is shifted with increasing Mach number towards the apex.

Figure 55 shows the corresponding $c_{P_{le}}$ distribution. The $c_{P_{le}}$ distribution delivers a clear prediction of the location of the leading edge vortex for $M_\infty = 0.3$ and 0.4 in the same manner as for the case with $\varphi = 45°$. For $M_\infty = 0.5$ and 0.6 the characteristic has a point of inflection, but has not a clear minimum to identify the vortex onset location. However, the range of minimum $c_{P_{le}}$ values matches quite reasonable with the position of the vortex onset locations.

In the **Figures 56** and **57** the results for the configurations with $\varphi = 60°$ and in **58** and **59** the results for $\varphi = 65°$ are depicted. For the case of a sweep angle of $\varphi = 65°$ the flow topology remains with decreasing Mach number. The vortex onset point at the leading edge is shifted downstream towards the wing tip along the span. For the configuration with $\varphi = 60°$ the same behavior as for $\varphi = 53°$ occurs where a reduction of the Mach number leads to a fully attached flow over the wing.

The effects regarding a changing Mach number is comparable to the effects observed by changing the angle of attack or the leading edge contour radius. In case of an already existing leading edge vortex, a reduction of the onflow Mach number or AoA is shifting the vortex onset point location towards the wing tip. In both cases the separation at the leading edge disappears and the flow topology changes to a fully attached flow if the Mach number or AoA is sufficiently small respectively. An opposite behavior applies for an increasing Mach number or leading edge contour radius at a constant AoA. In both cases the vortex onset point is shifted towards the wing root.

The reason for the separation at the leading edge due to an increasing Mach number will be given by evaluating **Figures 60** and **61**. The pressure distribution over wing from Fig. 53 is plotted at two locations y/s = const. In Fig. 60 the pressure distribution extracted from the TAU solution in Fig. 53a, plotted in red. The green curves are the TAU results of the pressure distribution for the transformed wing by applying the *Prandtl-Glauert-Ackeret* rule with a correction parameter derived with a Mach number of $M_\infty = 0.4$. The rule expresses that the compressible pressure distribution can be evaluated by the results of a transformed wing. The transformed wing results by reducing the span of the wing in y-direction with a scaling factor of $\sqrt{1-(M_\infty)^2}$. This leads to a transformed wing with an increased sweep angle of $\varphi = 55.5°$ and a reduced aspect ratio of $AR = 4.4$. The compressible pressure distribution derives by a calculation of the transformed wing at incompressible conditions ($Ma_\infty = 0$). In the present case $M_\infty = 0.3$ is taken as the incompressible conditions. Taking this assumption into account, it can be seen that the transformed wing solution provides a higher pressure gradient on the upper side of the wing, which forces the attached flow to separate at the leading edge.

In Fig. 61 the *Prandtl-Glauert-Ackeret* rule is applied to the pressure distribution itself. It can be observed that the result for $M_\infty = 0.4$ (blue) is similar to the one for the transformed grid in Fig. 60 (green). The black c_P distribution evaluates from a Mach number of $M_\infty = 0.6$. However the changes of the pressure gradient are quite small it has been shown before that the flow is fairly sensitive regarding separation by changing the onflow conditions slightly.

F. Sensitivities of the vortical flow for round leading edges

The results from the investigations regarding the influence of the angle of attack α, the leading edge contour radius r_N and sweep angle φ, as well as the Mach number M_∞, on the vortex topology development can be summarized into a sensitivity scheme. **Figure 62** shows the flow topology states depending on the four parameters. It is presented how the vortex onset point at the leading edge is moving along the span in case one of the four parameters is changing while the other three are kept constant. Two characteristic limit states are marked in the diagram. The first limit defines the state the vortex onset point has moved up to the apex. The second limit is the situation where the vortex at leading edge is vanished and a fully attached flow state is present or the flow is attached around the leading edge respectively.

There is one constraint regarding the sweep angle effect that there is only a fully attached flow present if the aerodynamic loads are small enough at the outer wing. Otherwise a reduction of the Mach number M_∞ or AoA α is necessary. Usually a wing twist towards the onflow direction is applied to reduce the local AoA and thus the load on the outer wing to avoid separation.

The results regarding the cases with variable contour distribution along the leading edge show comparable results as the study in Fig. 62 for constant leading edge contour. It can be shown that with a variable contour distribution the development and location of the vortex at the leading edge can be influenced additionally. With an increasing contour curvature towards the wing tip the vortex onset point can be shifted towards the wing root. A reduction along the span is shifting the onset point in the direction of the wing tip. This particular case is comparable to the situation for the SACCON configuration.

The sensitivity study can be taken to define the specifications of a new or existing design to determine the behavior of the flow topology at a certain state if one of the parameters α, r_N, φ or M_∞ will be changed. By adapting the flow topology conclusions can be drawn about possible changes of the aerodynamic behavior.

The aerodynamic studies with respect to the lift and pitching moment behavior provide an assessment about the influence of the vortical flow topology on the nonlinear aerodynamic characteristic. Beside the position of the vortex onset location on the load distribution, the location of the MRP is a major determining factor for the design influencing the nonlinear aerodynamics, and finally the stability and control behavior. These findings can provide a contribution for the redesign of the SACCON by changing it from principally a computational validation case towards a real flying aircraft configuration.

VI. Summary

The present paper discussed the results from investigations of the flow physics and aerodynamic behavior of swept wings with round leading edges. The outcome of this work provides a contribution for the design of configurations with swept wings having a round or variable contour leading edge along the span. Additionally, the present investigations deliver an improved understanding about the vortex development at the round leading edge. The applied wing geometries for the study are swept wings with a constant aspect ratio for all sweep angles. The wing profiles are based on a NACA-64A-005 airfoil manipulated with a CST method to adapt the leading edge contour radius.

Several publications of the author are used for the validation of the numerical method and grid generation approach and provide the validation for the RANS solver DLR TAU to justify the present numerical approach.

Opposite to swept, sharp leading edge wings, the separation line of a swept, round leading edge wing is not fixed at the leading edge. The origin of the separation and attachment line are separated from each other and the separation onset location depends among others on the angle of attack or leading edge contour. This was initially demonstrated for a wing planform with spanwise constant round leading edge contour and a sweep angle φ of 53°.

It was shown that the mechanism of the vortex flow development at the leading edge can be set in analogy to the investigations from Frink.[41] In case of a vortical flow at a round leading edge, a so-called incipient separation area occurs. The area of incipient separation is an attached flow area limited by the extension of the separation and attachment towards the apex. The attached flow in this area turns further downstream towards the mean flow direction and feeds the vortex underneath the vortex core. Additionally to the results from Frink[41] the author demonstrated that the range of the area of incipient separation varies with angle of attack and by changing the leading edge contour. A reduction of the AoA or an increasing leading edge contour radius leads to an extended range of the area of incipient separation.

In addition it was shown that with increasing AoA the location of the vortex onset point is moving towards the apex. At a certain AoA while decreasing α a limit state is reached where the flow region is fully attached over the entire wing or an attached flow around the leading edge is present, respectively. It was demonstrated by looking at different leading edge contour radii, that with increasing radius the development of the vortex is shifted to higher AoA. The same applies for an increasing leading edge contour radius which shifts the location of the vortex onset point further downstream up to the limit state of a fully attached flow.

Beside wing configurations with constant radius distribution the flow physics of wings with linear increasing and decreasing contour distributions have been explored. The flow around a configuration with increasing leading edge contour has the same behavior as the one with a constant r_N. The location of the separation onset is driven by the AoA

and local curvature. In case of a decreasing leading edge contour it can be observed that the vortex occurs first at the wing tip caused by the local small radius. For an increasing leading edge contour radius the vortex occurs first closer to the apex if the AoA is high enough.

For the investigations regarding the influence of the leading edge sweep different sweep angles have been applied. Beside the reference angle of $\varphi = 53°$, sweep angles of $\varphi = 45°$, $60°$ and $65°$ have been determined. It has been shown in the case of an already existing vortex at the leading edge, the vortex topology remains with decreasing sweep angle. A reduction leads to a movement of the vortex onset point towards the apex.

An increasing leading edge sweep shifts the vortex onset point location downstream towards the wing tip. In case the AoA is small enough the vortex vanishes and a fully attached flow topology is present. In case a vortex is present at the leading edge it can be observed that the area of incipient separation is extended up to the wing root. The attachment line is located beyond the trailing edge and the area of incipient separation is limited downstream by the extended separation line towards the leading edge.

Furthermore, the influence of the Mach number on the flow topology was examined. The effect on the flow topology by changing the Mach number is comparable with other parameters like the effect of the AoA variation at constant Mach number. The location of the vortex onset at the leading edge moves with reducing Mach number downstream towards the wing tip up to the limit state of a fully attached flow. An increasing Mach number shifts the vortex onset location in the direction of the apex.

The results of the sensitivity study regarding the geometric and onflow parameters are summarized in a diagram which can be taken to specify a new, or to assess and improve a given, wing design.

Beside the flow physics studies the influence of the flow topology on the aerodynamic behavior has been examined. For certain wing configurations investigated in the present work a partly similar aerodynamic behavior has been observed, as for the SACCON[34] configuration. The pitching moment behavior is very sensitive with respect to changes of the vortical flow topology. For several examples it has been demonstrated that a change of the flow from a fully attached flow to a separated flow with a vortex at the leading edge can cause significant nonlinear effects in the characteristics of the pitching moment. This nonlinear behavior depends on the location and strength of the vortex over the wing. This influences the load distribution caused by the vortex in front and behind the moment reference point of the configuration.

In summary, the present work provides a contribution for the deeper understanding of the vortical flow development of swept wing configurations with round leading edges. Interdependent flow topology related effects identified in previous investigations have been discussed separately and analyzed in detail. The mechanism of the flow physics regarding the vortex onset process was demonstrated in correlation to the work provided by Frink.[41] In addition to these investigations it was shown how the flow topology at the leading edge is changing by changing geometric and flow physical parameters.

The results of this paper provide a support for the design process of configurations with swept wings and round leading edges. The comprehensive sensitivity studies can be applied to assess the way a certain flow topology and aerodynamic characteristic will change by changing the presently discussed geometric and aerodynamic parameters

Acknowledgments

The author would like to offer special thanks to Prof. Dietrich Hummel for extensive and fruitfull discussions to conduct the present work. In addition the author would like to thank all members of the NATO STO/AVT Task Groups for their inspiring contributions, valuable discussions and friendship over the last several years.

References

[1]Hummel, D. and Redeker, G., "A new Vortex Flow Experiment for computer code validation," *RTO AVT Meeting Proceedings, RTO-MP-069-I*, 2001, pp. 8–1 – 8–31.

[2]Hummel, D., "The Second International Vortex Flow Experiment (VFE-2): Objectives and first results," *Journal of Aerospace Engineering*, Vol. 220, No. 6, 2006, pp. 559–568.

[3]Hummel, D., "Review of the Second International Vortex Flow Experiment (VFE-2)," *AIAA Paper 2008-377*, Jan 2008.

[4]Chu, J. and Luckring, J., "Experimental Surface Pressure Data Obtained on 65-Degree Delta Wing Across Reynolds Number and Mach Number Ranges," *NASA TM-4645*, Vol. 1-4, 1996.

[5]Le Roy, J. F., Rodriguez, O., and Kurun, S., "Experimental and CFD contribution – delta wing vortical flow understanding," *AIAA Paper 2008-380*, Jan 2008.

[6]Furman, A. and Breitsamter, C., "Turbulent and unsteady flow characteristics of delta wing vortex systems," *AIAA Paper 2008-381*, Jan 2008.

[7]Coton, F., Mat, S., and Galbraith, R., "Low speed wind tunnel characterization of the VFE-2 wing," *AIAA Paper 2008-382*, Jan 2008.

[8]Konrath, R., Klein, C., and Schroeder, A., "PSP and PIV investigations on the VFE-2 configuration in sub- and transonic flow," *AIAA Paper 2008-379*, Jan 2008.

[9]Luckring, J. M., "Initial experiments and analysis of vortex flow on blunt edged delta wings," *AIAA Paper 2008-378*, Jan 2008.

[10]Fritz, W., "Numerical simulation of the peculiar subsonic flow-field about the VFE-2 delta wing with rounded leading edge," *AIAA Paper 2008-393*, Jan 2008.

[11]Schiavetta, L. A., Boelens, O. J., Crippa, S., Cummings, R. M., Fritz, W., and Badcock, K. J., "Shock effects on delta wing vortex breakdown," *Journal of Aircraft*, Vol. 46, No. 3, 2009, pp. 903–914.

[12]Cummings, R. M. and Schütte, A., "Detached-eddy simulation of the vortical flow field about the VFE-2 delta wings," *Aerospace Science and Technology*, Vol. 24, No. 1, 2013, pp. 66–76.

[13]Crippa, S. and Rizzi, A., "Steady, subsonic CFD analysis of the VFE-2 configuration and comparison – wind tunnel data." *AIAA Paper 2008-397*, Jan 2008.

[14]Gürdamar, E., Ortakaya, Y., Kaya, S., and Korkem, B., "Some factors influencing the vortical flow structures on delta wings," *AIAA Paper 2008-394*, Jan 2008.

[15]Fritz, W. and Cummings, R. M., "What was learned from the numerical simulations for the VFE-2?" *AIAA Paper 2008-399*, Jan 2008.

[16]Schütte, A. and Lüdeke, H., "Numerical investigations on the VFE-2 65-degree rounded leading edge delta wing using the unstructured DLR TAU-Code," *Aerospace Science and Technology*, Vol. 24, No. 1, 2013, pp. 56–65.

[17]Rein, M., Höhler, G., Schütte, A., Bergmann, A., and Löser, T., "Ground-based simulation of complex maneuvers of a delta wing aircraft," *Journal of Aircraft*, Vol. 45, No. 1, 2008, pp. 286–291.

[18]Schütte, A., Einarsson, G., Raichle, A., Schöning, B., Mönnich, W., Neumann, J., Arnold, J., Alrutz, T., Heinecke, J., Forkert, T., and Schumann, H., "Prediction of the unsteady behavior of maneuvering aircraft by CFD aerodynamic, flight-mechanic and aeroelastic coupling," *NATO RTO/AVT Meeting Proceeding, RTO-AVT-MP-123*, 2005, pp. 11–1 – 11–20.

[19]Schütte, A., Einarsson, G., Raichle, A., Schöning, B., Orlt, M., Neumann, J., Arnold, J., Mönnich, W., and Forkert, T., "Numerical simulation of maneuvering aircraft by aerodynamic, flight mechanics and structural mechanics coupling," *Journal of Aircraft*, Vol. 46, No. 1, 2009, pp. 53–64.

[20]Schütte, A., Rein, M., and Höhler, G., "Experimental and numerical aspects of simulating unsteady flows around the X-31 configuration," *Proc. IMechE - J. Aerospace Engineering*, Vol. 223 Part G, 2009, pp. 309–321.

[21]Schütte, A., Cummings, R., and Loeser, T., "An integrated computational/experimental approach - X-31 stability & control estimation," *Aerospace Science and Technology*, Vol. 20, No. 1, 2011, pp. 2–11.

[22]Schütte, A., Boelens, O., Loeser, T., and Oehlke, M., "Prediction of the flow around the X-31 aircraft using two different CFD methods," *AIAA Paper 2010-4692*, June-July 2010.

[23]Boelens, O., "CFD analysis of the flow around the X-31 aircraft at high angle of attack," *AIAA Paper 2009-3628*, June 2009.

[24]Jirasek, A. and Cummings, R., "Application of Volterra functions – X-31 aircraft model motion," *AIAA Paper 2009-3629*, June 2009.

[25]Loeser, T., Vicroy, D., and Schütte, A., "SACCON static wind tunnel tests at DNW-NWB and 14x22 NASA LaRC," *AIAA Paper 2010-4393*, June-July 2010.

[26]Vicroy, D. and Loeser, T., "SACCON dynamic wind tunnel tests at DNW-NWB and 14x22 NASA LaRC," *AIAA Paper 2010-4394*, June-July 2010.

[27]Konrath, R., Roosenboom, E., Schröder, A., Pallek, D., and Otter, D., "Static and dynamic SACCON PIV tests - part II: Aft flow field," *AIAA Paper 2010-4396*, June-July 2010.

[28]Gilliot, A., "Static and dynamic SACCON PIV tests - Part I: Forward flowfield," *AIAA Paper 2010-4395*, June-July 2010.

[29]Frink, N., "Strategy for dynamic CFD simulations on SACCON configuration," *AIAA Paper 2010-4559*, June-July 2010.

[30]Vallespin, D., Ronch, A., Badcock, K., and Boelens, O., "SACCON CFD simulations using structured grid approaches," *AIAA Paper 2010-4560*, June-July 2010.

[31]Tormalm, M. and Schmidt, S., "Computational study of static and dynamic vortical flow over the delta wing SACCON configuration using the FOI flow solver Edge," *AIAA Paper 2010-4561*, June-July 2010.

[32]Le Roy, J. and Morgand, S., "SACCON CFD static and dynamic derivatives using elsA," *AIAA Paper 2010-4562*, June-July 2010.

[33]Cummings, R., Petterson, K., Jirasek, A., and Schmidt, S., "SACCON static and dynamic motion flow physics simulation using Cobalt," *AIAA Paper 2010-4691*, June-July 2010.

[34]Schütte, A., Hummel, D., and Hitzel, S., "Flow physics analyses of a generic unmanned combat aerial vehicle configuration," *Journal of Aircraft*, Vol. 49, No. 6, 2012, pp. 1638–1651.

[35]Huber, K., Schütte, A., and Rein, M., "Numerical investigation of the aerodynamic properties of a flying wing configuration," *AIAA Paper 2012-3325*, June 2012.

[36]Zimper, D. and Rein, M., "Experimental and numerical analysis of the transonic vortical flow over a generic lambda wing configuration," *AIAA Paper 2014-2005*, June 2014.

[37]Zimper, D. and Hummel, D., "Analysis of the transonic flow around a generic UCAV configuration," *AIAA Paper 2014-2266*, June 2014.

[38]Huber, K., Vicroy, D., Schütte, A., and Hübner, A.-R., "UCAV model design and static experimental investigations to estimate control device effectiveness and stability & control capabilities," *AIAA Paper 2014-2002*, June 2014.

[39]Vicroy, D., Huber, K., Loeser, T., and Rohlf, D., "Low-speed Dynamic Wind Tunnel Test Analysis of a Generic 53 Swept UCAV Configuration," *AIAA Paper 2014-2003*, June 2014.

[40]Rein, M., Irving, J., Rigby, G., and Birch, T., "High speed static experimental investigations to estimate control device effectiveness and stability & control capabilities," *AIAA Paper 2014-2004*, June 2014.

[41]Frink, N., "Stability and Control CFD Investigations of a Generic 53-deg Swept UCAV Configuration," *AIAA Paper 2014-2133*, June 2014.

[42]Hitzel, S. and Zimper, D., "Model Scale and "Real" Flight of Generic UCAV and Advanced Combat Aircraft - An Industrial Perspective," *AIAA Paper 2014-2267*, June 2014.

[43]Kennett, D., Hoholis, G., and Badcock, K., "Numerical Simulation of Control Surface Deflections over a Generic UCAV configuration at Off-design Flow Conditions," *AIAA Paper 2014-2134*, June 2014.

[44]Lofthouse, A., Ghoreyshi, M., JirasekA., and Cummings, R., "Static and Dynamic Simulations of a Generic UCAV Geometry Using the Kestrel Flow Solver," *AIAA Paper 2014-2264*, June 2014.

[45]Jirasek, A., Cummings, R., Schütte, A., and Huber, K., "The NATO STO AVT-201 Task Group on Extended assessment of Stability an Control Prediction Methods for NATO Air Vehicles: Summary, Conclusions and Lessons Learned," *AIAA Paper 2014-2394*, June 2014.

[46]Schütte, A., Huber, K., and Boelens, O., "Static and dynamic numerical simulations of a generic UCAV configuration with and without control devices." *AIAA Paper 2014-2132*, June 2014.

[47]Hövelmann, A. and Breitsamter, C., "Leading-Edge Geometry Effects on the Vortex Formation of a Diamond-Wing Configuration," *Journal of Aircraft, doi: 10.2514/1.C033014*, 2015.

[48]Boelens, O. and Luckring, J., "A Reduced-Complexity Investigation of Blunt Leading-Edge Separation Motivated by UCAV Aerodynamics," *AIAA Paper 2015-61*, Jan 2015.

[49]Boelens, O., Luckring, J., Breitsamter, C., Hövelmann, A., Knoth, F., Malloy, D., and Deck, S., "Numerical and Theoretical Considerations for the Design of the AVT-183 Diamond-Wing Experimental Investigations," *AIAA Paper 2015-62*, Jan 2015.

[50]Hövelmann, A. and Breitsamter, C., "Leading-Edge Roughness Effects on the Flow Separation Onset of the AVT-183 Diamond Wing Configuration ," *AIAA Paper 2015-63*, Jan 2015.

[51]Hövelmann, A., Grawunder, M., Buzica, A., and Breitsamter, C., "Experimental Analyses on the Flow Field Characteristics of the AVT-183 Diamond Wing Configuration," *AIAA Paper 2015-64*, Jan 2015.

[52]Hitzel, S., Boelens, O., and Hövelmann, A., "Vortex Development on the AVT-183 Diamond Wing Configuration - Numerical and Experimental Findings," *AIAA Paper 2015-89*, Jan 2015.

[53]Frink, N., "Numerical Analysis of Incipient Separation on 53-Deg Swept Diamond Wing," *AIAA Paper 2015-88*, Jan 2015.

[54]Galle, M., Gerhold, T., and Evans, J., "Technical Documentation of the DLR TAU-Code," *DLR-IB 233-97/A43*, 1997.

[55]Gerhold, T., Galle, M., Friedrich, O., and Evans, J., "Calculation of complex three-dimensional configurations employing the DLR TAU-Code," *AIAA Paper 1997-167*, Jan 1997.

[56]Gerhold, T., "Overview of the Hybrid RANS Code TAU," *NNFM*, Vol. 89, 2005, pp. 81–92.

[57]Schwamborn, D., Gerhold, T., and Heinrich, R., "The DLR TAU-Code: Recent applications in research and industry," *Proceedings of "European Conference on Computational Fluid Dynamics"ECCOMAS CDF, Delft, The Netherland*, 2006.

[58]Jameson, A., Baker, T., and Weatherill, N., "Calculation of inviscid transonic flow over a complete aircraft," *AIAA Paper 86-103*, Jan. 1986.

[59]Spalart, P. and Allmaras, S., "A one–equation turbulence model for aerodynamic–flows," *La Recherche Aérospatiale Journal, No. 1, pp. 5-21*, 1994.

[60]Allmaras, S., Johnson, F., and Spalart, P., "Modifications and clarifications for the implementation of the Spalart-Allmaras turbulence model," *ICCFD7 Proceedings, ICCFD7-1902*, 2012.

[61]Visonneau, M., Guilmineau, E., and Toxopeus, S., "Incompressible flow calculations of blunt leading edge separation for a 53 degree swept diamond wing," *AIAA Paper 2015-65*, Jan 2015.

[62]Kulfan, B. M., "Universal parametric geometry representation method," *Journal of Aircraft*, Vol. 45, No. 1, 2008, pp. 142–158.

[63]Kunze, P., Himisch, J., and Wunderlich, T., "Untersuchung von Parametrisierungsmethoden und Zielfunktionen zur Optimierung von Profilen eines transsonischen Tragflügels," *DLR Interner Bericht, IB 124-2009/7*, 2009.

[64]Jenkins, D., Landis, T., and Miller, J., "AMERICAN X-VEHICLES - Centennial of Flight Edition: An Inventory 2014 X-1 to X-50," *NASA SP-2003-4531, Monographs in Aerospace History, No. 31*, 2003.

[65]Louis, J., Marchetto, A., Maretsis, M., and Mijares, F., "nEUROn: An international cooperation to enhance innovation," *ICAS General Lecture*, 2014.

[66]Rauen, A., "Eurofighter Typhoon," *ICAS General Lecture*, 2008.

[67]Bertin, J. and Cummings, R., "Aerodynamics for Engineers," *Prentice Hall, New Jersey, 6 edition*, 2013.

[68]CentaurSoft, "http://www.centaursoft.com," *Webseite.*.

[69]Liersch, C. and Huber, K., "Conceptual control surface design and aerodynamic analyses of a generic UCAV configuration," *AIAA Paper 2014-2001*, June 2014.

[70]Polhamus, E., "Leading-edge-suction analogy of vortex lift to drag due to lift of sharp-edge delta wings," *NASA TN D-3767*, 1966.

[71]Schütte, A., Huber, K., and Boelens, O., "Static and dynamic numerical simulations of a generic UCAV configuration with and without control devices," *AIAA Paper 2014-2132*, June 2014.

[72]Schlichting, H. and Truckenbrodt, E., "Aerodynamik des Flugzeugs, Bd. 2," *Springer, Berlin*, 1969.

Curvature distribution	Leading edge radius r_N	Sweep angle φ	Mach number M_∞	Angle of attack α
Constant	0.001	53°	0.4	5 / 5.5 / 5.75 / 6 / 7 / 8 / 9 / 10
Constant	0.002	45°	0.4	10 / 11
	0.002	53°	0.4	6 / 7.5 / 8 / 8.25 / 8.5 / 9 / 10 / 11
	0.002	60°	0.4	10 / 11
	0.002	65°	0.4	10 / 11
Constant	0.003	45°	0.3	11 / 12
	0.003	45°	0.4	10 / 11
	0.003	45°	0.5	11
	0.003	45°	0.6	11
	0.003	53°	0.3	11 / 12 / 13
	0.003	53°	0.4	8 / 9 / 9.5 / 9.6 / 9.75 / 10 / 11 / 12
	0.003	53°	0.5	11 / 12
	0.003	53°	0.6	11 / 12
	0.003	60°	0.3	11 / 12
	0.003	60°	0.4	10 / 11 / 12
	0.003	60°	0.5	10 / 11
	0.003	60°	0.6	10 / 11
	0.003	65°	0.3	11 / 12
	0.003	65°	0.4	10 / 11 / 12
	0.003	65°	0.5	11 / 12
	0.003	65°	0.6	11 / 12
Constant	0.004	45°	0.4	10 / 11
	0.004	53°	0.4	8 / 9.5 / 10 / 10.5 / 10.75 / 11 / 12 / 13
	0.004	60°	0.4	10 / 11 / 12
	0.004	65°	0.4	10 / 11 / 12
Constant	0.005	53°	0.4	9 / 10 / 10.5 / 11 / 11.5 / 11.75 / 12 / 13/ 14
Increasing	0.001–0.003	53°	0.4	6 / 7 / 7.25 / 7.5 / 7.75 / 8 / 9 / 10
Decreasing	0.003–0.001	53°	0.4	6 / 6.5 / 7 / 8 / 9 / 10

Table 1. Configurations and test matrix.

intial wall distance y_W	$8 \cdot 10^{-6} \cdot c_{ref}$
number of prism layers	35
area of refinement at the leading edge	$0\,to\,3 \cdot 10^{-3} \cdot c_{ref}$
cell size around wing nose	$2 \cdot 10^{-4} \cdot c_{ref}$
cell size on the surface	$1 \cdot 10^{-2} \cdot c_{ref}$
dimension of the field source over the wing	
hight	$0.3 \cdot c_{ref}$
width	$1.1 \cdot s$
depth	$1.6 \cdot c_{ref}$
cell size within the source	$1 \cdot 10^{-2} \cdot c_{ref}$

Table 2. Grid generation parameters

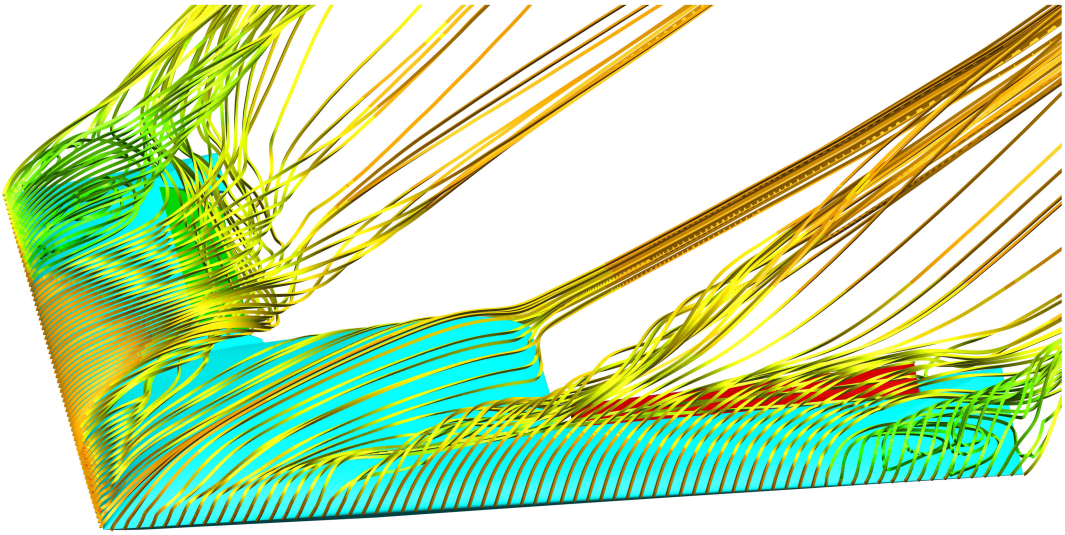

Figure 1. RANS calculation of the complex vortex topology around a generic military configuration with high sweep angle and round leading edges. [71]

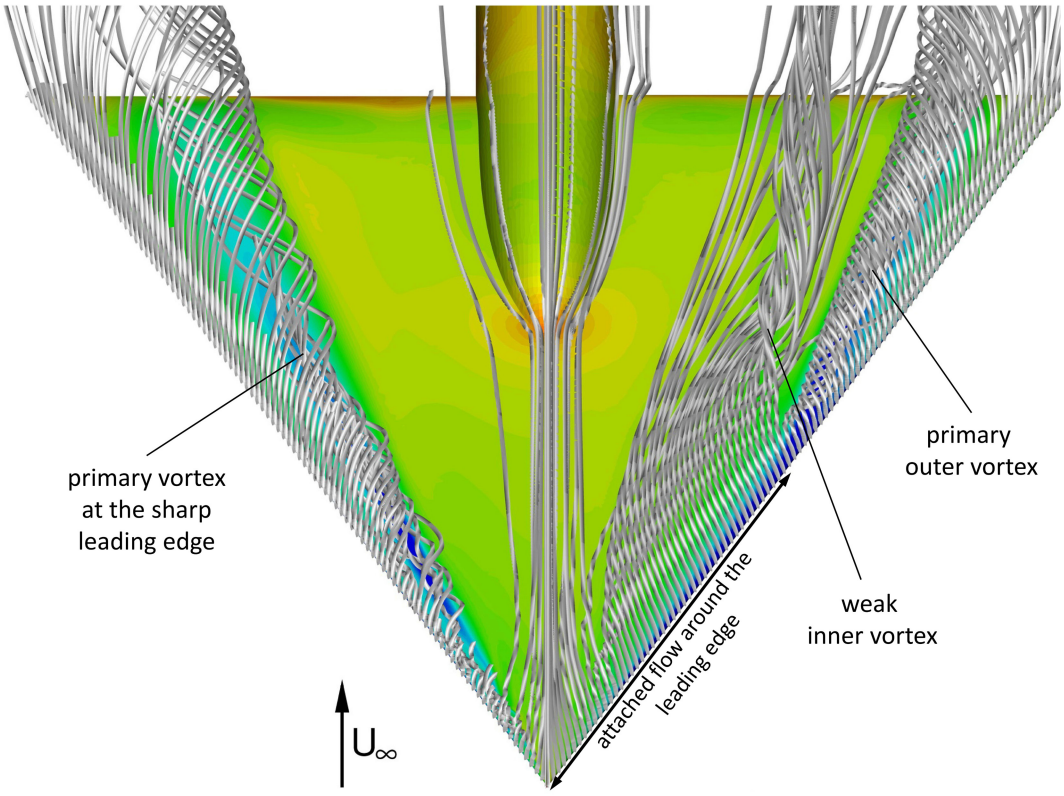

Figure 2. RANS calculation of the complex vortex topology around a delta wing with sharp (left) and round (right) leading edges. Plotted are the field streamlines starting from the leading edge close to the wing nose in the z=0 plane.

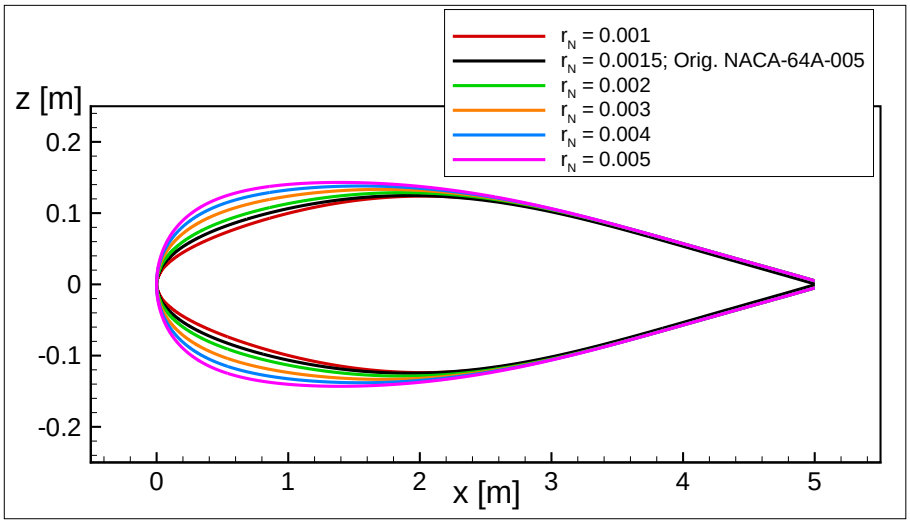

Figure 3. NACA-64A-005 airfoil and applied airfoil geometries with different leading edge contour curvatures.

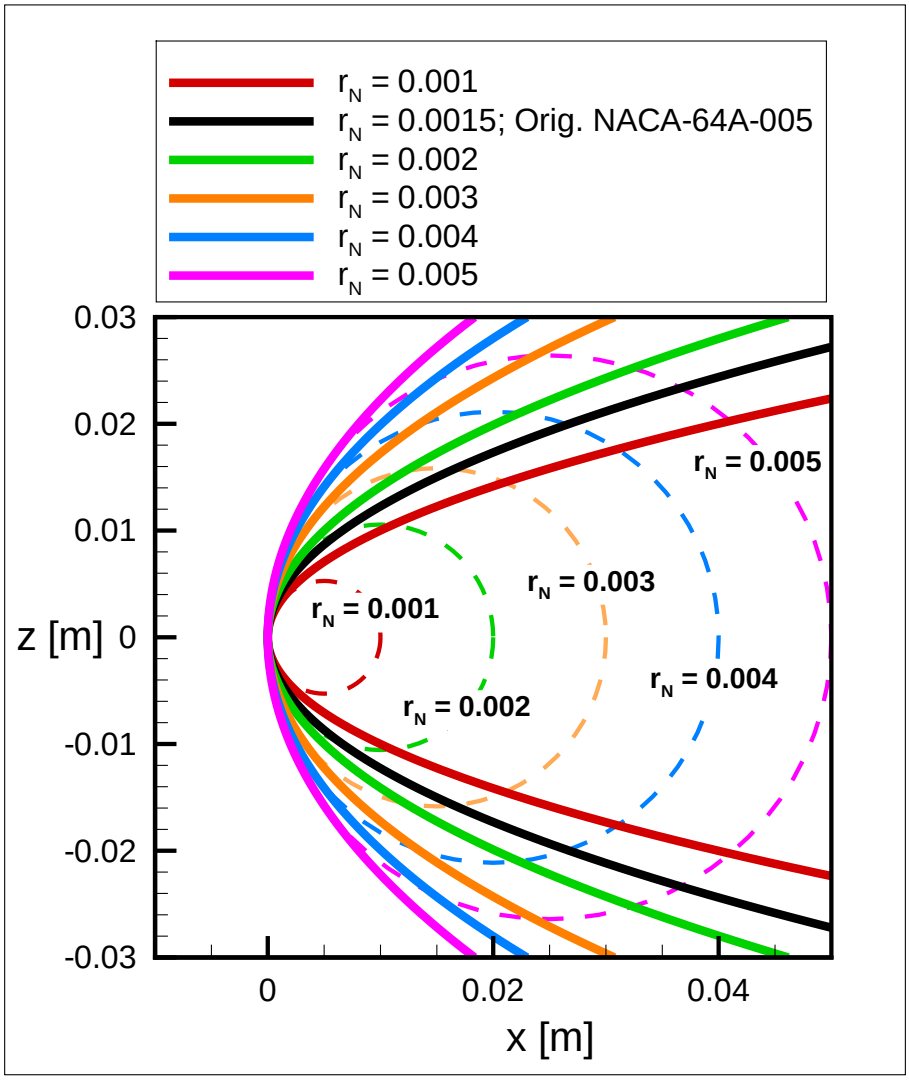

Figure 4. Comparison of the leading edge contour curvatures of the applied airfoils with c_{ref}=5m.

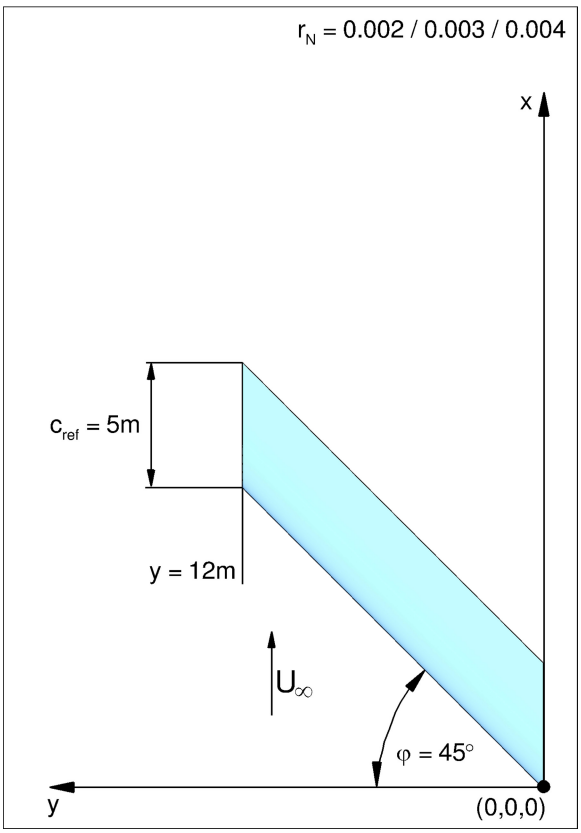

Figure 5. Plan form of the wing configuration with constant leading edge curvature radius r_N and sweep angle of $\varphi = 45°$.

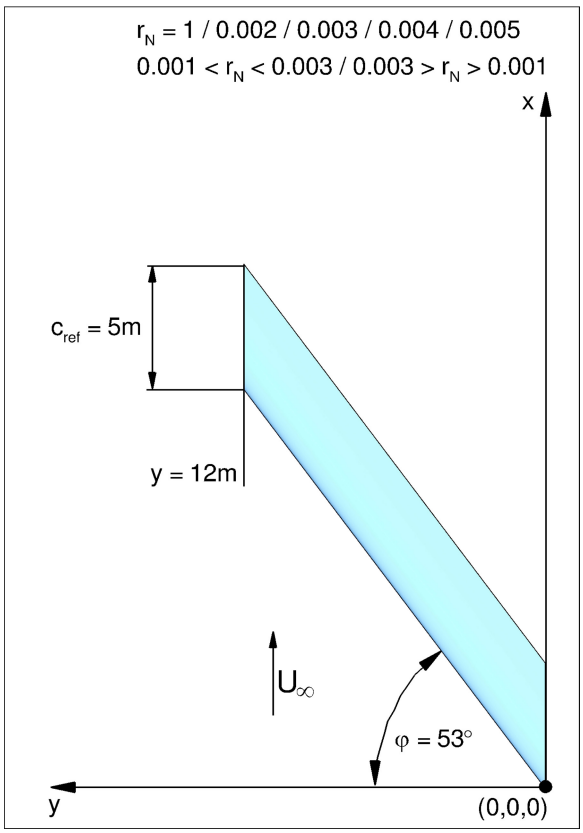

Figure 6. Plan form of the wing configuration with constant and variable leading edge curvature radius r_N and sweep angle of $\varphi = 53°$.

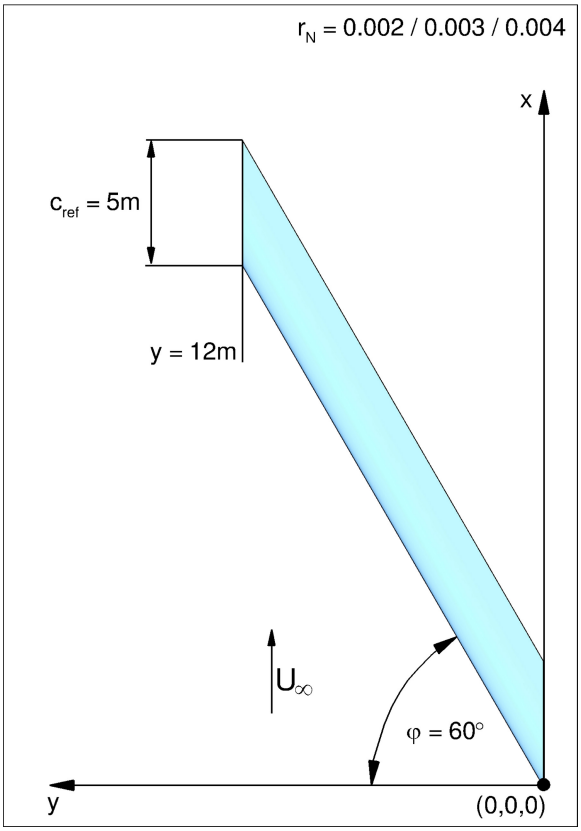

Figure 7. Plan form of the wing configuration with constant leading edge curvature radius r_N and sweep angle of $\varphi = 60°$.

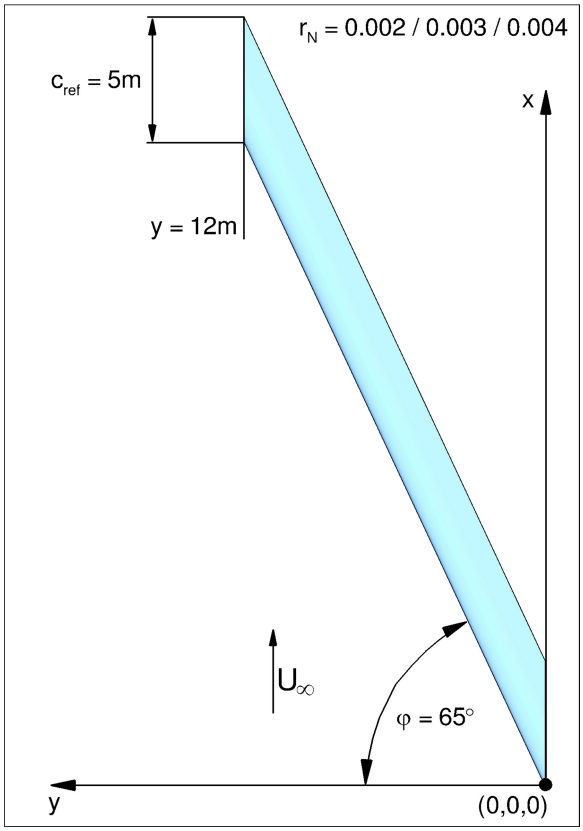

Figure 8. Plan form of the wing configuration with constant leading edge curvature radius r_N and sweep angle of $\varphi = 65°$.

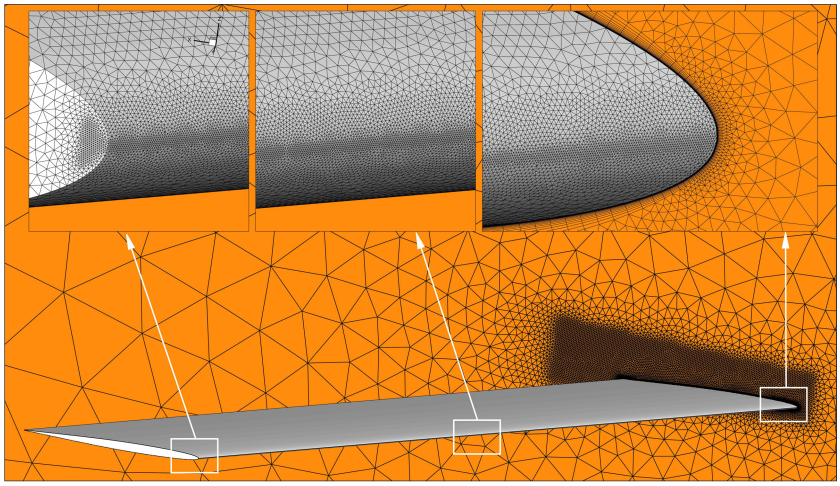

Figure 9. Grid topology: Triangulation of the leading edge and symmetry plane.

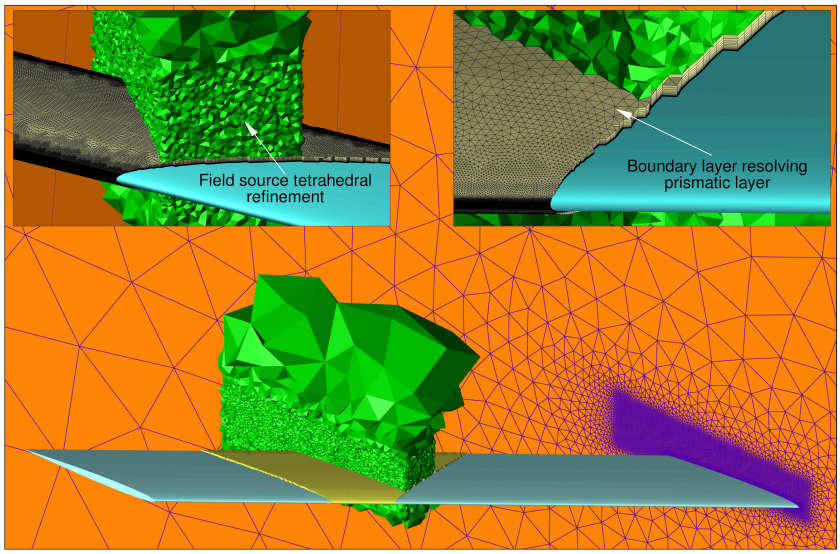

Figure 10. Grid topology: Dicitization of the prismatic layer to resolve the boundary layer flow abs well as the refinement of the tetrhedrals in the outer flow field to resolve the vortical flow around the wing.

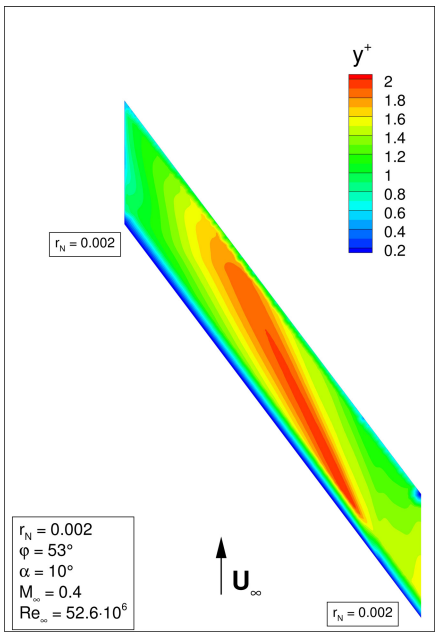

Figure 11. y+ distribution: $r_N = 0.002$; $\varphi = 53°$, $\alpha = 10°$. $M_\infty = 0.4$, $Re_\infty = 52.6 \cdot 10^6$.

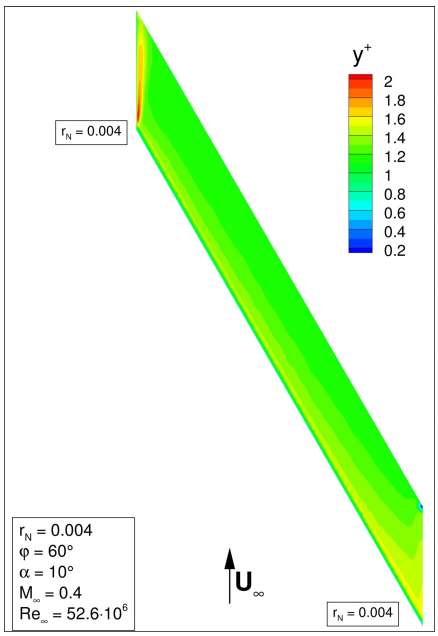

Figure 12. y+ distribution: $r_N = 0.004$, $\varphi = 60°$, $\alpha = 10°$. $M_\infty = 0.4$, $Re_\infty = 52.6 \cdot 10^6$.

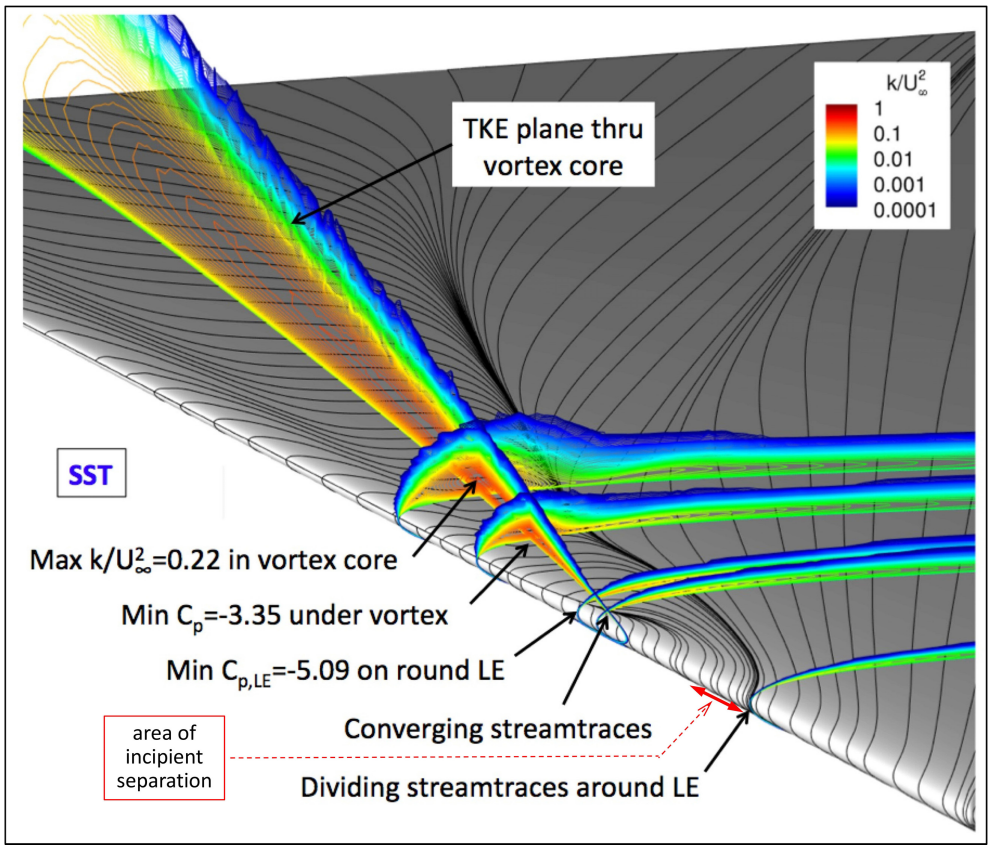

Figure 13. Flow physics of the AVT-183 53° delta wing. Surface streamlines and the turbulent kinetic energy k/U_∞^2 at slices through the flow field. CFD method USM3D, Menter-SST turbulence model, $\alpha = 12°$, $M_\infty = 0.15$, $Re_{\infty\, c_{ref}} = 2.7 \cdot 10^6$.[41]

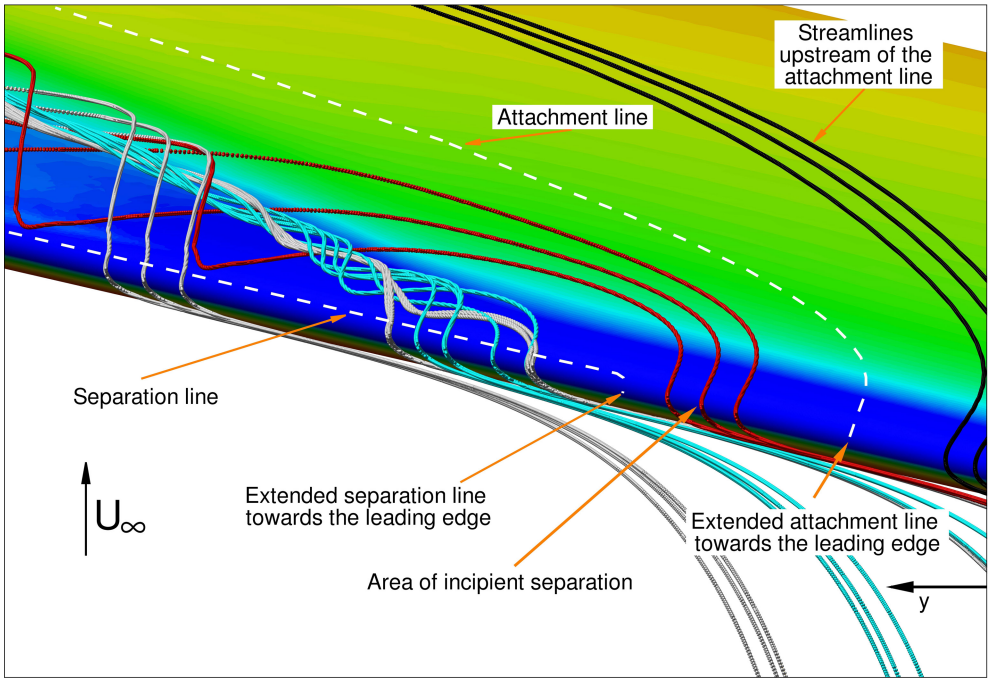

Figure 14. Detailed view on the flow physics of the separation at the round leading edge: Location of the separation and attachment line as well as streamlines of the outer flow field. $r_N = 0.004$, $\varphi = 53°$, $\alpha = 11°$. $M_\infty = 0.4$, $Re_\infty = 52.6 \cdot 10^6$.

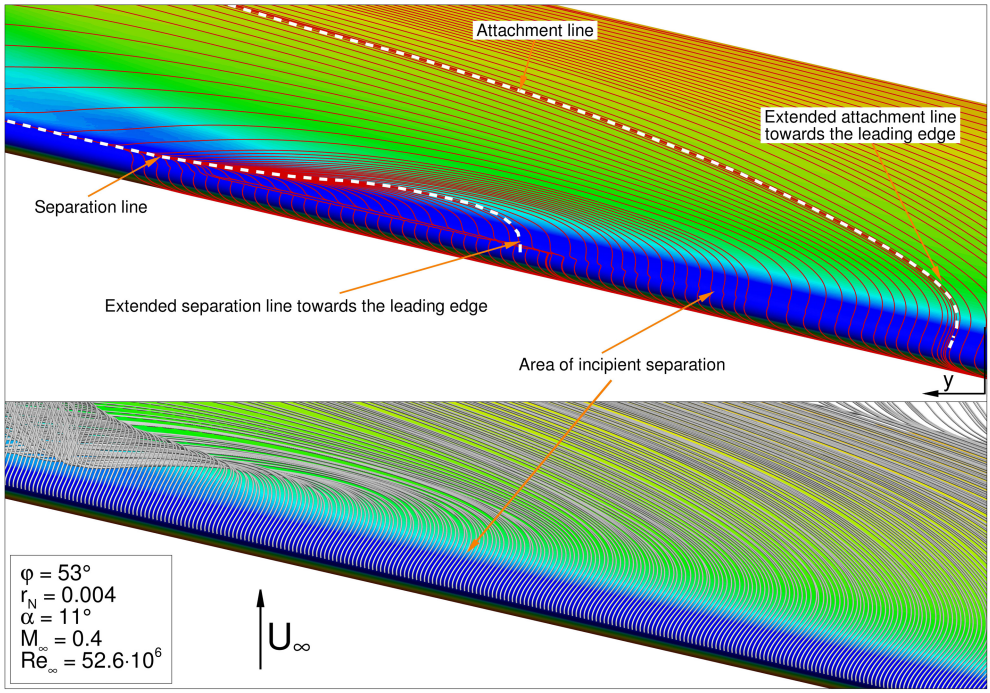

Figure 15. Detailed view on the flow physics of the separation at the round leading edge: Location of the separation and attachment line as well as streamlines of the outer flow field. $r_N = 0.004$, $\varphi = 53°$, $\alpha = 11°$. $M_\infty = 0.4$, $Re_\infty = 52.6 \cdot 10^6$.

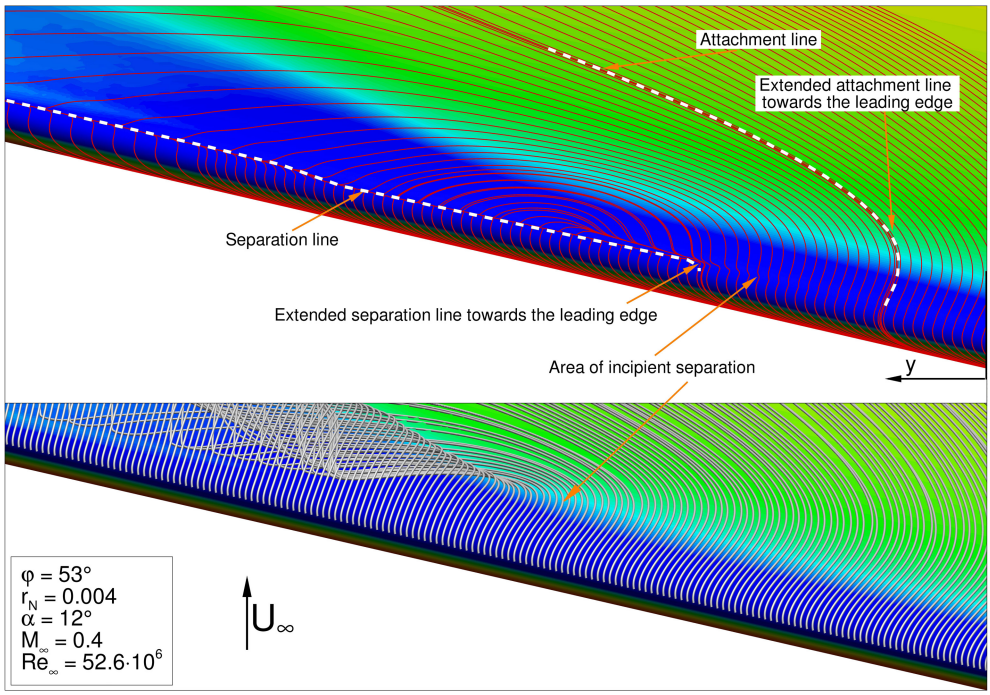

Figure 16. Detailed view on the flow physics of the separation at the round leading edge: Location of the separation and attachment line as well as streamlines of the outer flow field. $r_N = 0.004$, $\varphi = 53°$, $\alpha = 12°$. $M_\infty = 0.4$, $Re_\infty = 52.6 \cdot 10^6$.

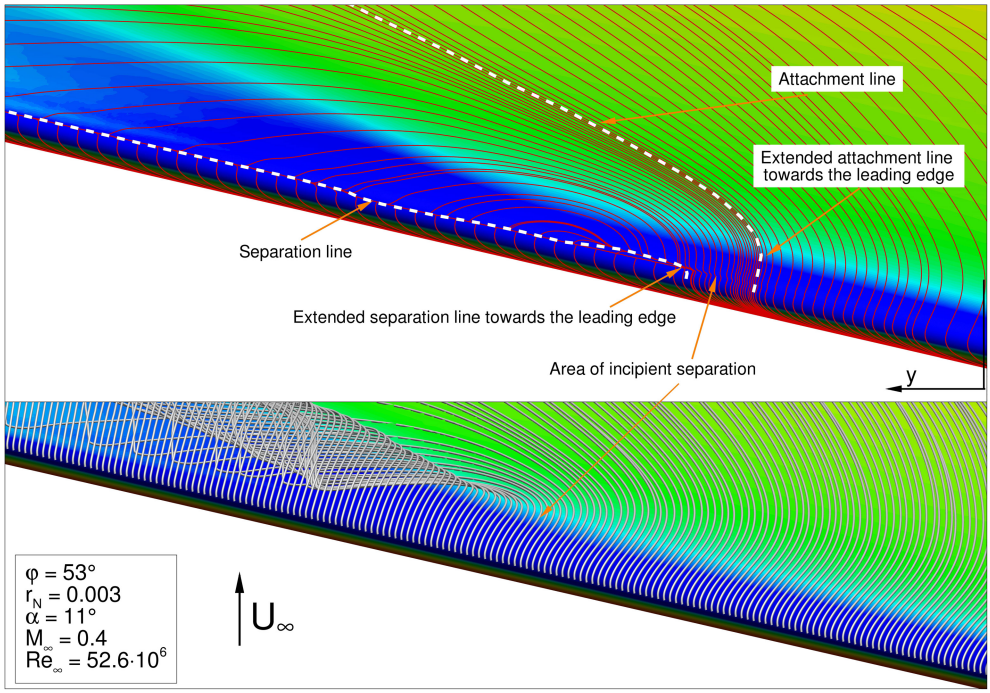

Figure 17. Detailed view on the flow physics of the separation at the round leading edge: Location of the separation and attachment line as well as streamlines of the outer flow field. $r_N = 0.003$, $\varphi = 53°$, $\alpha = 11°$. $M_\infty = 0.4$, $Re_\infty = 52.6 \cdot 10^6$.

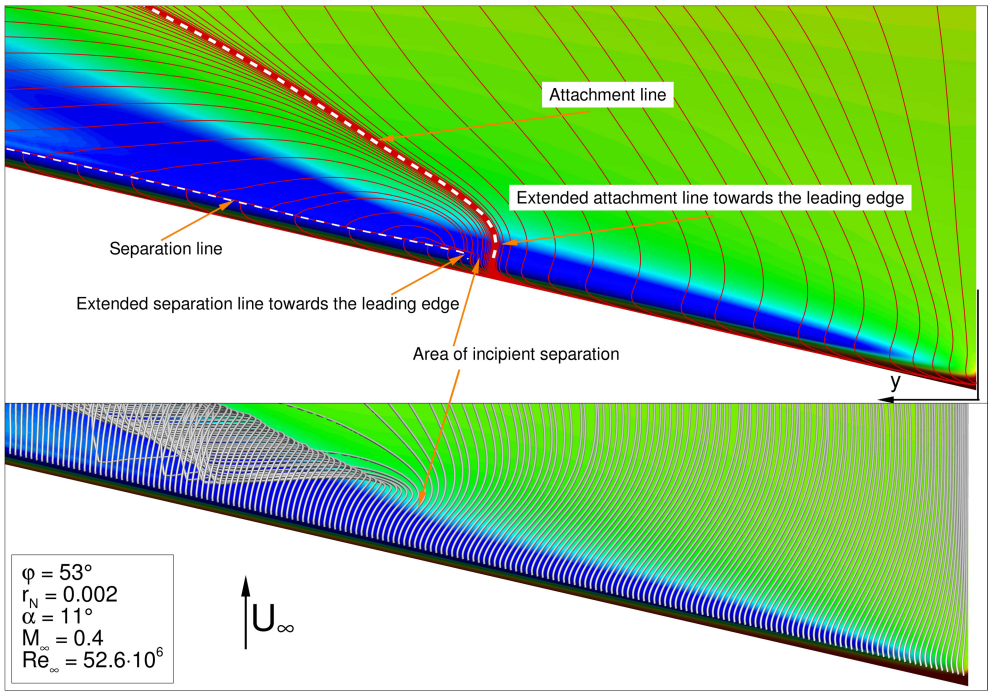

Figure 18. Detailed view on the flow physics of the separation at the round leading edge: Location of the separation and attachment line as well as streamlines of the outer flow field. $r_N = 0.002$; $\varphi = 53°$, $\alpha = 11°$. $M_\infty = 0.4$, $Re_\infty = 52.6 \cdot 10^6$.

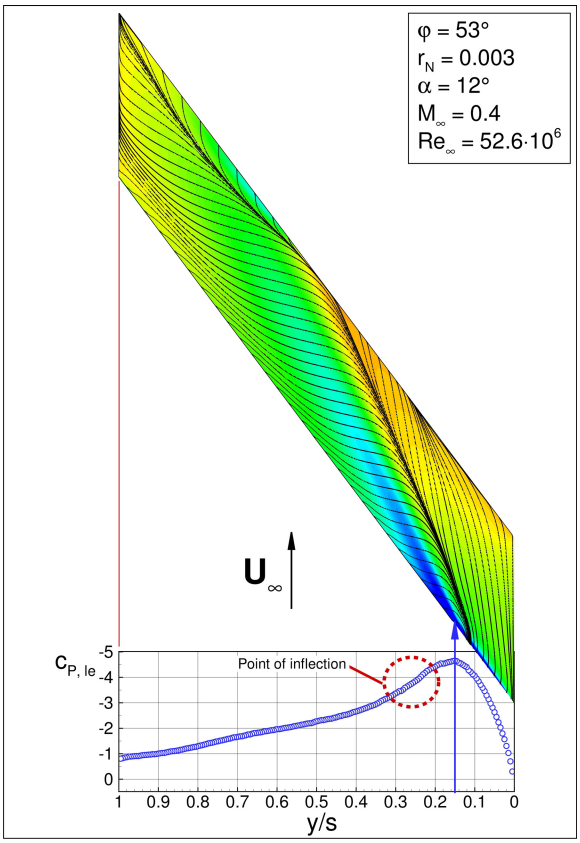

Figure 19. Surface streamlines and c_P distribution on the upper side of the wing and at the leading edge to determine the vortex onset location. $r_N = 0.003$, $\varphi = 53°$, $\alpha = 12°$. $M_\infty = 0.4$, $Re_\infty = 52.6 \cdot 10^6$. ($c_P$ legend as reference for all following presented results)

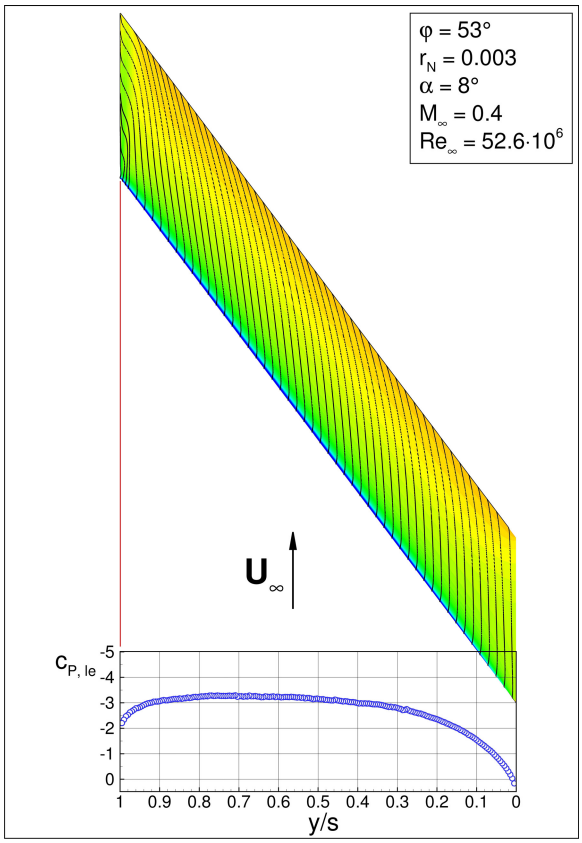

Figure 20. Surface streamlines and c_P distribution on the upper side of the wing and at the leading edge to determine the vortex onset location. $r_N = 0.003$, $\varphi = 53°$, $\alpha = 8°$. $M_\infty = 0.4$, $Re_\infty = 52.6 \cdot 10^6$. ($c_P$ legend as reference for all following presented results)

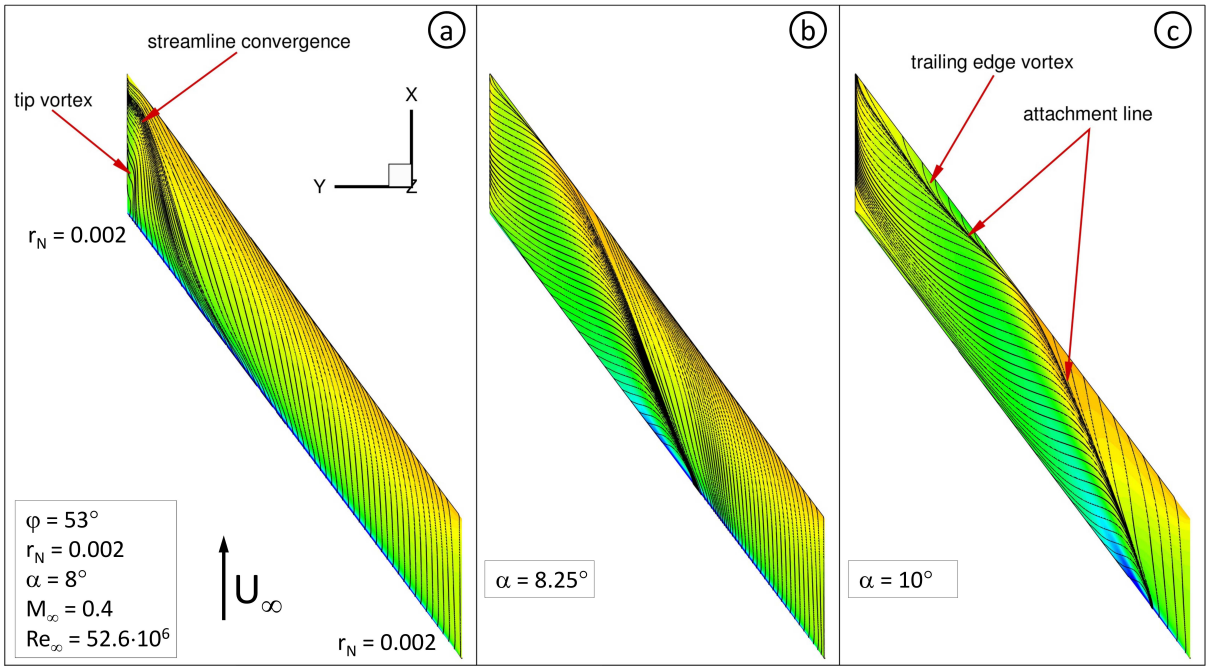

Figure 21. r_N const.: c_P distribution and surface streamlines on the upper side of the wing: $r_N =$ 0.002, $\varphi = 53°$, $\alpha = 8°$, 8.25° and 10°, $M_\infty = 0.4$, $Re_\infty = 52.6 \cdot 10^6$.

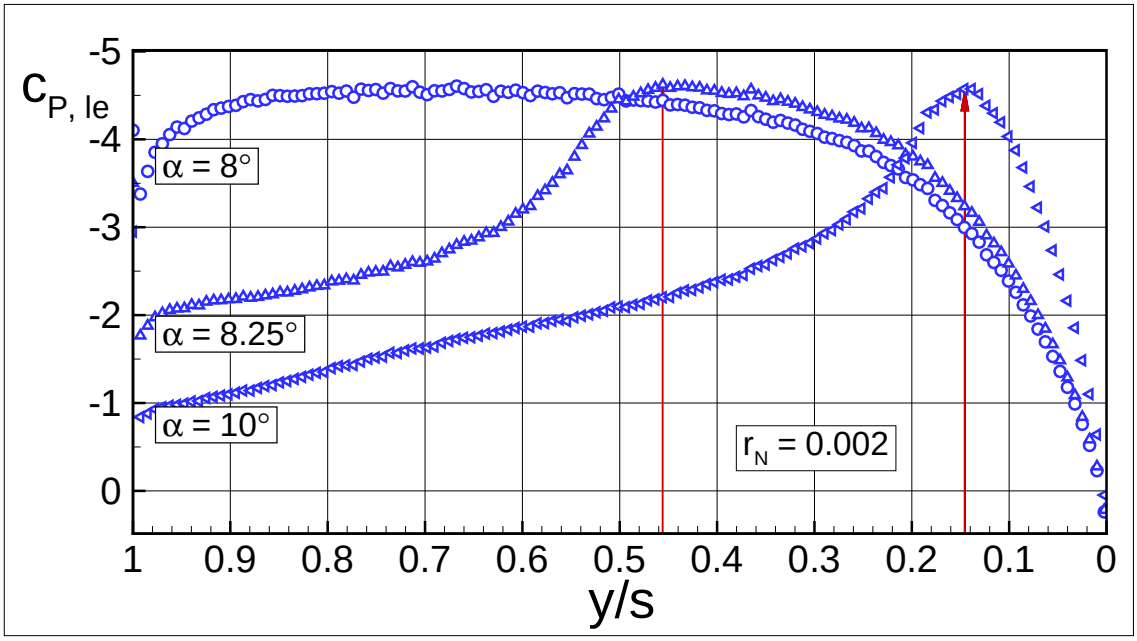

Figure 22. r_N **const.:** c_P **distribution at the leading edge:** $r_N = 0.002$, $\varphi = 53°$, $\alpha = 8°$, **8.25° and 10°,** $M_\infty = 0{,}4$; $Re_\infty = 52.6 \cdot 10^6$.

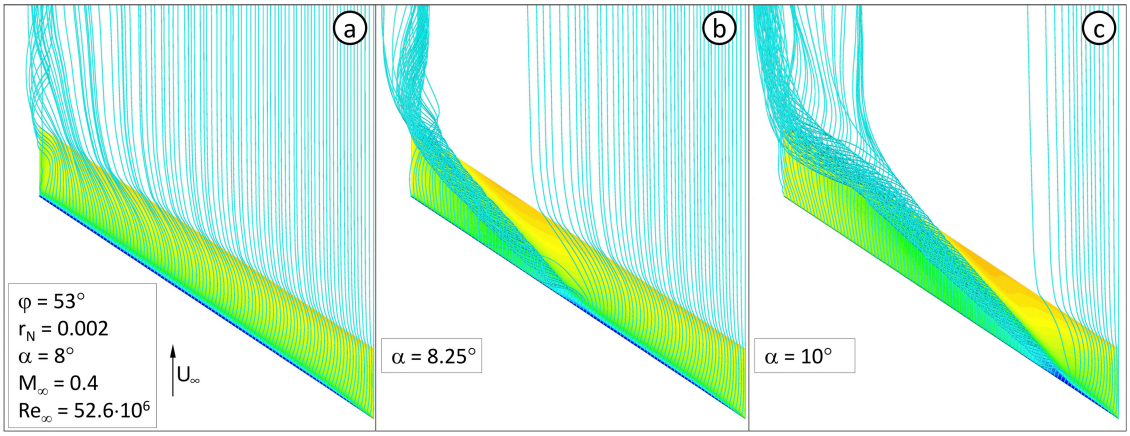

Figure 23. r_N **const.: Streamline in the flow field upon the upper side of the wing:** $r_N = 0.002$, $\varphi = 53°$, $\alpha = 8°$, **8.25° and 10°,** $M_\infty = 0{,}4$; $Re_\infty = 52.6 \cdot 10^6$.

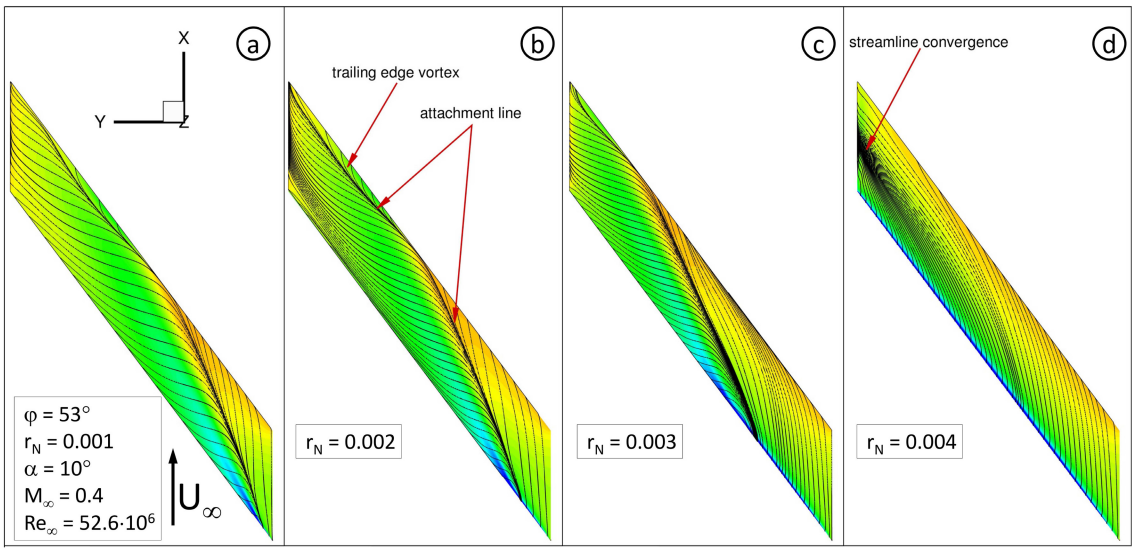

Figure 24. r_N **const.:** c_P **distribution and surface streamlines on the upper side of the wing:** $r_N =$ **0.001, 0.002, 0.003 and 0.004,** $\varphi = 53°$, $\alpha = 10°$, $M_\infty = 0.4$, $Re_\infty = 52.6 \cdot 10^6$.

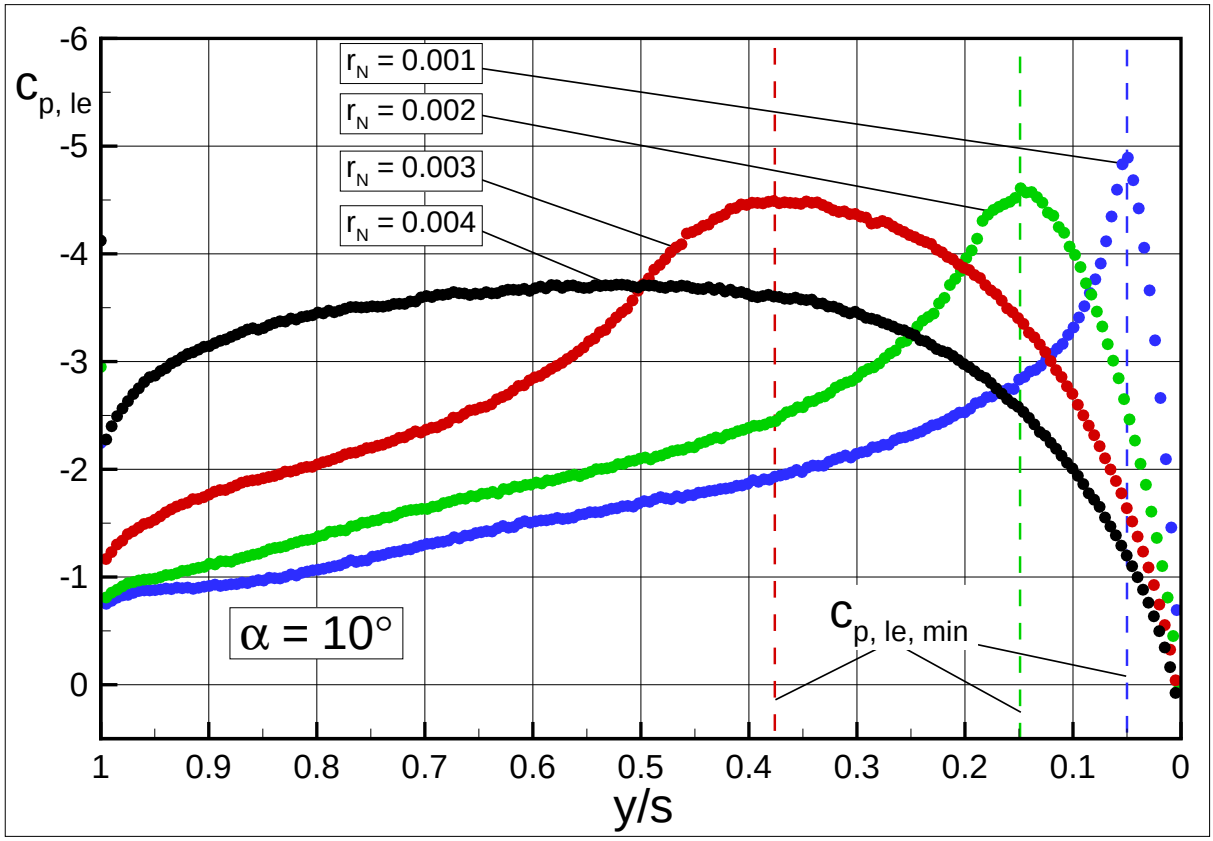

Figure 25. r_N const.: c_P distribution at the leading edge and determination of the vortex onset location. r_N = 0.001-0.004, φ = 53°, α = 10°. M_∞ = 0.4, Re_∞ = 52.6·10^6.

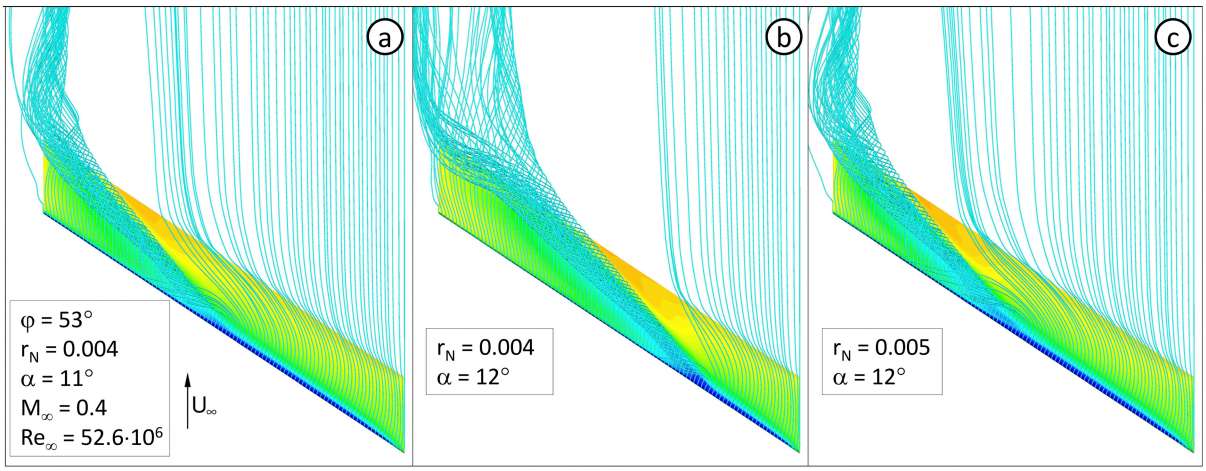

Figure 26. r_N const.: Streamline in the flow field upon the upper side of the wing: r_N = 0.004 and 0.005, φ = 53°, α = 11° and 12°, M_∞ = 0,4; Re_∞ = 52.6·10^6.

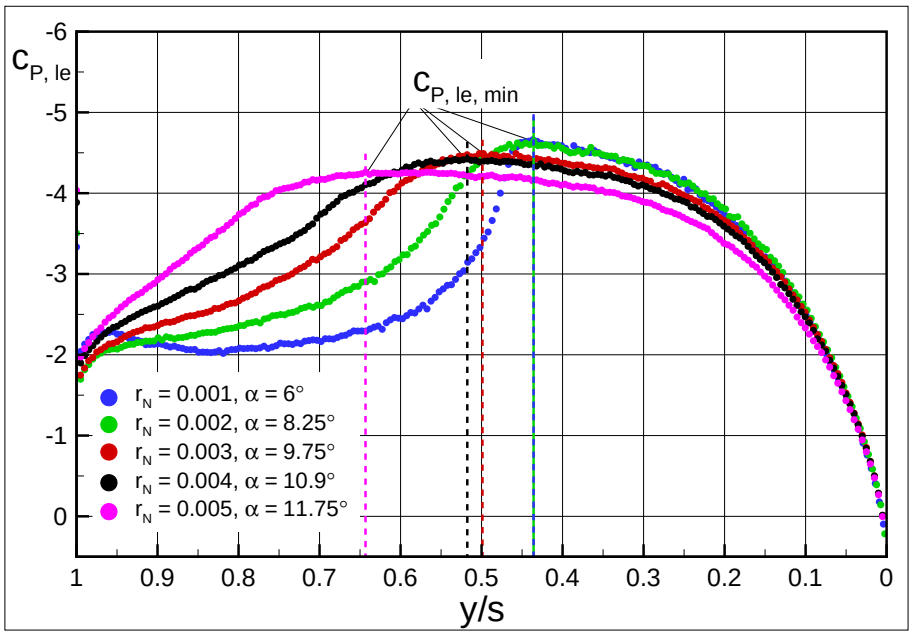

Figure 27. r_N const.: c_P distribution at the leading edge and determination of the vortex onset location for r_N = 0,001-0,005, φ = 53°. M_∞ = 0.4, $Re_\infty = 52.6 \cdot 10^6$.

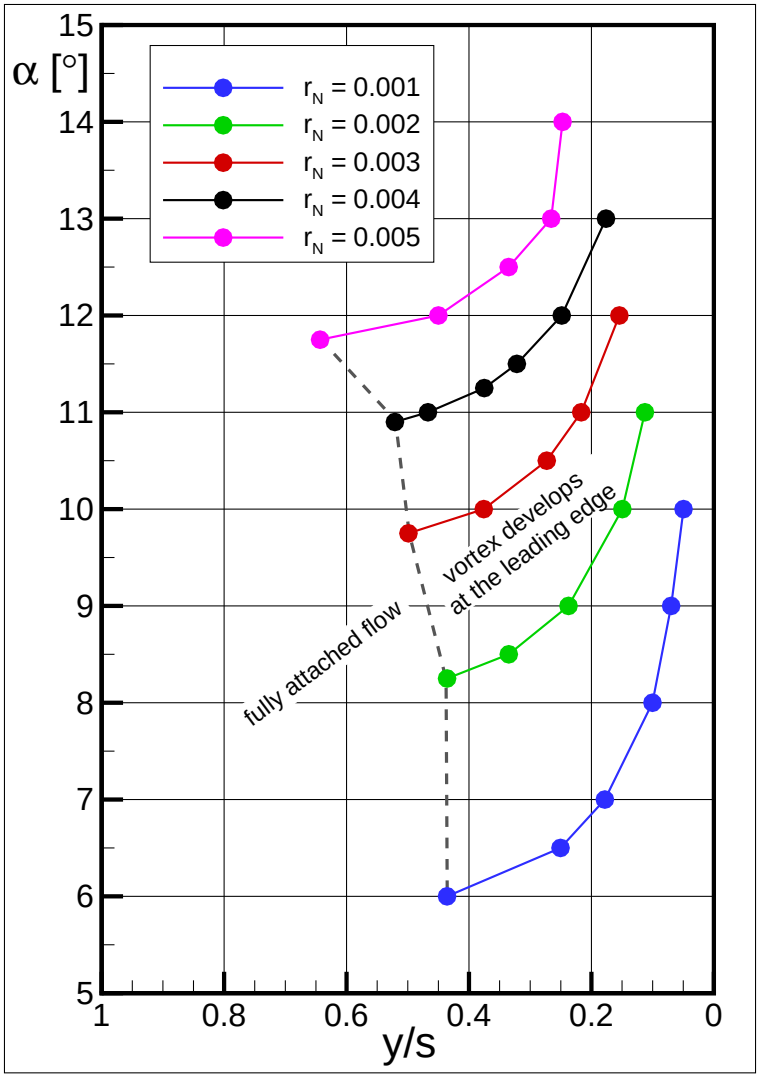

Figure 28. Overview of the vortex onset location versus the AoA α for different leading edge radius contours r_N.

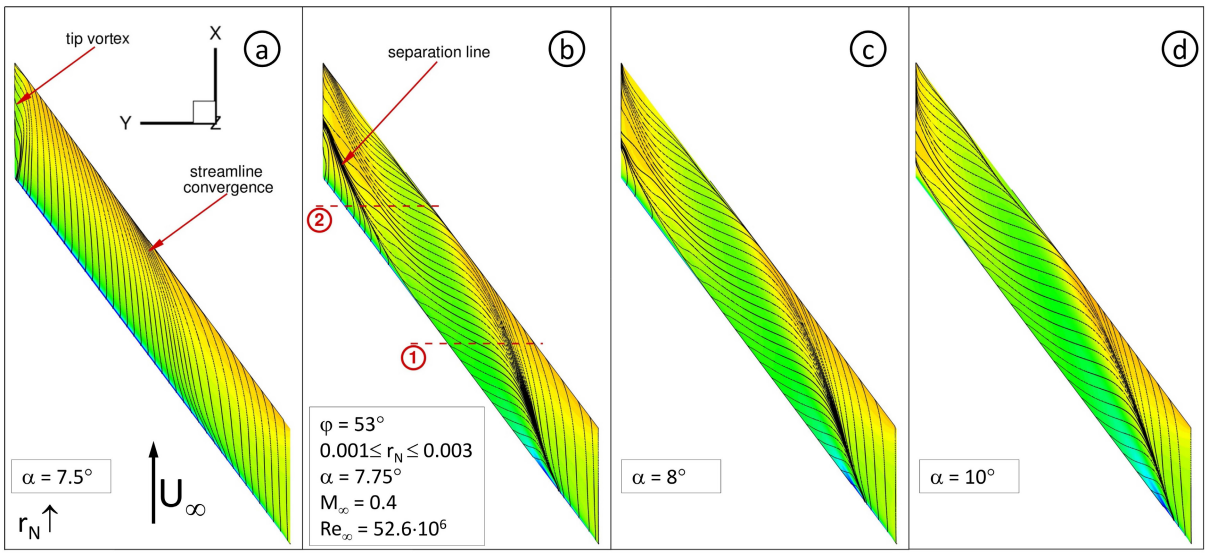

Figure 29. r_N increasing: c_P distribution and surface streamlines on the upper side of the wing: $0.001 \leq r_N \leq 0.003$, $\varphi = 53°$, $\alpha = 7.5°$, 7.75°, 8° and 10°, $M_\infty = 0.4$; $Re_\infty = 52.6 \cdot 10^6$.

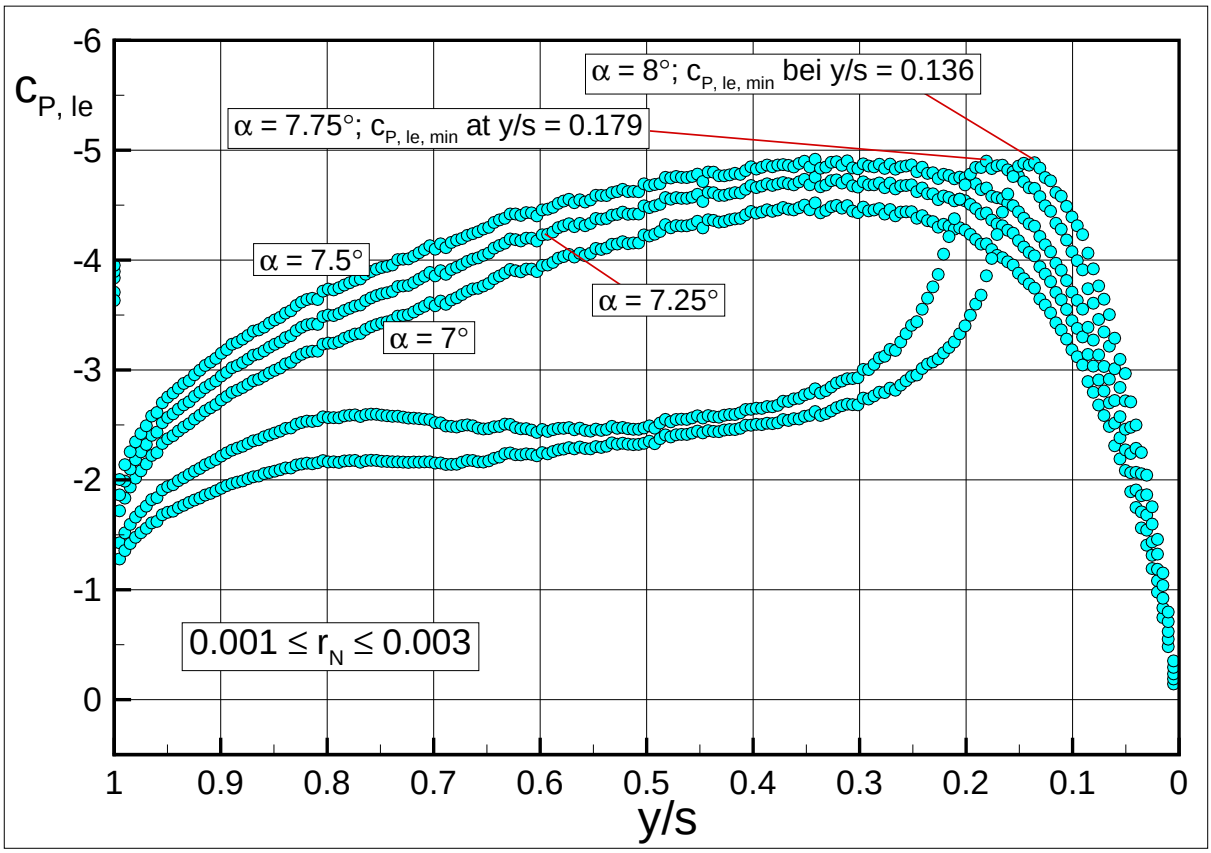

Figure 30. r_N increasing: c_P distribution at the leading edge and determination of the vortex onset location. $0.001 \leq r_N \leq 0.003$, $\varphi = 53°$. $M_\infty = 0.4$, $Re_\infty = 52.6 \cdot 10^6$.

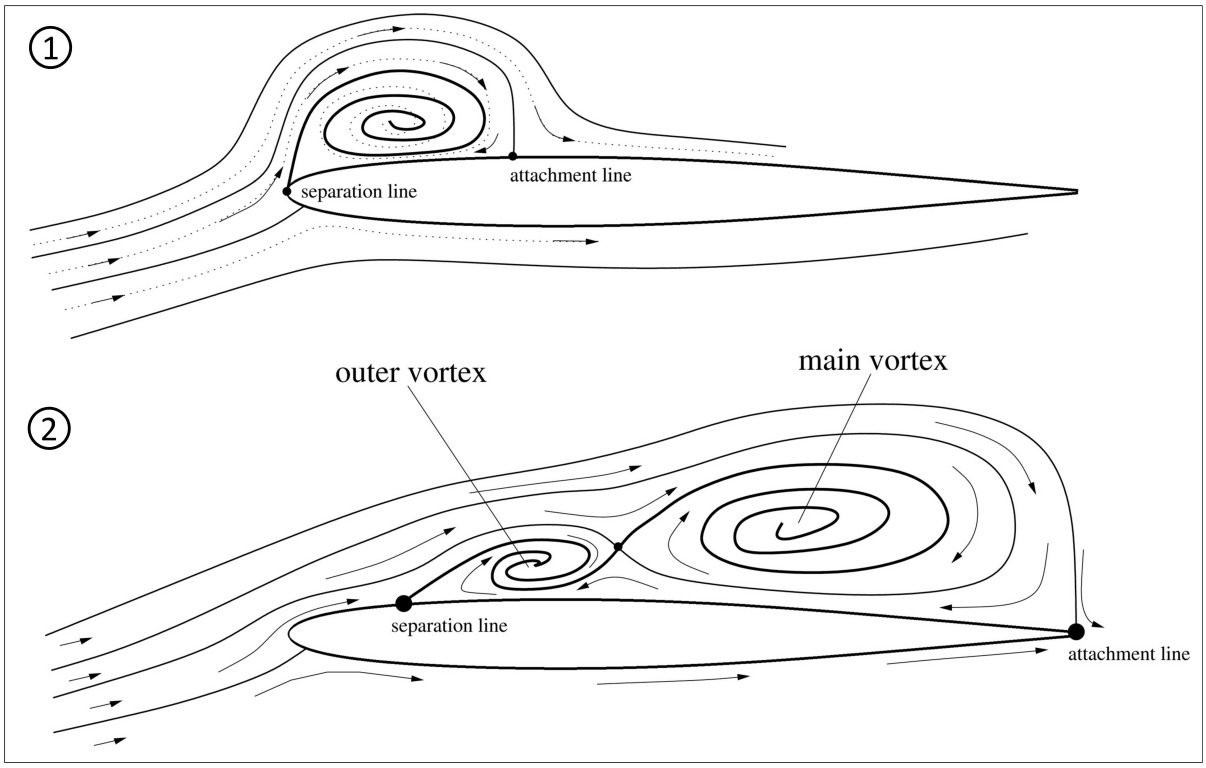

Figure 31. r_N increasing: Vortex topology at the round leading edge. Position (1) and (2) in Fig. 24b.

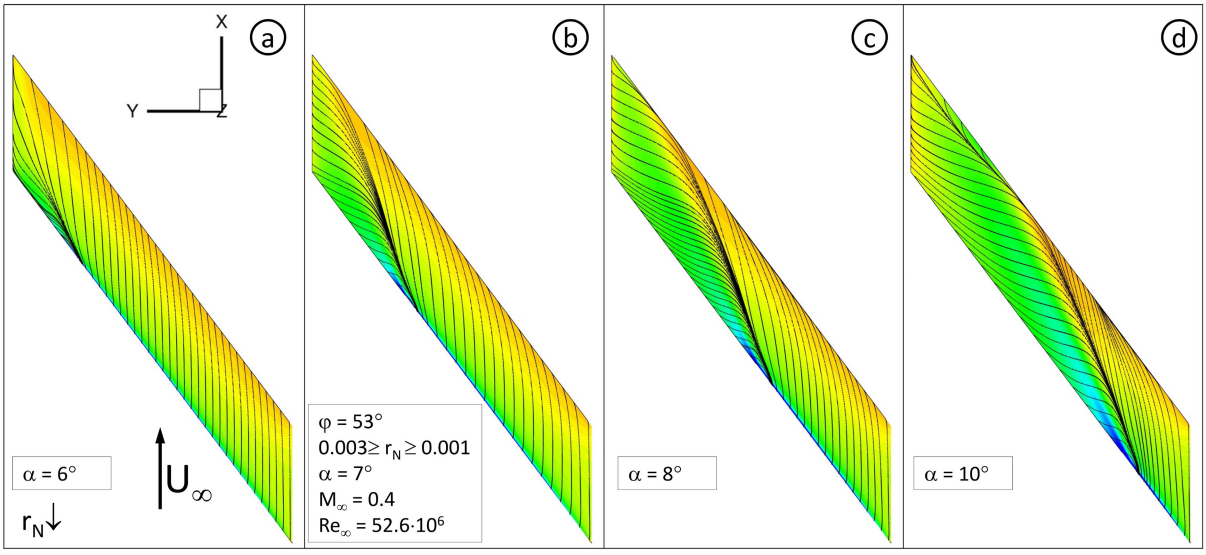

Figure 32. r_N decreasing: c_P distribution and surface streamlines on the upper side of the wing: $0.003 \geq r_N \geq 0.001$, $\varphi = 53°$, $\alpha = 6°$, 7°, 8° and 10°, $M_\infty = 0.4$; $Re_\infty = 52.6 \cdot 10^6$.

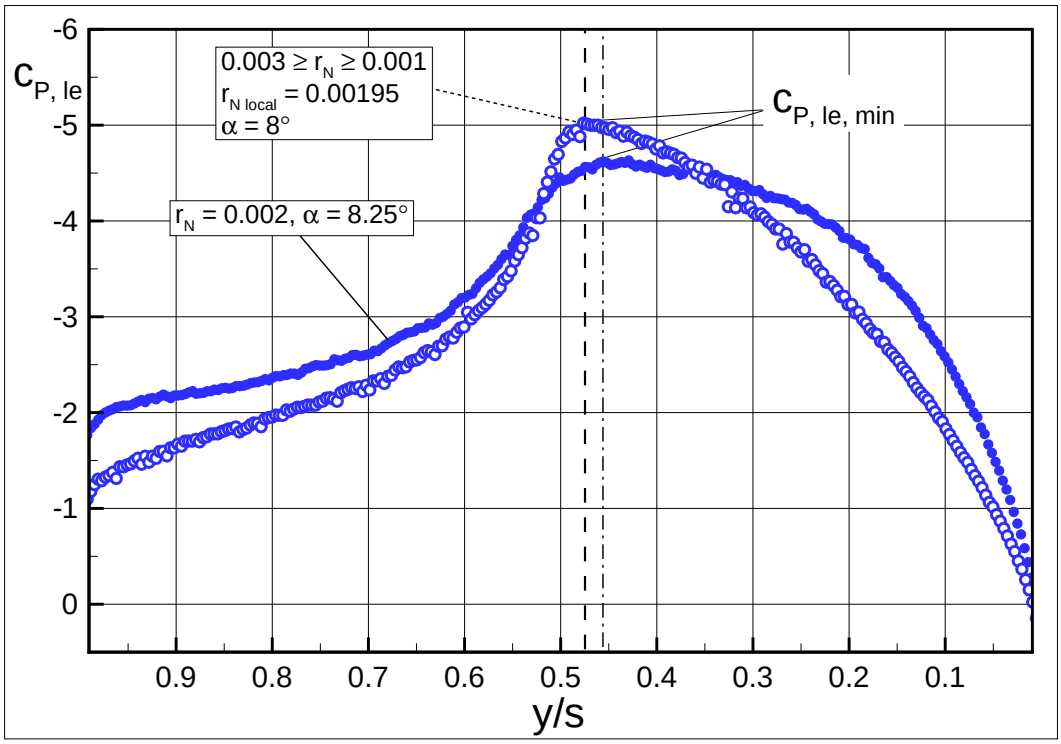

Figure 33. r_N decreasing: c_P distribution at the leading edge and determination of the vortex onset location. Comparison of a decreasing r_N ($\alpha = 8°$) and constant r_N with $r_N = 0.002$ ($\alpha = 8.25°$), $\varphi = 53°$, $M_\infty = 0.4$, $Re_\infty = 52.6 \cdot 10^6$.

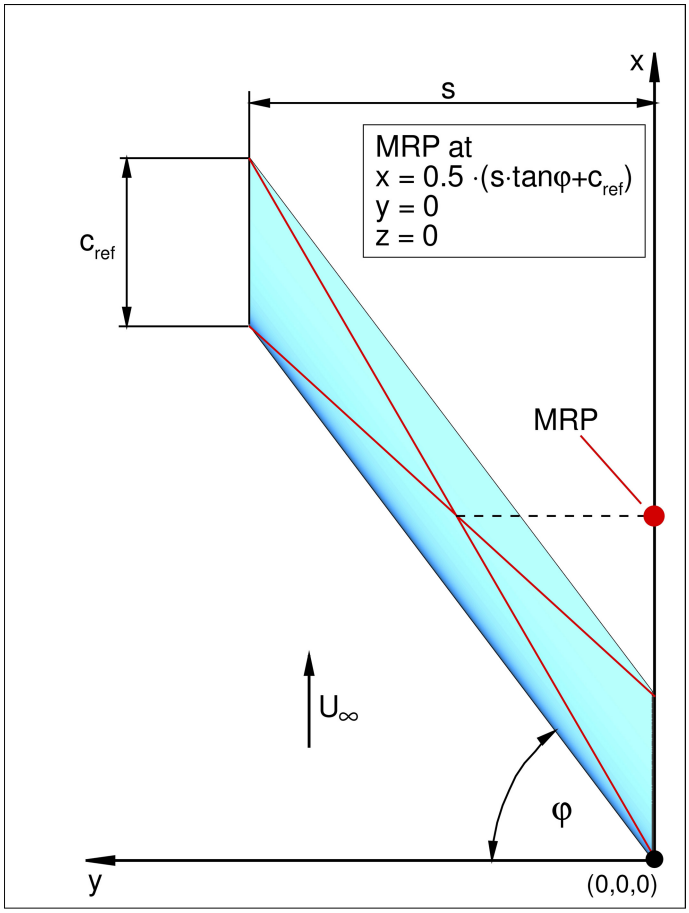

Figure 34. Location and determination of the Moment Reference Point (MRP) to assess the pitching moment.

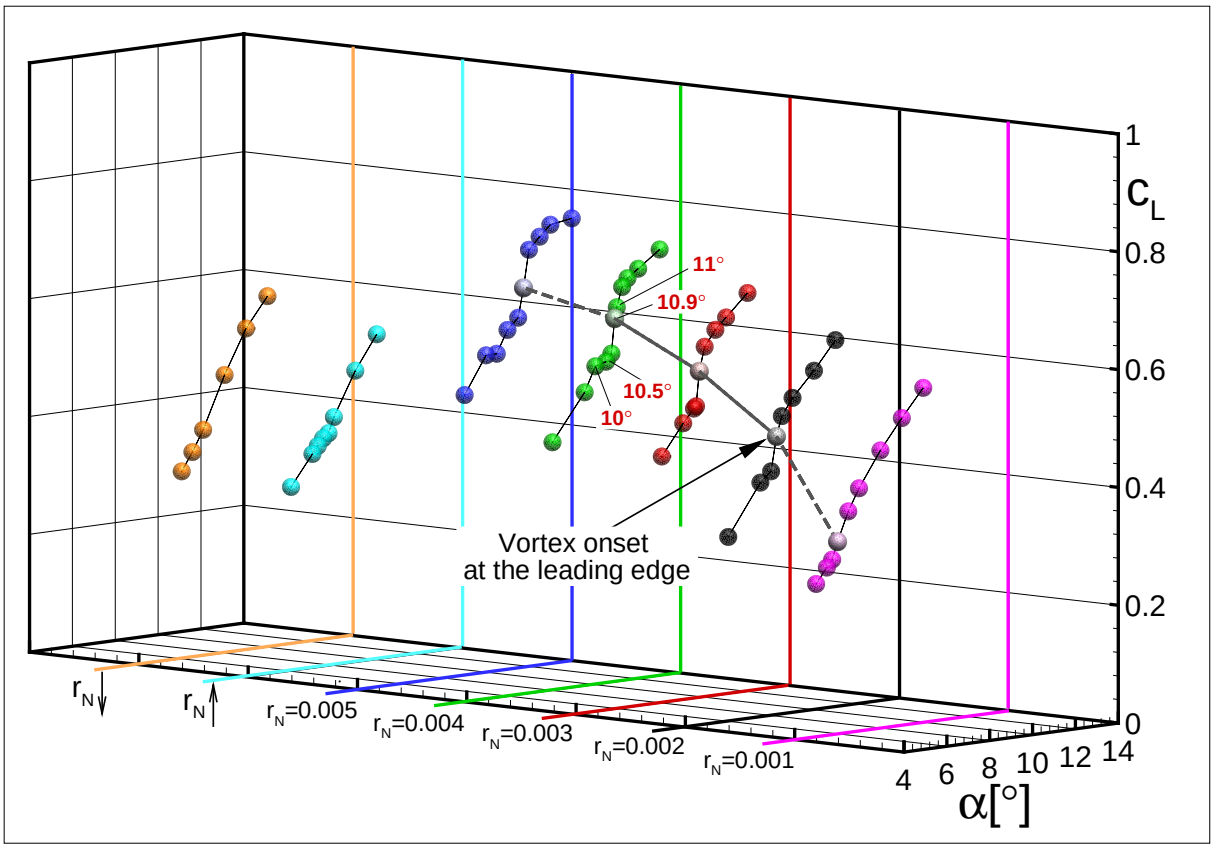

Figure 35. Lift coeffcient c_A versus AoA α for the configuration with $\varphi = 53°$ and variable r_N.

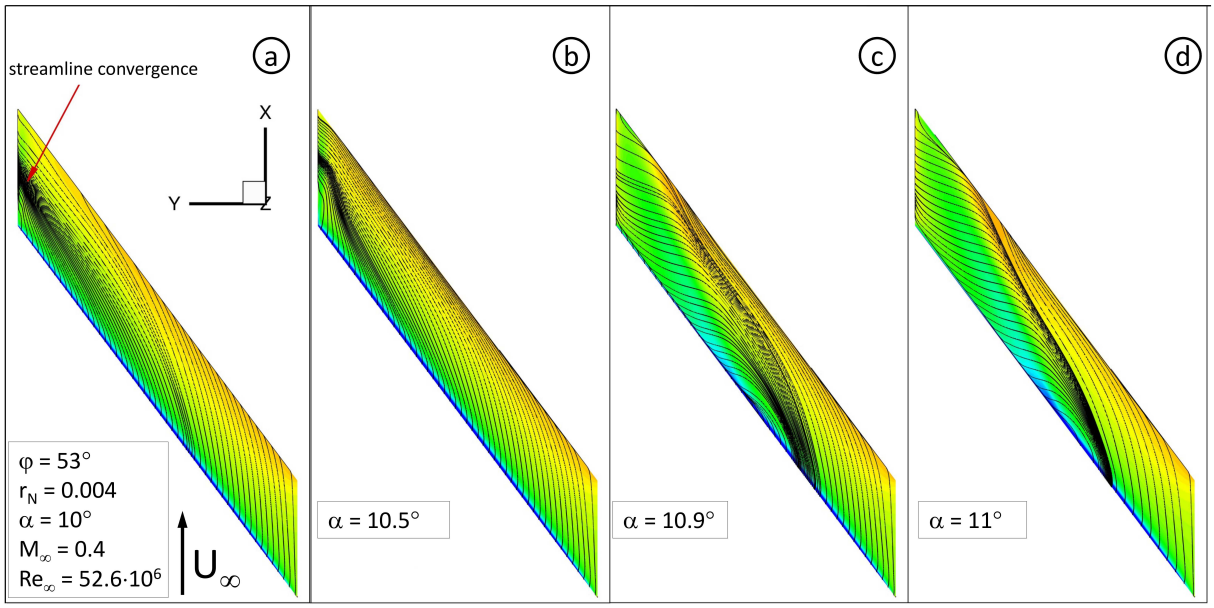

Figure 36. r_N const.: c_P distribution and surface streamlines on the upper side of the wing: $r_N = 0.004$, $\varphi = 53°$, $\alpha = 10.5°$, 10.9° und 11°, $M_\infty = 0.4$, $Re_\infty = 52.6 \cdot 10^6$.

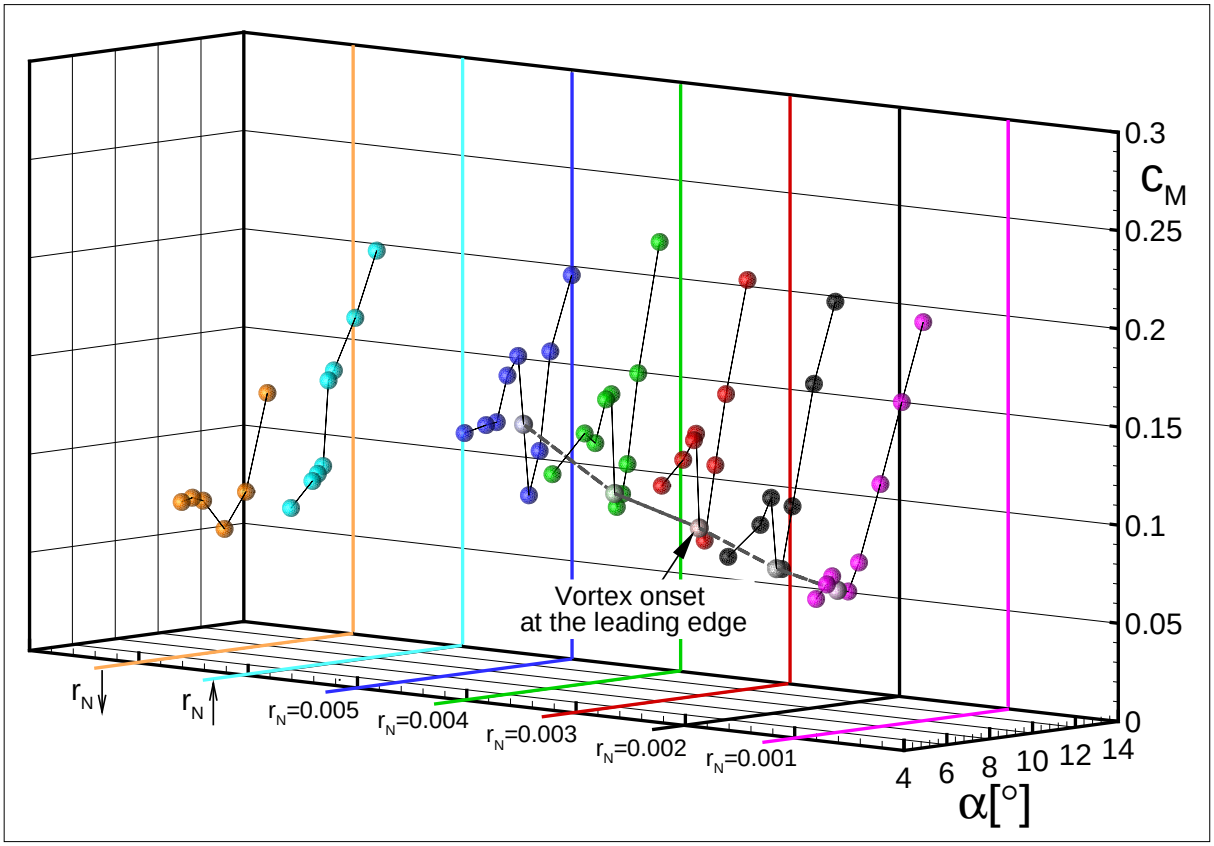

Figure 37. Pitching moment coefficient c_M versus AoA α for the configuration with $\varphi = 53°$ and variable r_N.

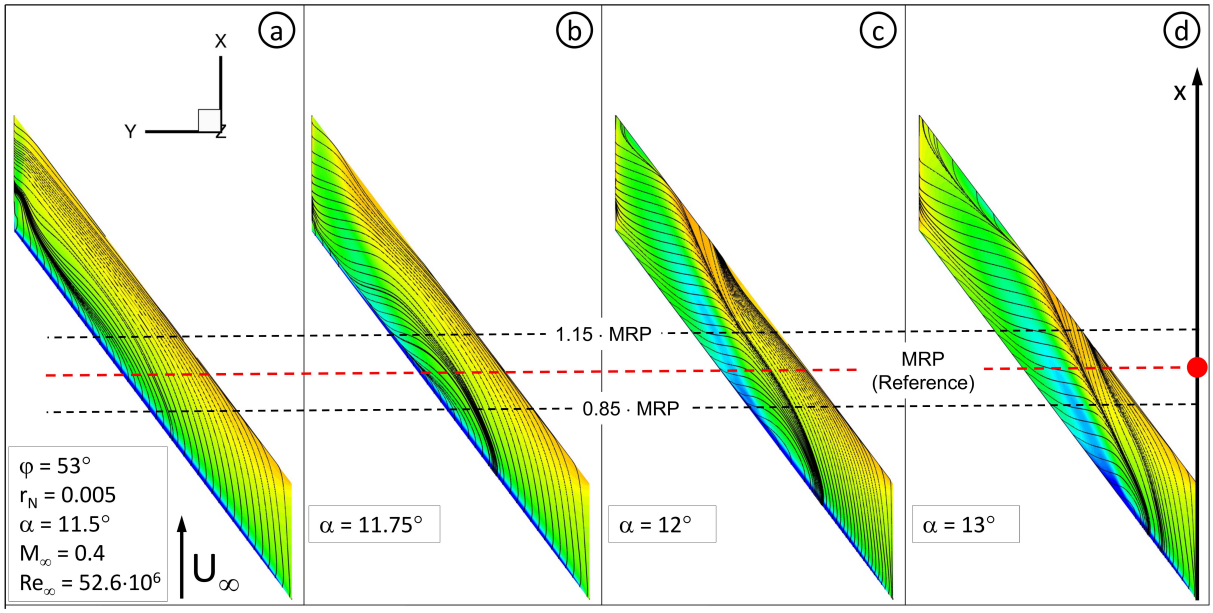

Figure 38. r_N const.: c_P distribution and surface streamlines on the upper side of the wing: $r_N = 0.005$, $\varphi = 53°$, $\alpha = 11.5°$, 11.75°, 12° und 13°, $Ma_\infty = 0.4$; $Re_\infty = 52.6 \cdot 10^6$. Pressure distribution and vortex location related to the MRP.

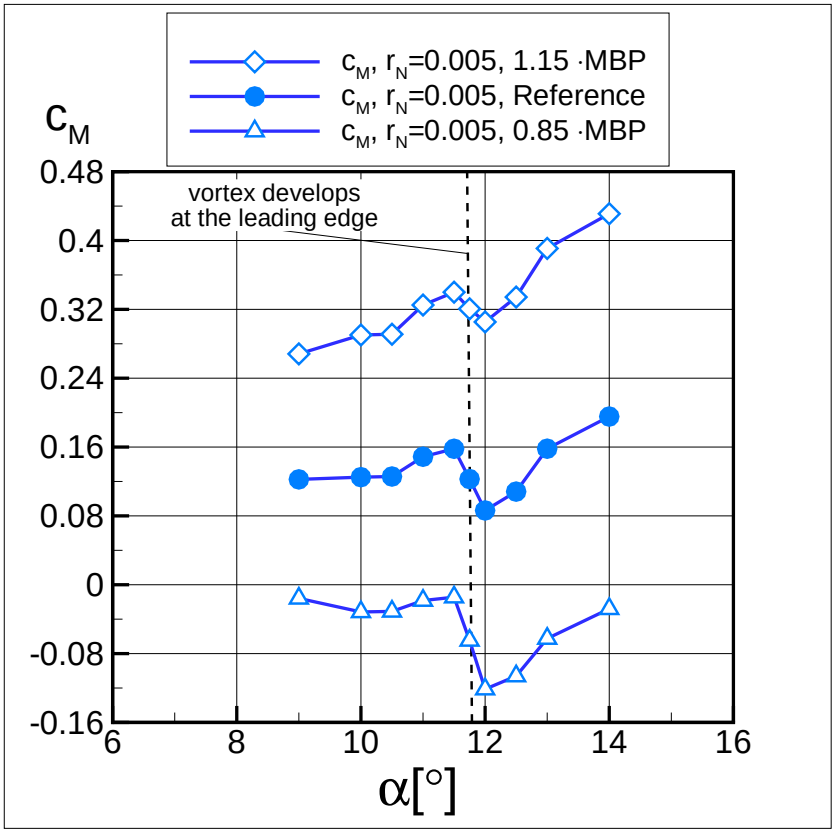

Figure 39. Pitching moment coefficient c_M versus AoA α for different locations of the MRP. r_N = 0.005, $\varphi = 53°$.

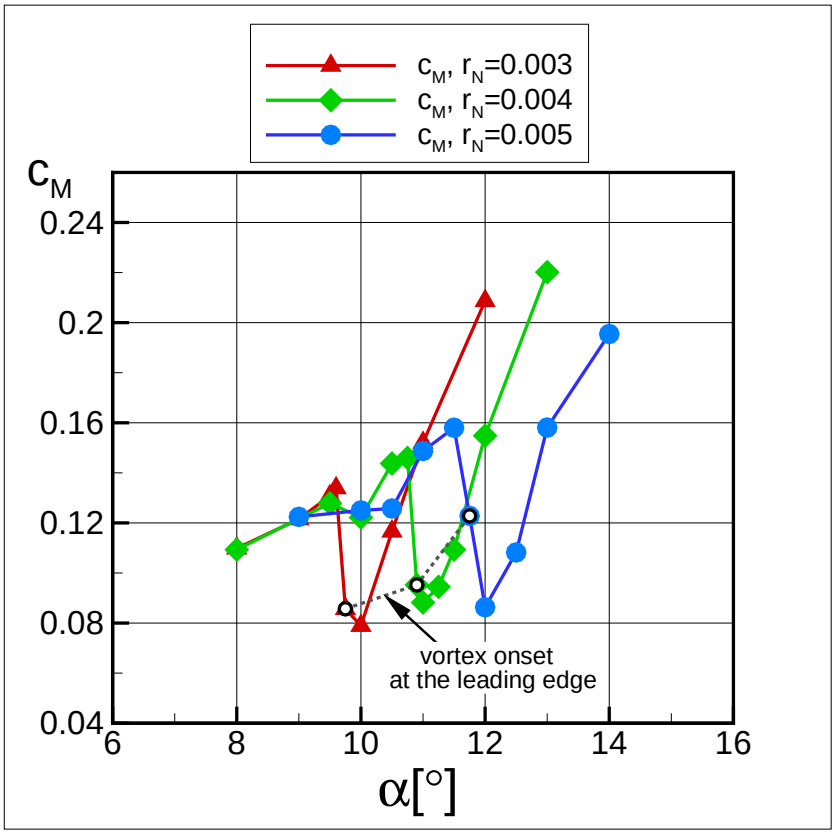

Figure 40. Pitching moment coefficient c_M versus AoA α for the configuration with $\varphi = 53°$ and r_N = 0.003, 0.004, 0.005.

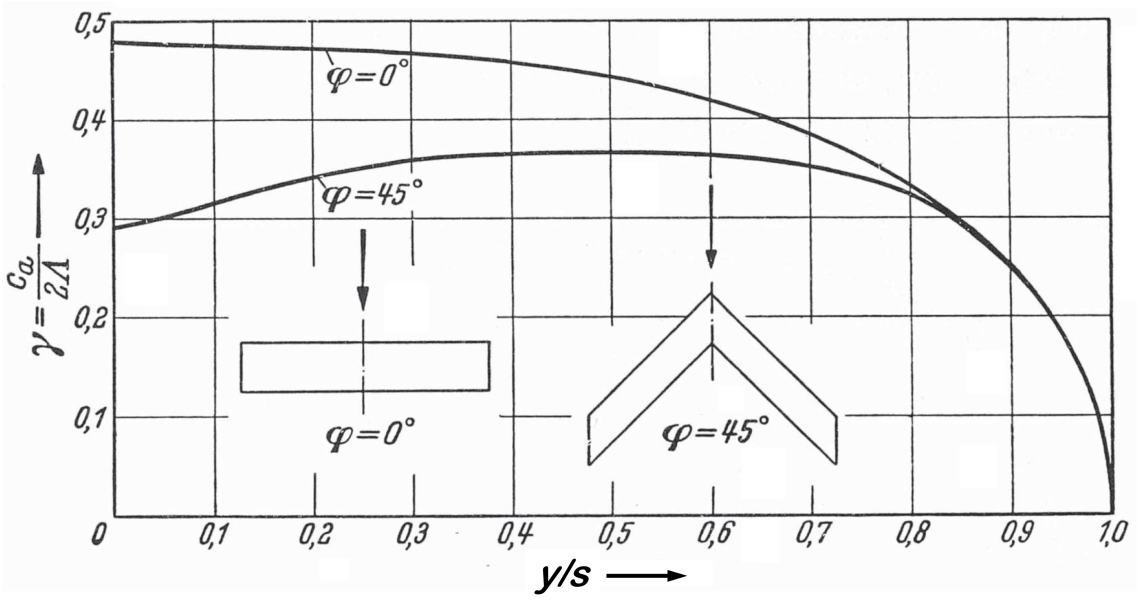

Figure 41. Distribution of the circulation along the span for two wings with an aspect ratio of $AR = 5$ and a sweep angle of $\varphi = 0°, 45°$, $\alpha =$ const. TLinear wing theory by Truckenbrodt [72]

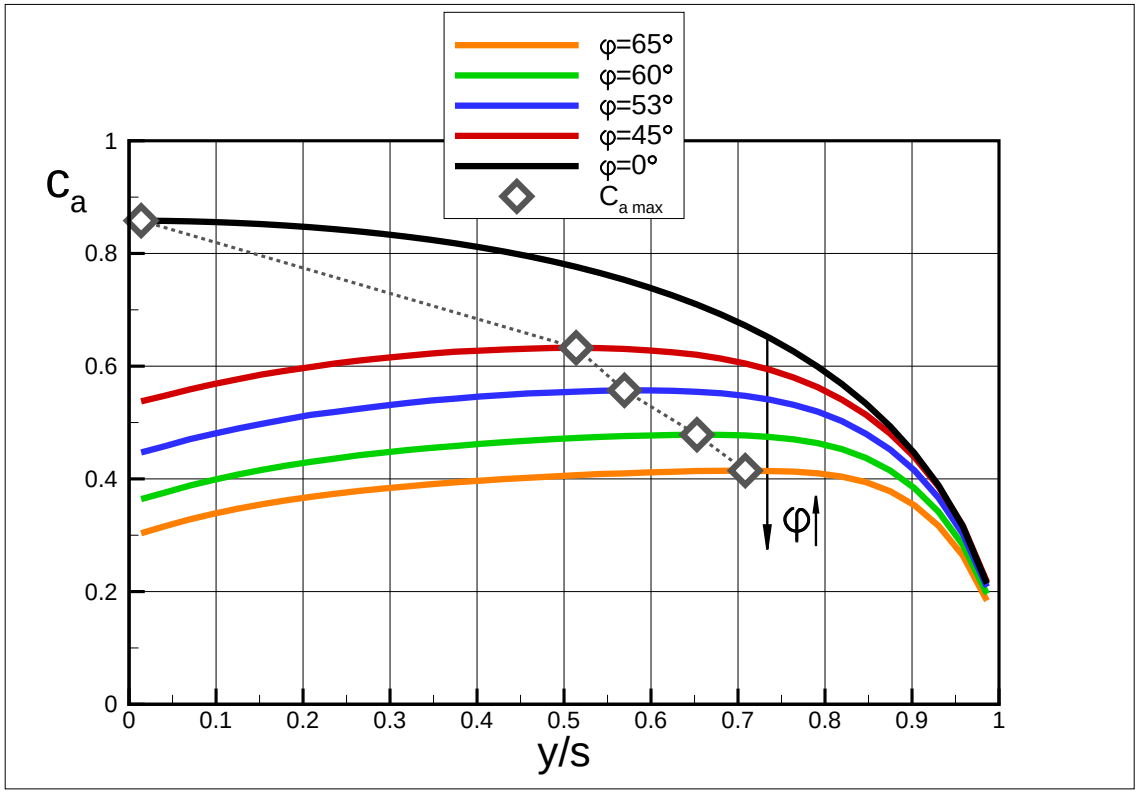

Figure 42. Distribution of the local lift coefficient along the span at profile sections perpendicular to the leading edge for two wings with an aspect ratio of $AR = 4.8$ and a sweep angle of $\varphi = 0°, 45°, 53°, 60°, 65°$, $\alpha = 10°$. Linear wing theory by Truckenbrodt [72].

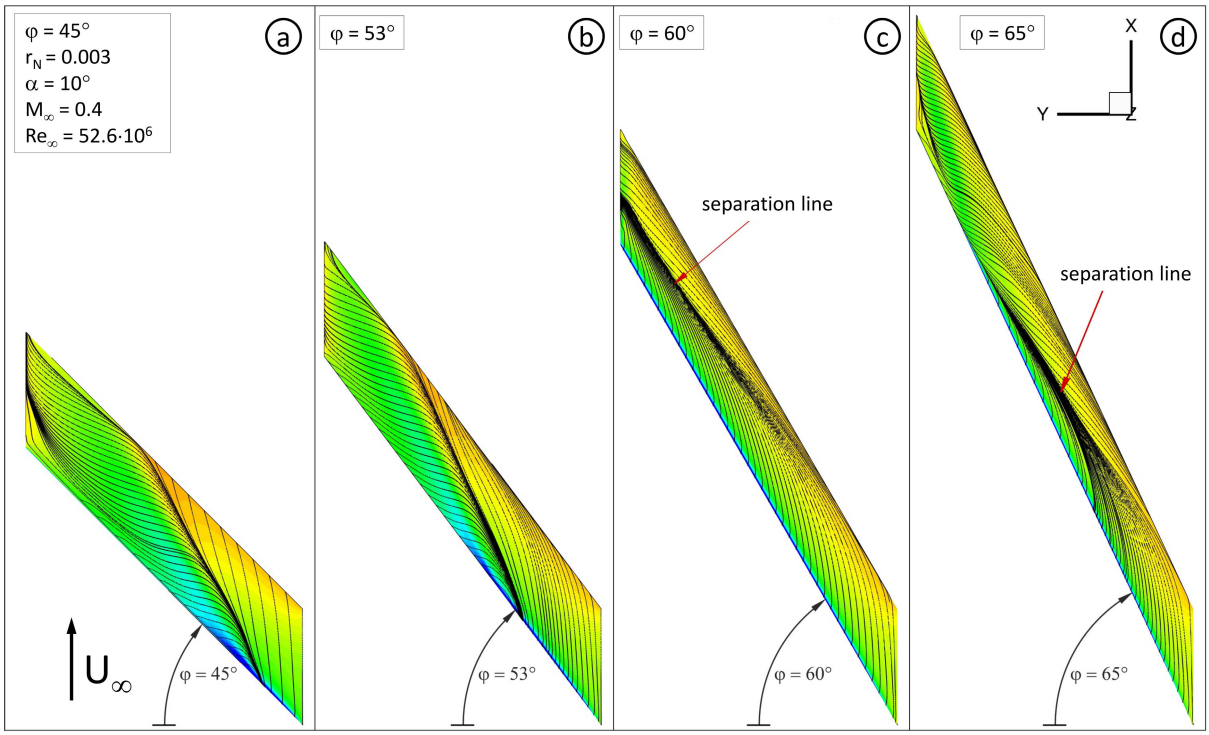

Figure 43. φ**-Effect:** c_P **distribution and surface streamlines on the upper side of the wing for different leading edge sweep angles of** φ **= 45°, 53°, 60° and 65°,** r_N **=0.003,** α **= 10°,** M_∞ **= 0.4,** Re_∞ **= 52.6·10^6.**

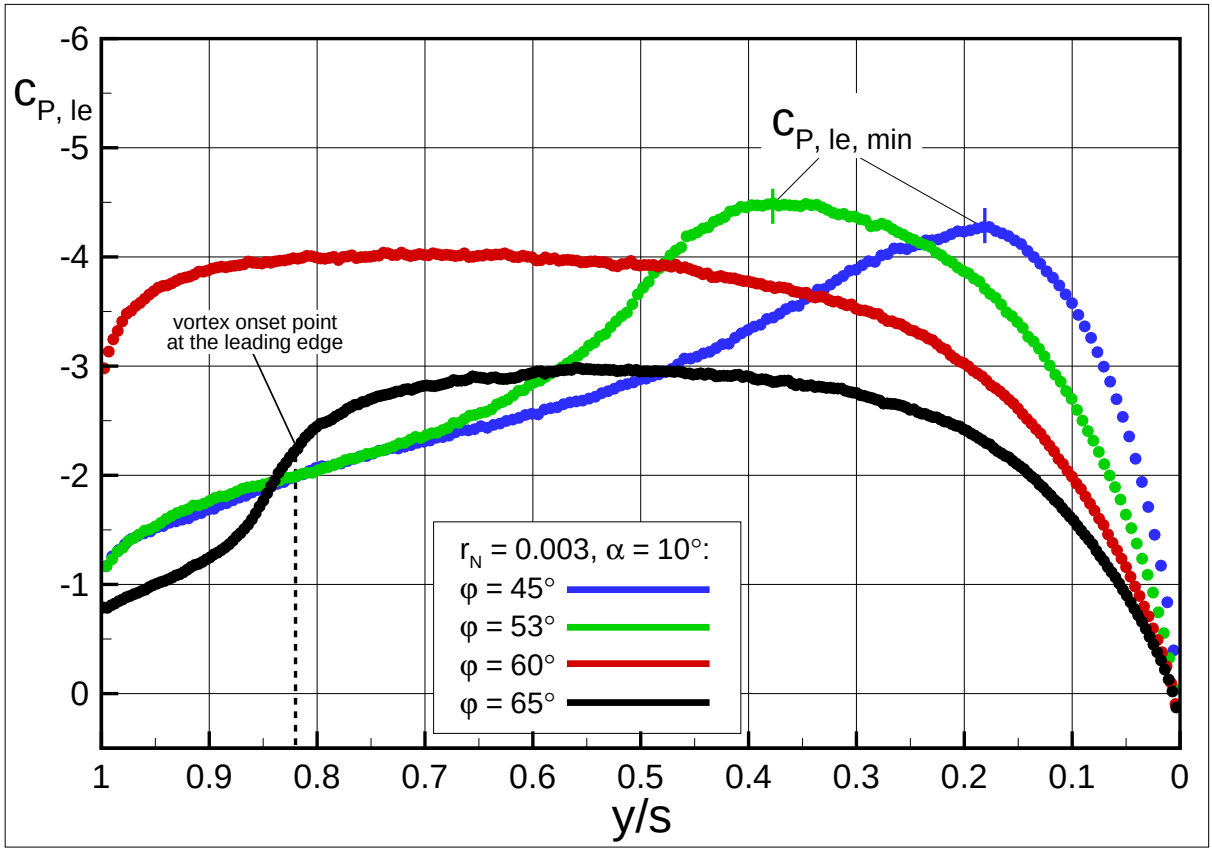

Figure 44. φ**-Effect:** c_P **distribution at the leading edge for different leading edge sweep angles of** φ **= 45°, 53°, 60° and 65°,** r_N **=0.003,** α **= 10°,** M_∞ **= 0.4,** Re_∞ **= 52.6·10^6.**

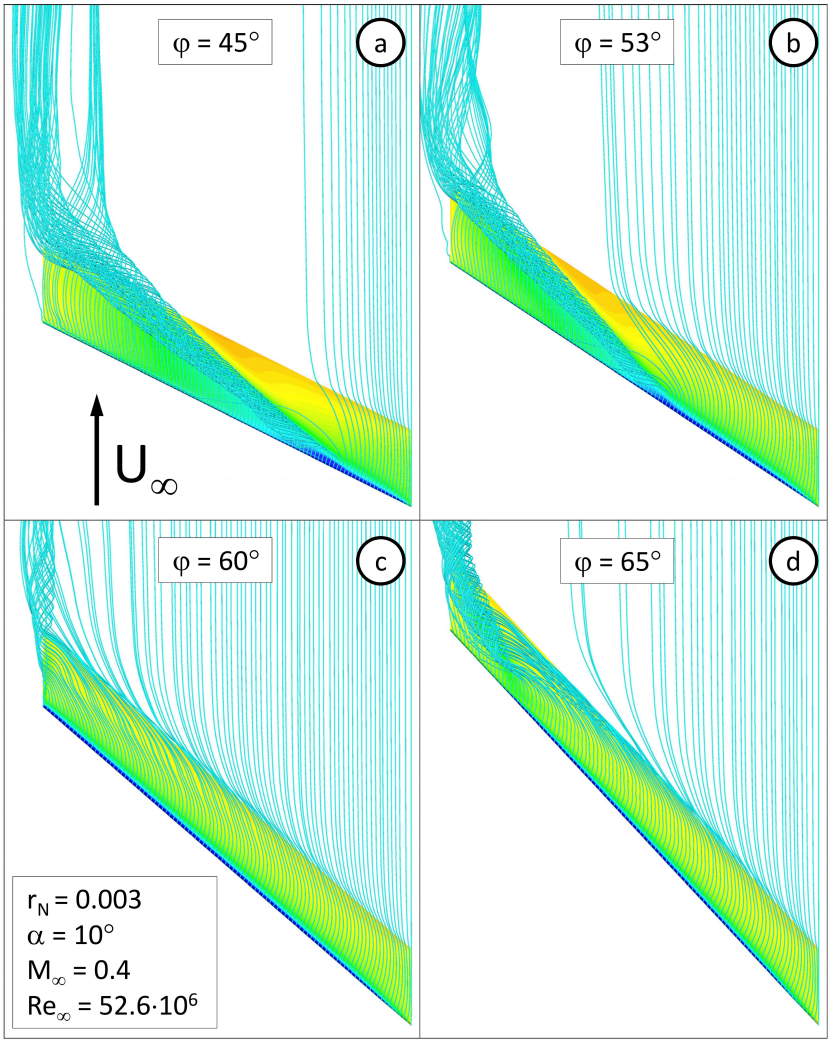

Figure 45. φ-Effect: Streamlines in the flow field upon the upper side of the wing for different leading edge sweep angles of $\varphi = 45°$, 53°, 60° and 65°, $r_N = 0.003$, $\alpha = 10°$, $M_\infty = 0{,}4$; $Re_\infty = 52.6 \cdot 10^6$.

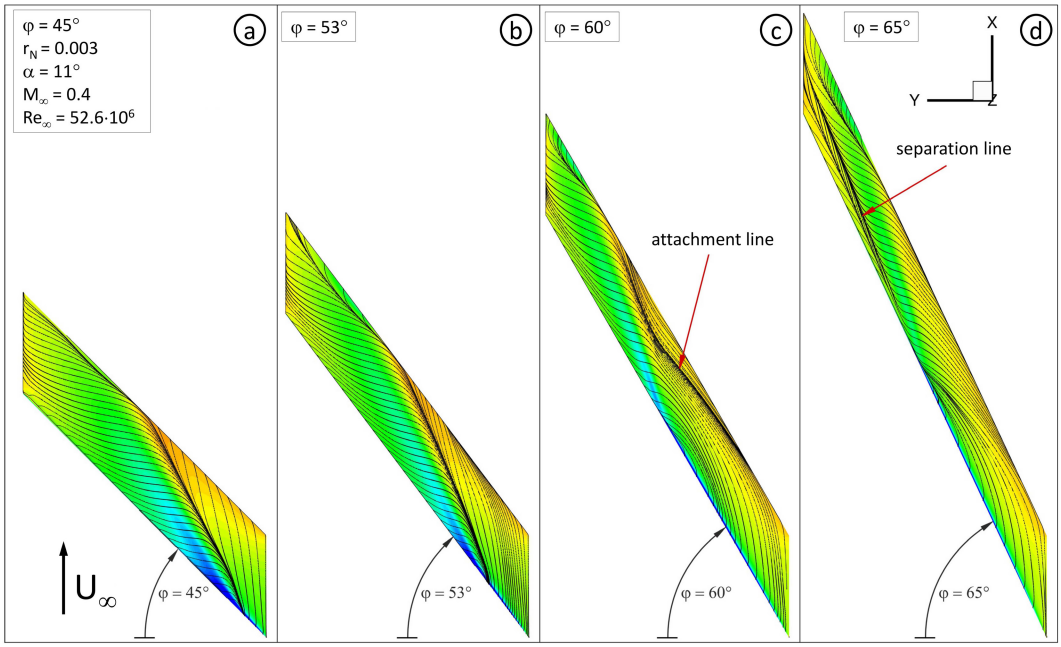

Figure 46. φ-Effect: c_P distribution and surface streamlines on the upper side of the wing for different leading edge sweep angles of $\varphi = 45°$, 53°, 60° and 65°, $r_N = 0.003$, $\alpha = 11°$, $M_\infty = 0.4$, $Re_\infty = 52.6 \cdot 10^6$.

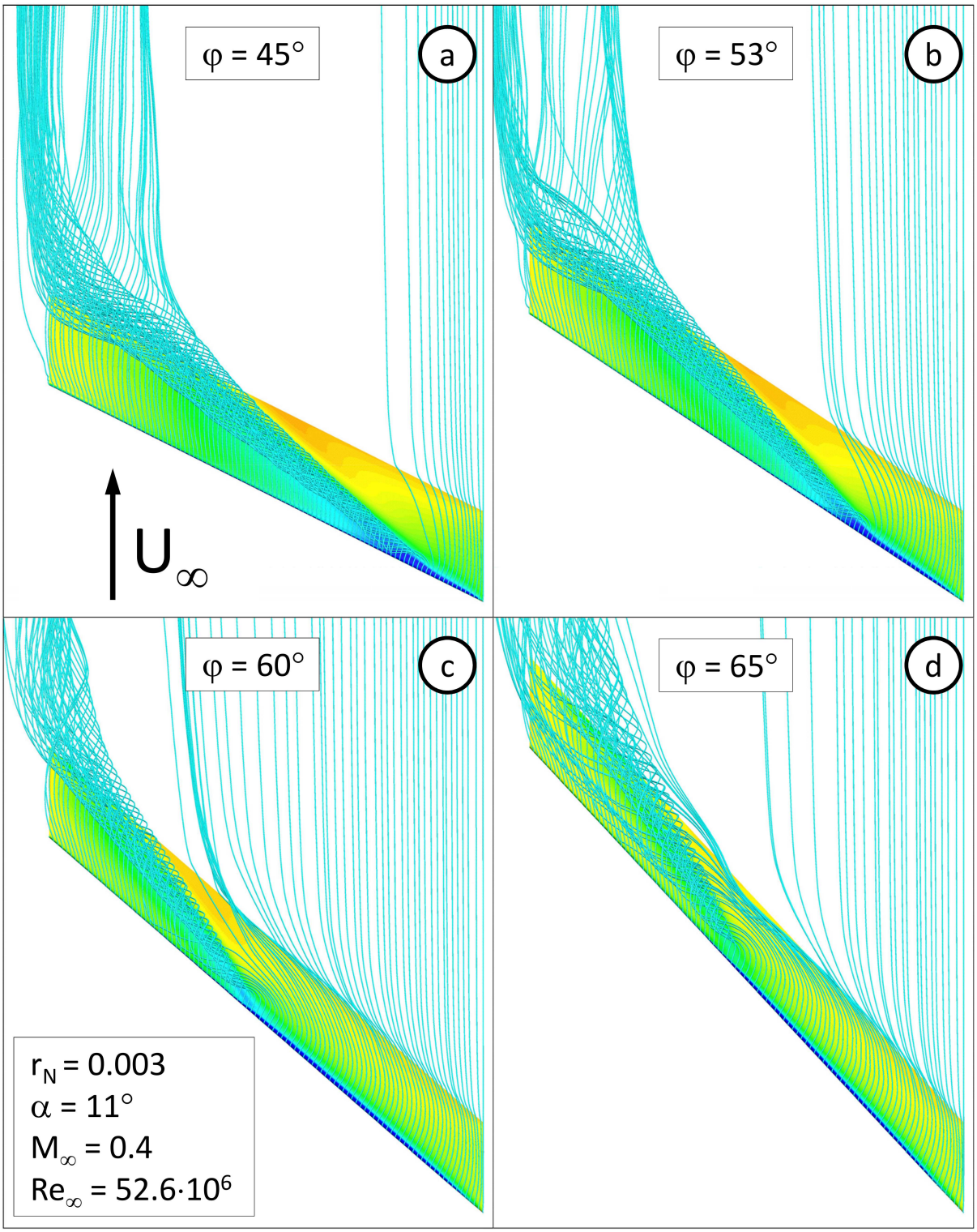

Figure 47. φ-Effect: Streamlines in the flow field upon the upper side of the wing for different leading edge sweep angles of $\varphi = 45^\circ$, 53°, 60° and 65°, $r_N = 0.003$, $\alpha = 11^\circ$, $M_\infty = 0{,}4$; $Re_\infty = 52.6 \cdot 10^6$.

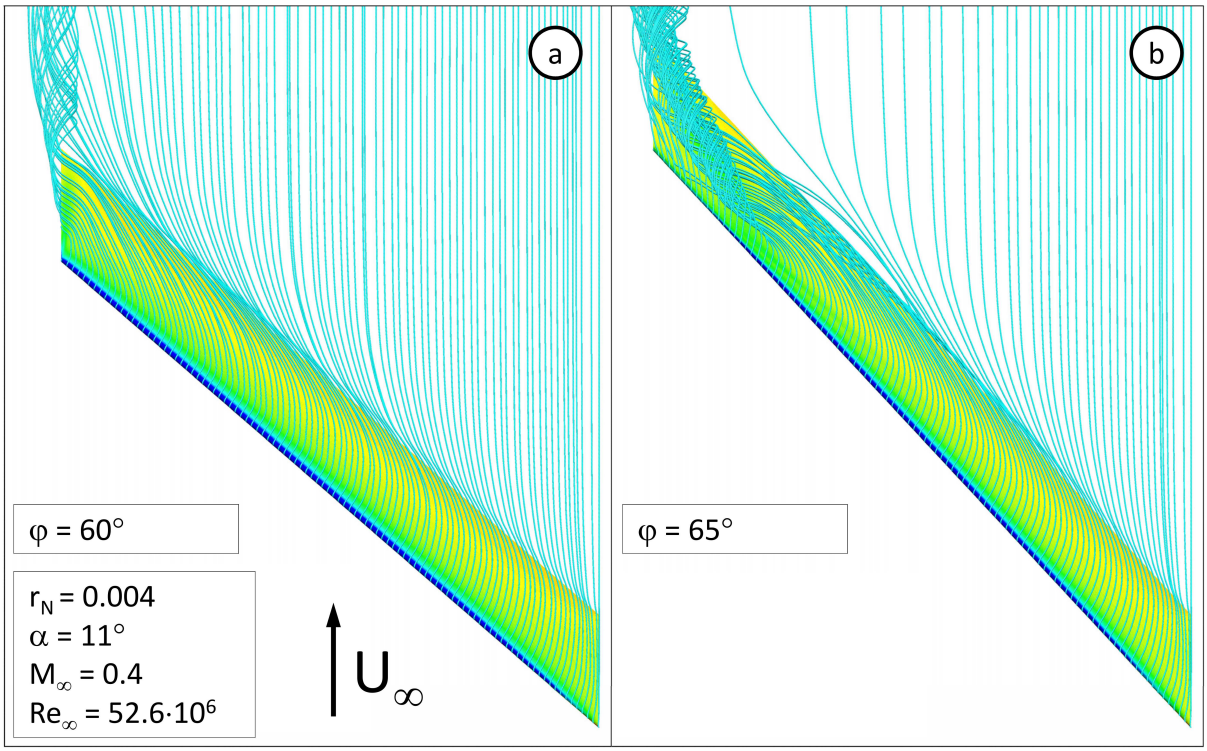

Figure 48. φ-Effect: Streamlines in the flow field upon the upper side of the wing for different leading edge sweep angles of $\varphi = 60°$ and 65°, $r_N = 0.004$, $\alpha = 11°$, $M_\infty = 0,4$; $Re_\infty = 52.6 \cdot 10^6$.

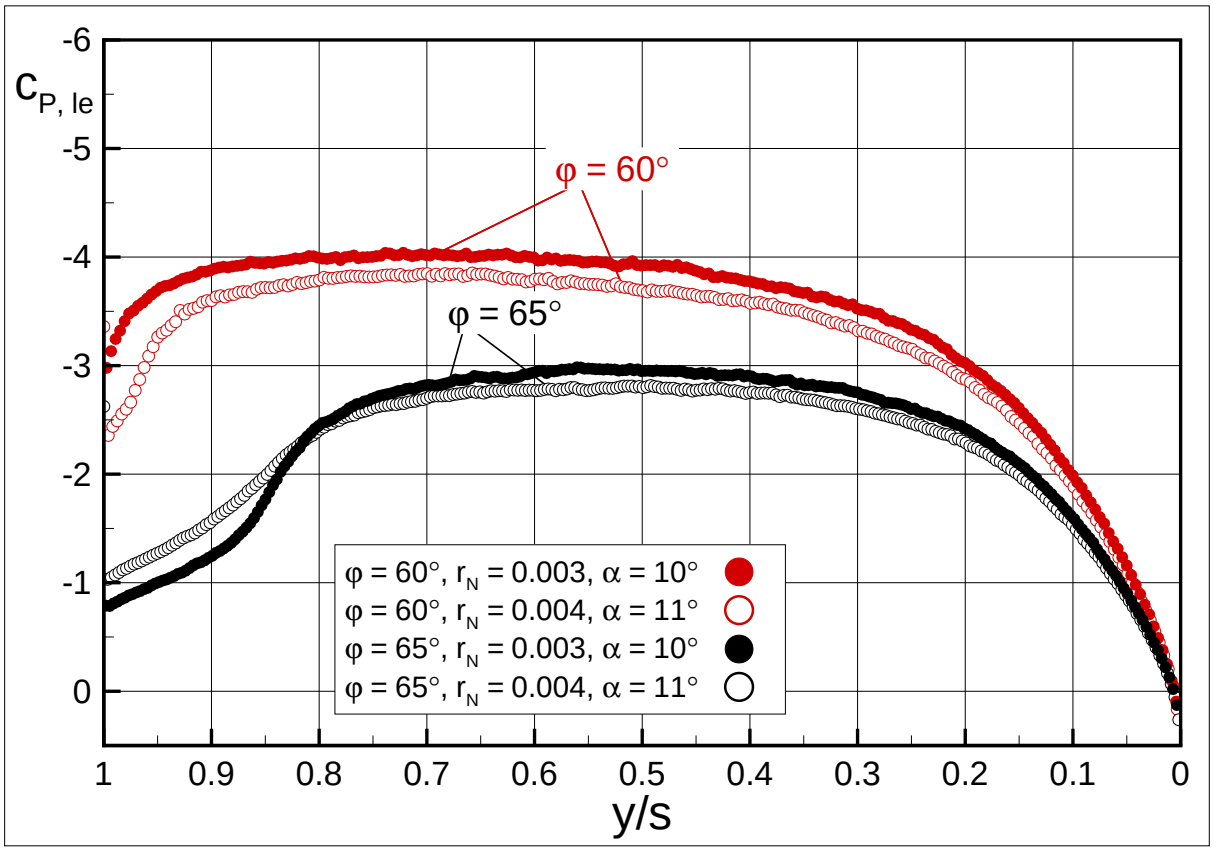

Figure 49. φ-Effect: c_P distribution at the leading edge. Comparison of different sweep angle $\varphi = 60°$ and 65° for different leadinmg edge contour radii of $r_N = 0.003$ and 0.004 at $\alpha = 10°$ and 11° , $M_\infty = 0.4$, $Re_\infty = 52.6 \cdot 10^6$.

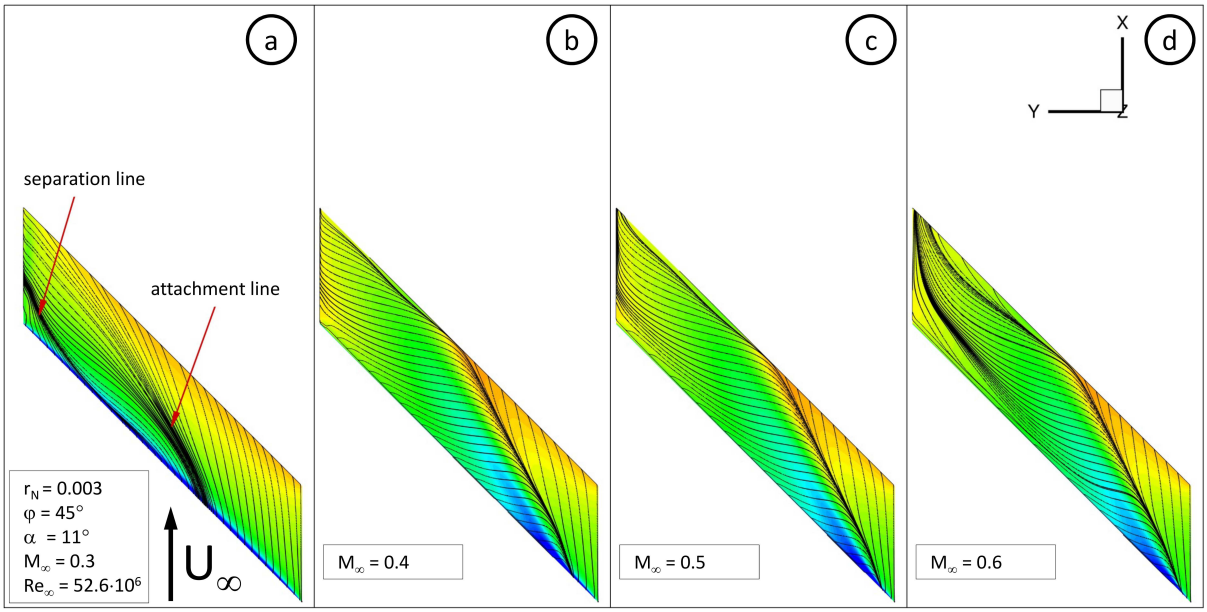

Figure 50. Mach-Effect: c_P distribution and surface streamlines on the upper side of the wing for different onflow Mach numbers of M_∞ = 0.3, 0.4, 0.5 and 0.6, φ = 45°, r_N =0.003, α = 11°, Re_∞ = 52.6·10^6.

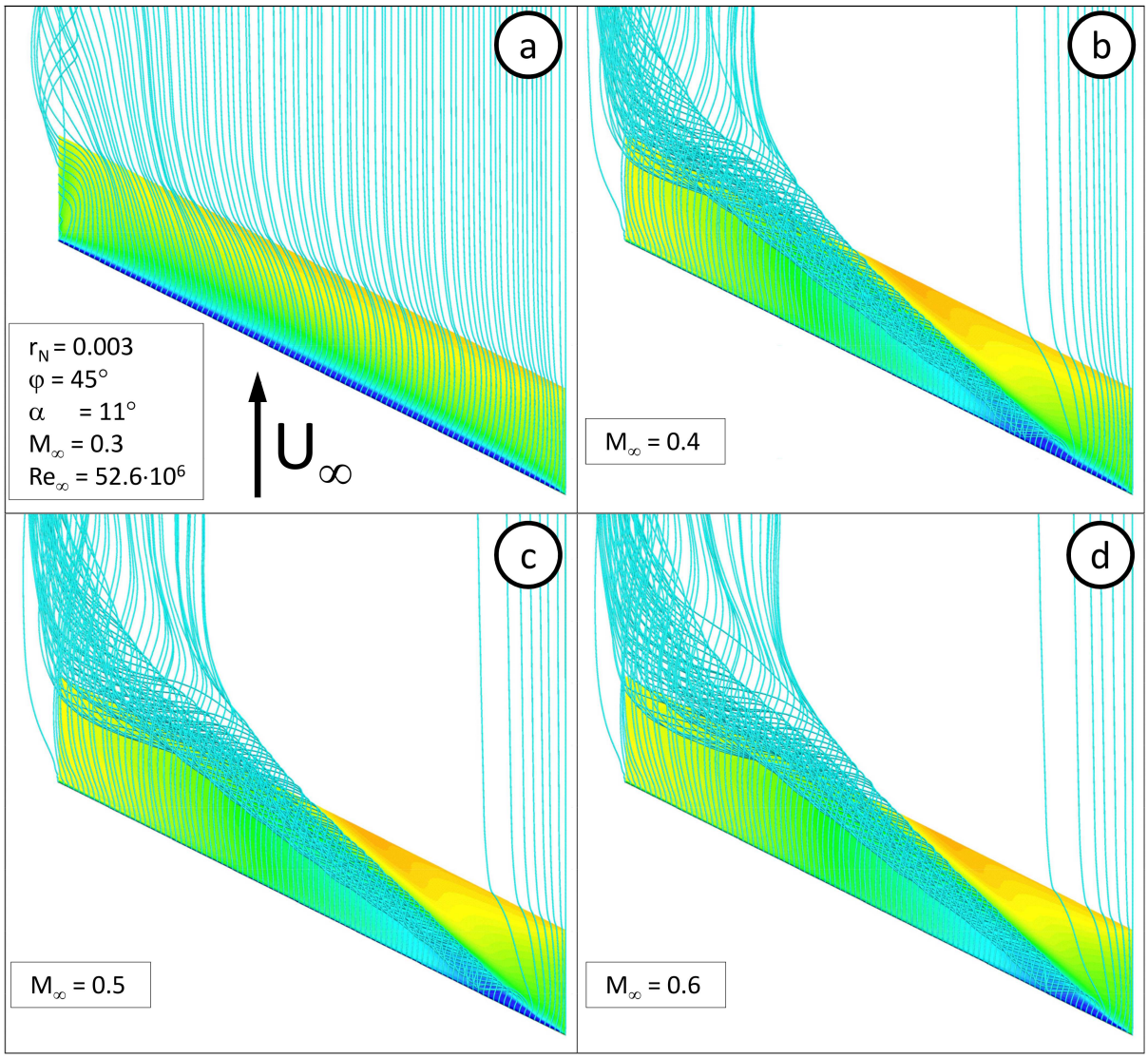

Figure 51. Mach-Effect: Streamlines in the flow field upon the upper side of the wing for different onflow Mach numbers of M_∞ = 0.3, 0.4, 0.5 and 0.6, φ = 45°, r_N =0.003, α = 11°, Re_∞ = 52.6·10^6.

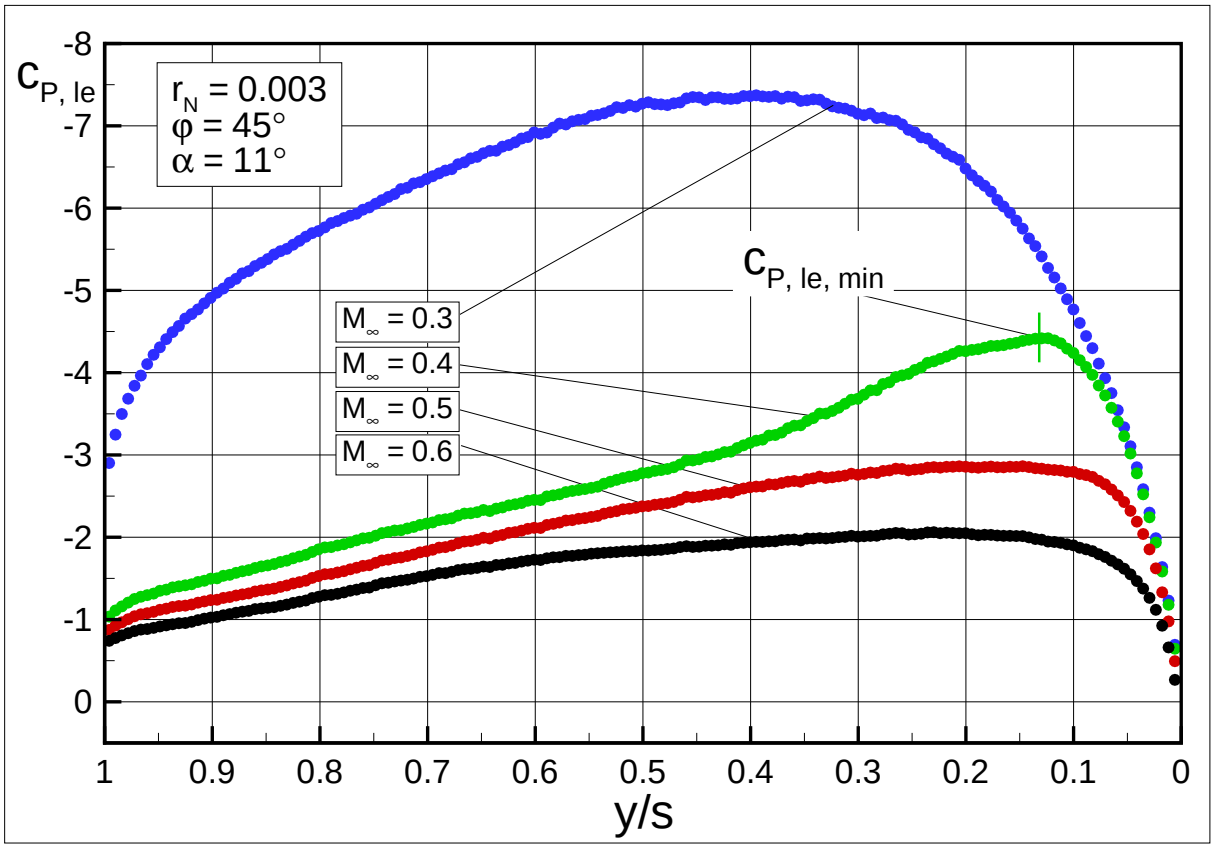

Figure 52. Mach-Effect: c_P distribution at the leading edge. Comparison of different Mach numbers of M_∞ = 0.3, 0.4, 0.5 and 0.6, φ = 45°, r_N =0.003, α = 11°, Re_∞ = 52.6·10^6.

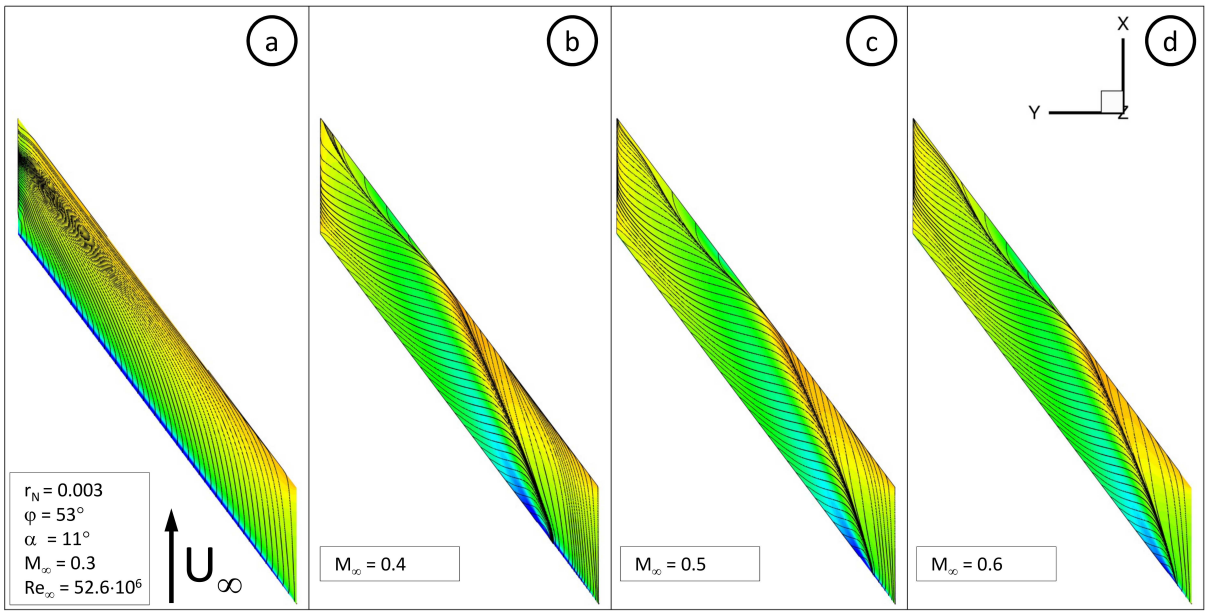

Figure 53. Mach-Effect: c_P distribution and surface streamlines on the upper side of the wing for different onflow Mach numbers of M_∞ = 0.3, 0.4, 0.5 and 0.6, φ = 53°, r_N =0.003, α = 11°, Re_∞ = 52.6·10^6.

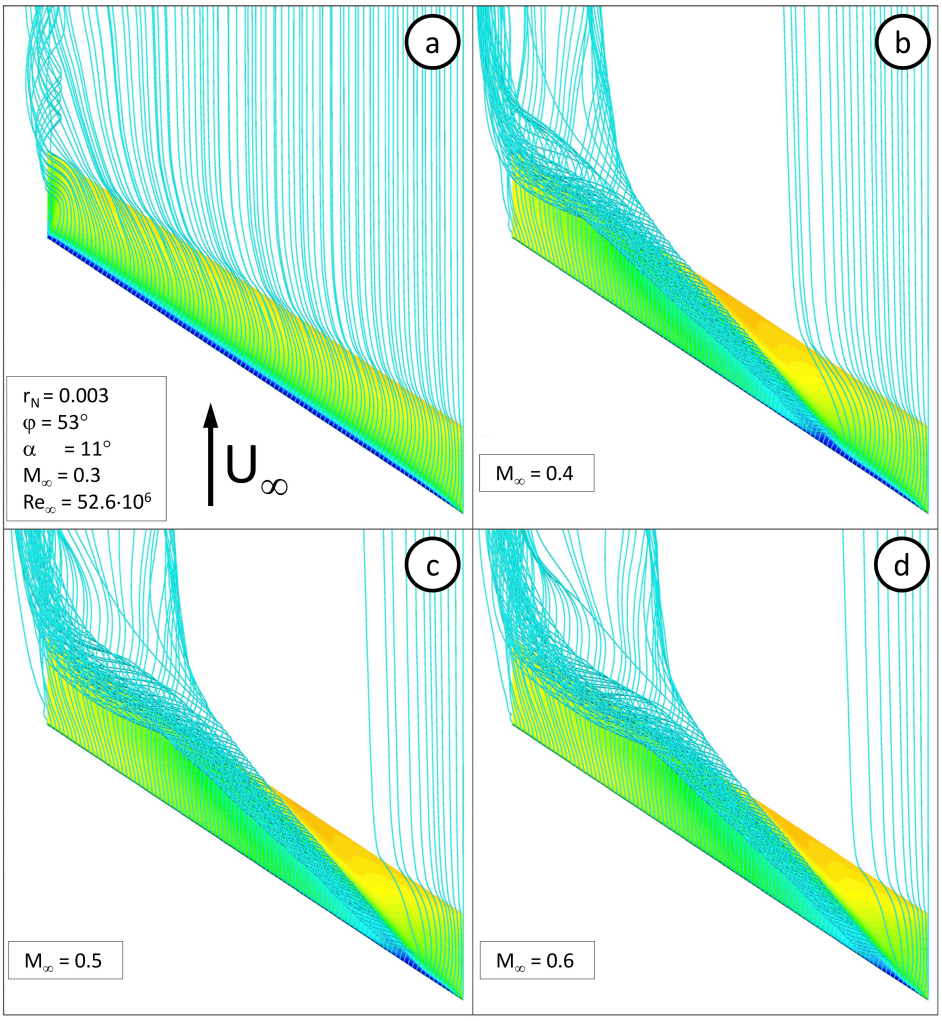

Figure 54. Mach-Effect: Streamlines in the flow field upon the upper side of the wing for different onflow Mach numbers of M_∞ = 0.3, 0.4, 0.5 and 0.6, φ = 53°, r_N =0.003, α = 11°, Re_∞ = 52.6·10^6.

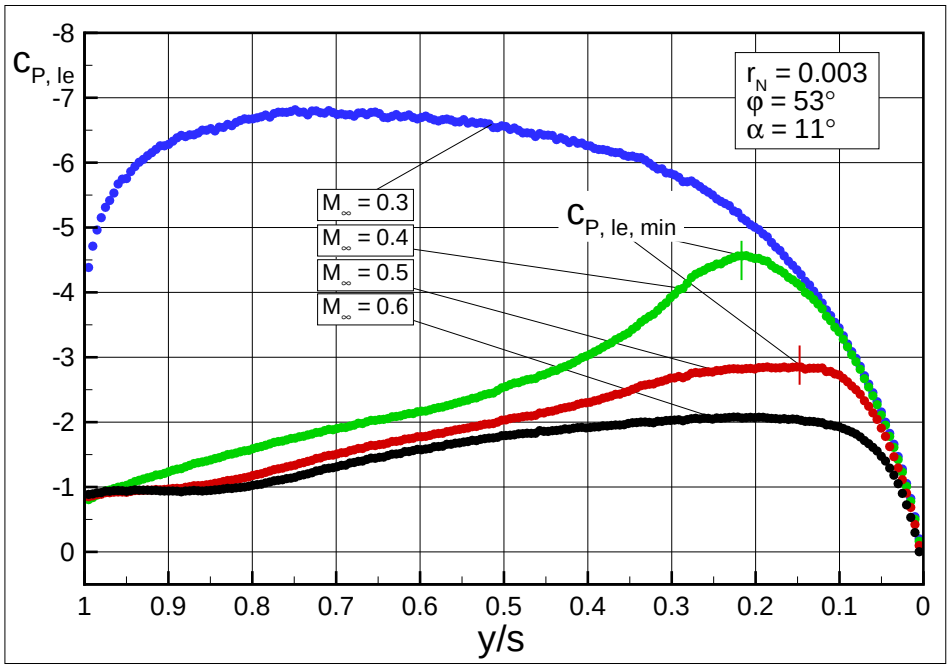

Figure 55. Mach-Effect: c_P distribution at the leading edge. Comparison of different Mach numbers of M_∞ = 0.3, 0.4, 0.5 and 0.6, φ = 53°, r_N =0.003, α = 11°, Re_∞ = 52.6·10^6.

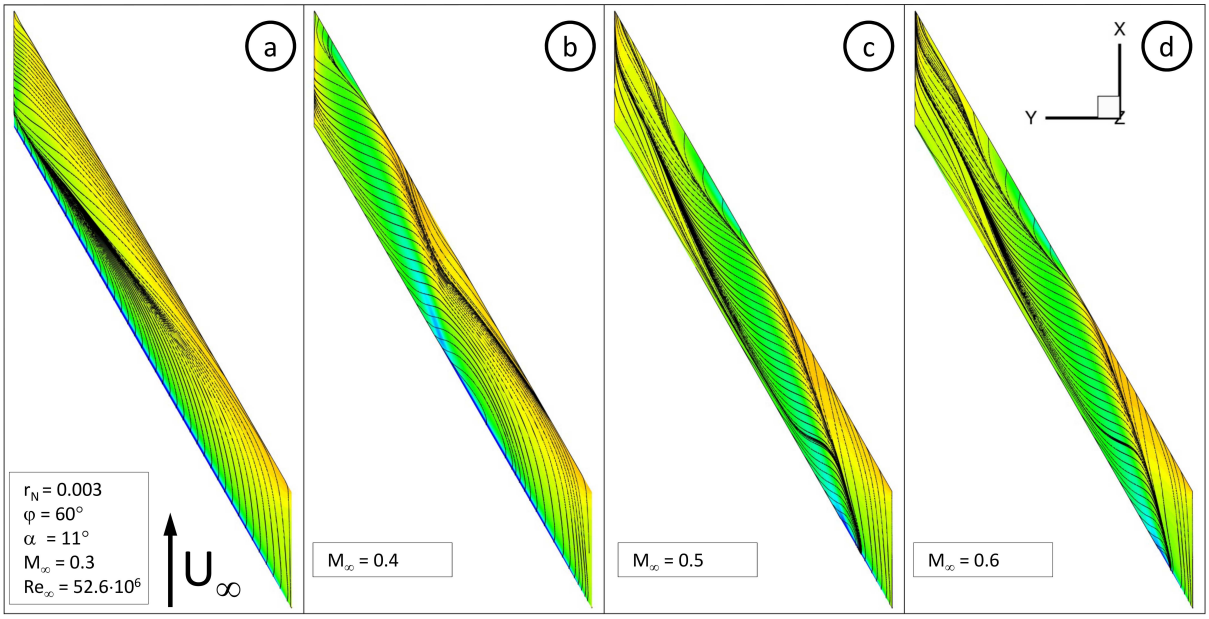

Figure 56. Mach-Effect: c_P distribution and surface streamlines on the upper side of the wing for different onflow Mach numbers of $M_\infty = 0.3, 0.4, 0.5$ and 0.6, $\varphi = 60°$, $r_N = 0.003$, $\alpha = 11°$, $Re_\infty = 52.6 \cdot 10^6$.

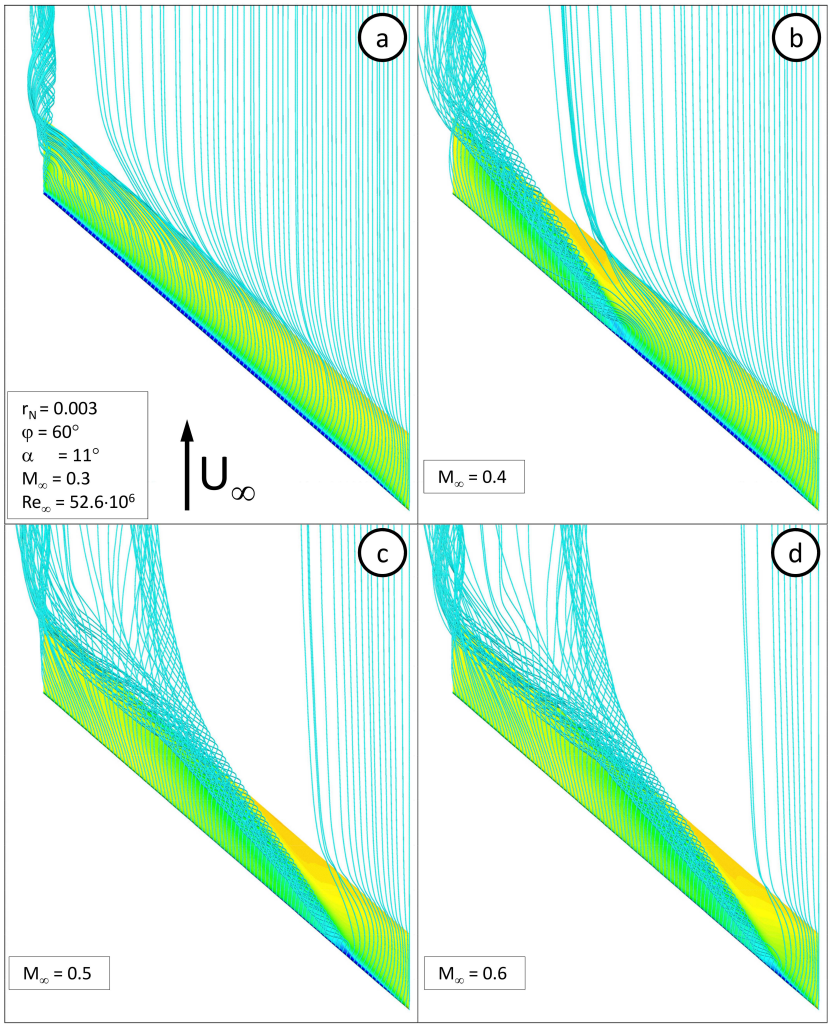

Figure 57. Mach-Effect: Streamlines in the flow field upon the upper side of the wing for different onflow Mach numbers of $M_\infty = 0.3, 0.4, 0.5$ and 0.6, $\varphi = 60°$, $r_N = 0.003$, $\alpha = 11°$, $Re_\infty = 52.6 \cdot 10^6$.

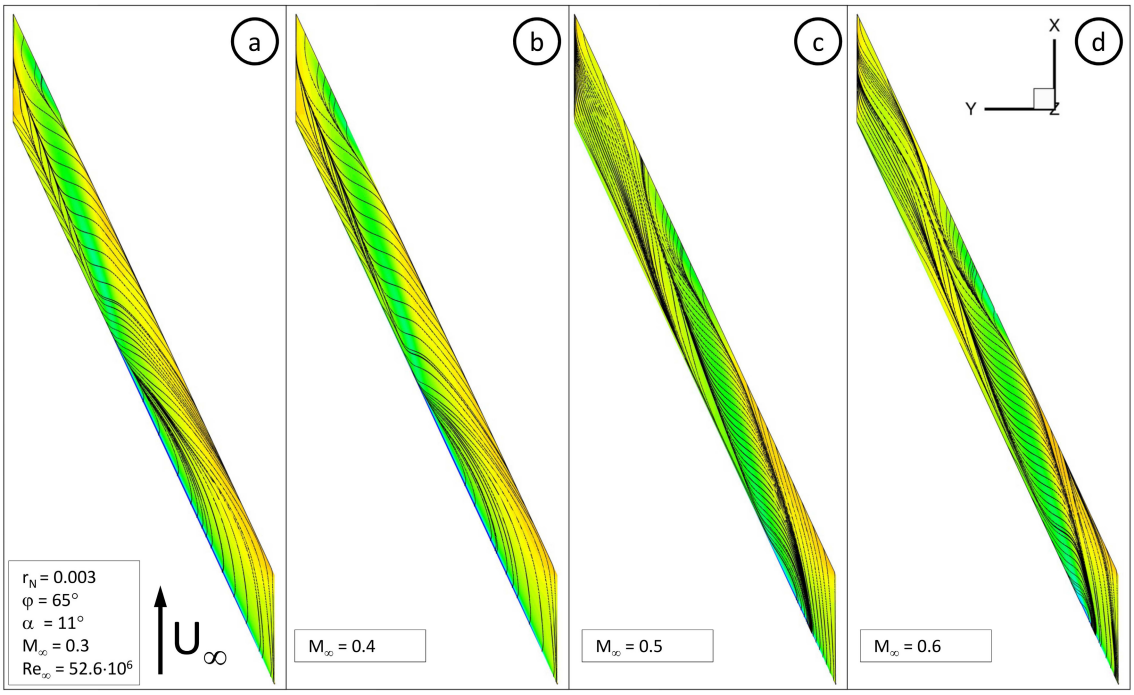

Figure 58. Mach-Effect: c_P distribution and surface streamlines on the upper side of the wing for different onflow Mach numbers of M_∞ = 0.3, 0.4, 0.5 and 0.6, $\varphi = 65°$, r_N =0.003, $\alpha = 11°$, $Re_\infty = 52.6 \cdot 10^6$.

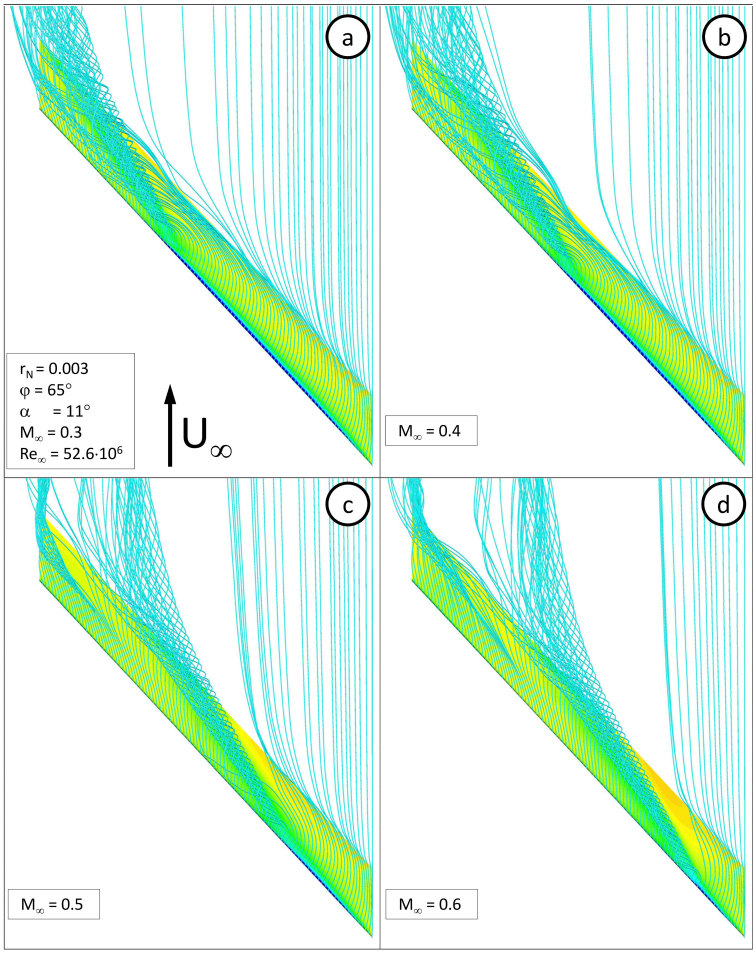

Figure 59. Mach-Effect: Streamlines in the flow field upon the upper side of the wing for different onflow Mach numbers of M_∞ = 0.3, 0.4, 0.5 and 0.6, $\varphi = 65°$, r_N =0.003, $\alpha = 11°$, $Re_\infty = 52.6 \cdot 10^6$.

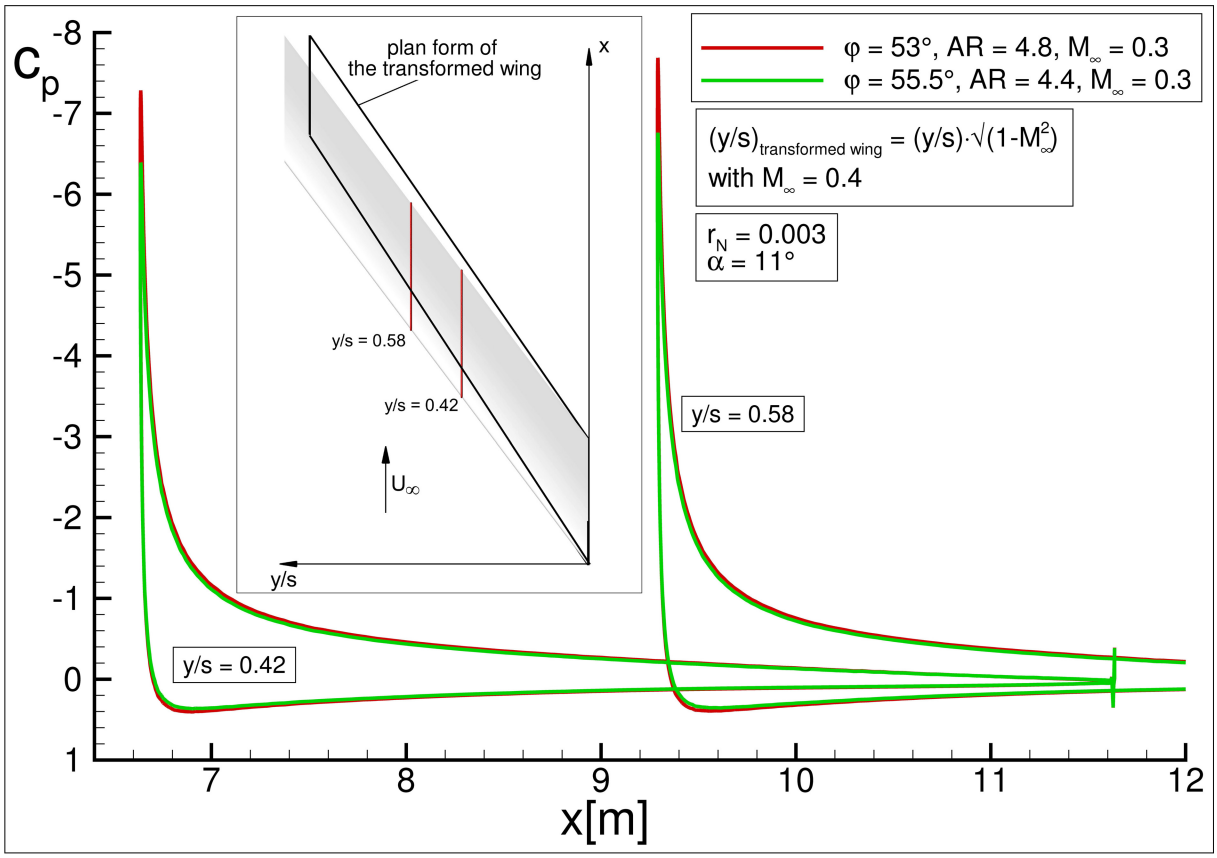

Figure 60. Mach-Effect: Pressure distribution at two locations y/s=const. TAU calculation: Original wing with $\varphi = 53°$ at $M_\infty = 0.3$ and transformed wing with $\varphi = 55.5°$ at $M_\infty = 0.3$ ($r_N = 0.003$ at $\alpha = 11°$; $Re_\infty = 52.6 \cdot 10^6$).

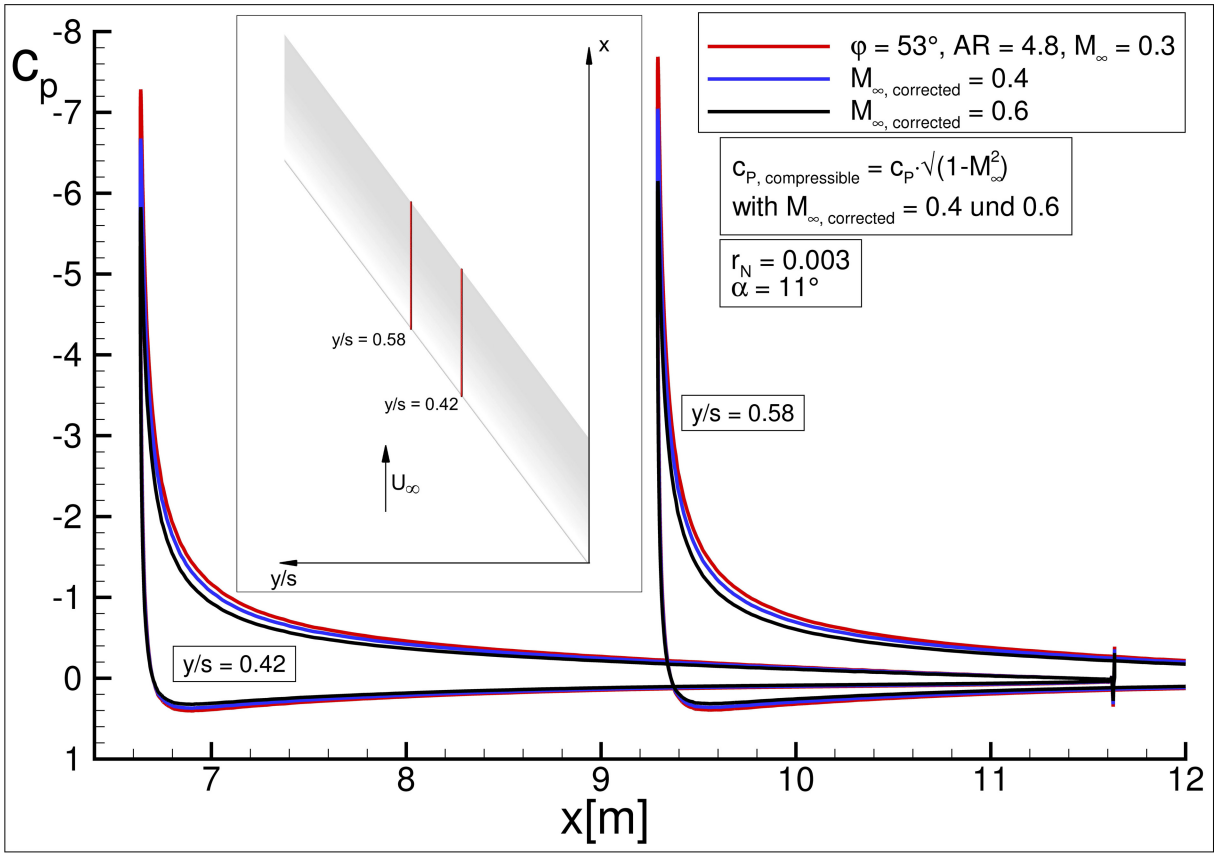

Figure 61. Mach-Effect: Pressure distribution at two locations y/s=const. TAU calculation: Original wing with $\varphi = 53°$ at $M_\infty = 0.3$ ($r_N = 0.003$ at $\alpha = 11°$; $Re_\infty = 52.6 \cdot 10^6$). PGE-rule: corrected pressure distribution for $M_\infty = 0.4$ and 0.6.

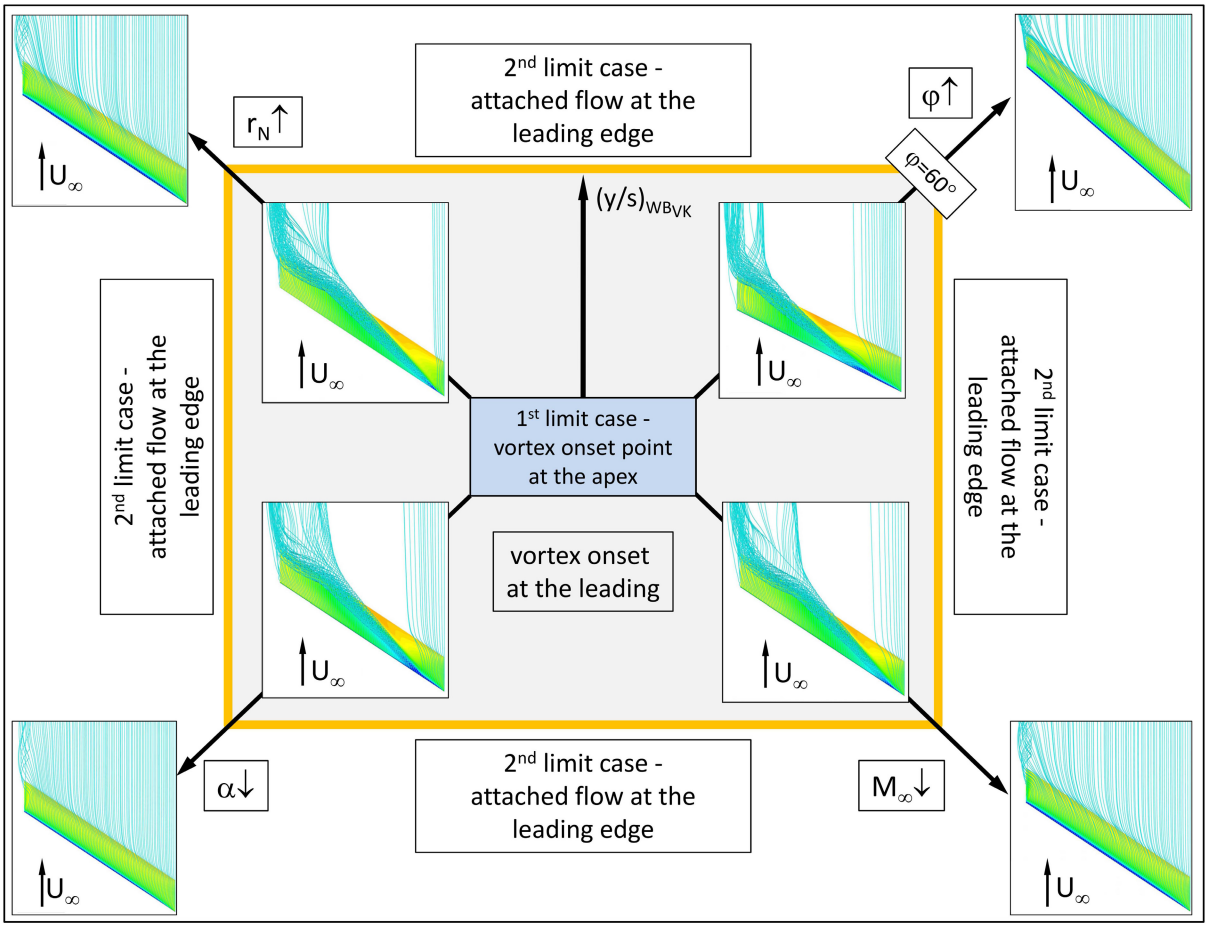

Figure 62. Overview of the assessed design rules: Effect of Angle of attack, sweep angle, leadings edge contour radius and Mach number.